Universitat Autònoma de Barcelona

SYNTHESIS OF NOVEL POLYMERIC MATERIALS FOR HIGH-PERFORMANCE AND 3D PRINTING APPLICATIONS

Guillem Romero-Sabat

SYNTHESIS OF NOVEL POLYMERIC MATERIALS FOR HIGH-PERFORMANCE AND 3D PRINTING APPLICATIONS

Guillem Romero-Sabat

DOCTORAL THESIS IN MATERIALS SCIENCE

2022

LEITAT
managing technologies

UAB
Universitat Autònoma
de Barcelona

DOCTORAL THESIS IN MATERIALS SCIENCE

SYNTHESIS OF NOVEL POLYMERIC MATERIALS FOR HIGH-PERFORMANCE AND 3D PRINTING APPLICATIONS

Guillem Romero-Sabat

DRA. SANDRA MEDEL FERNÁNDEZ
(DIRECTOR)

Applied Chemistry and Materials Division
Leitat Technological Center

LEITAT
managing technologies

UAB
Universitat Autònoma
de Barcelona

DOCTORAL THESIS IN MATERIALS SCIENCE

SYNTHESIS OF NOVEL POLYMERIC MATERIALS FOR HIGH-PERFORMANCE AND 3D PRINTING APPLICATIONS

Author:
Guillem Romero-Sabat
Director:
Dra. Sandra Medel Fernández
Tutor:
Dr. Jordi Hernando Campos

Thesis committee
President:
Dr. José Alberto Méndez González
Secretary:
Dr. Claudio Roscini
Spokesperson:
Dra. Paula Bosch Sarobe

LEITAT
managing technologies

UAB
Universitat Autònoma de Barcelona

Agradecimientos

Quiero aprovechar en cierta medida esta ventana para devolver, en forma de algunas líneas, una pequeña fracción de todo el cariño y apoyo que tanto amigos y familia me habéis dado haciendo que mi vida sea mejor. Sin vosotros, esto no sería posible, así que, de todo corazón, gracias.

En primer lugar, me gustaría dar las gracias a mi directora de tesis, la Dra. Sandra Medel, por aceptar dirigir esta tesis, por encontrar tiempo para las infinitas revisiones con sus correspondientes correcciones constructivas, por aguantar muchas más quejas de las que debería y por enseñarme muchas de las cosas que quedan patentes en este documento. No hay suficiente vermut ni cerveza para compensarlo.

A los grupos de síntesis y de procesado de polímeros, los momentos que pasamos juntos hacen que ir a trabajar cada día sea mucho más llevadero. Especialmente, agradecer a Hector Linuesa, por ser un gran jefe, mucho mejor persona y depositar su confianza en mí y al Dr. Luis Granda, por aportar su punto de vista y mejorar mi criterio científico.

A Ainhoa y Joseba, por introducirme en el mundo de la síntesis de polímeros, transmitirme su entusiasmo por él y ser los mejores referentes gastronómicos.

I would like to give my most heartfelt thanks to all the amazing Inventia people at Sydney. To Dr. Martin Engel and Dr. Cameron Ferris for trusting me half-way across the globe and letting me be part of the family. To all the *X-cessive ninja's* people, you made the pandemic time feel like a wonderful adventure.

A Mateu y Irene por ser de los mejores amigos que uno podría querer a su lado. Al equipo de los viernes, por vuestros ánimos y grandes momentos de cada semana con los que habéis hecho que el camino haya sido mucho más ameno.

A mis padres, porque aun estando físicamente separados durante gran parte de la realización de este trabajo, me han apoyado siempre de manera incondicional y me han dado las herramientas y el cariño para poder llegar dónde estoy ahora. Gracias por estar siempre que lo he necesitado.

A mi hermana África, por tener una capacidad de superación que me inspira a mejorar. A mis primos, Alex y Fani, por hacerme tener una sonrisa siempre que estamos juntos y a Víctor, por ser la personificación de "*cuqui*" y darlo siempre todo por ayudar a los demás.

A mi familia política y a mis tíos, por estar ahí para arroparme, ayudarme y darme ánimos.

A mis abuelos por ser referentes en cómo quiero ser de mayor.

Y por último, a Anna, porque para ti no hay palabras suficientes para agradecer todo lo que me das cada día de mi vida. Des del momento en el que nos conocimos me has hecho querer ser mejor persona y me has ayudado con todo lo que tienes para conseguir mis sueños y objetivos. Me has enseñado que cada día es una oportunidad para hacer aquello que nos hace felices y me das ese empujón para que siempre intente dar lo máximo de mí, se cuál sea la circunstancia. Sin ti, muy posiblemente esta tesis seguiría siendo una idea en mi cabeza.

Thesis summary

Advanced polymers, apart from playing a major role in our daily life, are responsible for shaping the potential innovations and breakthroughs in the future. The past three years of work, summarized in this thesis, have been directed towards increasing the knowledge of different advanced polymers and their technologies of application, aiming to expand the human knowledge a little bit further, as well as bringing it closer to industrial applications and thus, produce a potential impact in our lives.

This thesis has been divided into six chapters, comprising first, a **general overview** of polymers, their classification, reaction mechanisms in polymer chemistry, their main differences thermal behavior, and an exemplification of the polymers versatility by introducing polyurethanes. Additionally, this chapter explains the concept of advanced polymers with special emphasis on self-healing polymers and on Advanced Manufacturing as a transversal technology for the application of polymers. Last but not least, a small review on why those polymers and technologies represents a capital tool for future technological applications and their current needs is offered.

In the second chapter, the **thesis objectives** are summarized and presented.

The third chapter is dedicated to the **development of an innovative self-healing system** able to work at very low temperatures aimed for high demanding fields such as aeronautics, aerospace, automobile, or windmill applications. The main research is summarized in a scientific journal published under the DOI: 10.1016/j.compositesa.2021.106335 and an impact factor of 7.664. The selection of the healing agents, the ratio,

the optimal catalyst, the microcapsule synthesis, the dispersion of the whole system in commercial epoxy resins and finally, the overall self-healing efficiency were studied.

The fourth chapter is devoted to the study of the structure-properties relationship within the **synthesis of Polyurethane-acrylate (PUA) hybrid polymers**. Although the final aim of those polymers is the use as novel soft material for 3D-printing applications in the health field, the generated library holds the potential to be used in any field where PUA could be applied. The study on the polymer synthesis and characterization has been published in a peer reviewed journal under the title of "*Synthesis of UV-Curable Polyurethane-Acrylate Hybrids with tuneable hardness and viscoelastic properties on-demand*", DOI: 10.1039/D2MA00228K. Additionally, its use as a versatile 3D printing material has been also demonstrated in the "*QuirofAM"* project co-financed by ACCIÓ and the European Union through the European Regional Development Fund (ERDF) under grant COMRDI16-1-0011-03.

In the fifth chapter is introduced a summary of the most remarkable advances generated in a state-of-the-art **3D-bioprinting platform**. The principal focus of the developed platform is the high-throughput manufacture of cellular models. The reported developments were generated during a 6-months internship in an Australian company within the PhD (*Inventia Life Sciences*).

Finally, in the sixth chapter, the **conclusions** of the work undertaken in this thesis are presented to provide a visualization of the overall advances and impact generated through this work.

TABLE OF CONTENTS

CHAPTER

1

GENERAL BACKGROUND

1.1 Precedents in polymer science

A simplistic overview of polymers consists of describing them as a series of smaller molecules called monomers that repeat over time. Even more, the term polymer derives from the Greek suffix “poly” (several) and “meros” (parts). Even though this statement is completely true, the overall complexity and potential of polymers reach far beyond to a point that they can be found in fields ranging from commodity plastics to compose the very backbone of life itself.

Although polymers have been with us since the dawn of human history, it was not until the 19th century that scientists started making small steps towards a new age. The beginning of polymer science is set approximately with the discovery of the process of vulcanization by Charles Goodyear in 1844, when with a little bit of serendipity, mixed while heating natural rubber with Sulphur. Almost a century later, the works of Leo Baekeland in 1907 set a milestone in the use of synthetic polymers by the creation of Bakelite, a thermosetting phenol-formaldehyde resin. Nonetheless, the full incorporation of polymers into our lives came with WW2, where shortage of conventional materials led to the research, discovery, and implementation of what are now our everyday plastic materials.

Thanks to its internal structure and molecular arrangement, polymers possess a unique behaviour and interesting properties that can be modified to better adapt to almost any situation.

1.2 Classification of polymers

From the wide variety of possibilities ahead, polymer materials in this chapter have been classified through their performance (commodity, engineering or advanced), their polymerization mechanism (step-growth or chain growth polymerization), their structure (chemical and physical), or how they behave when heated (thermoplastic or thermosets). Those classifications provide a first glance to the wide polymer's world directed to improving the understanding of the studies provided afterwards.

1.2.1 Properties and applications of polymers

Based on their qualities and cost, plastic materials are typically classed as commodity polymers or engineering polymers.

Commodity (general) polymers are cost-driven and normally, less expensive than engineering plastics. Moreover, commodity plastics account for around 80 to 85% of the overall plastic consumption worldwide. They are often known as general-purpose plastics and are inexpensive and simple to process. They have low-to-moderate strengths and demonstrate low glass transition temperatures. Their typical working temperature oscillates between 60 to 150 °C and therefore, due to their moderate characteristics, they are utilized in less demanding applications than engineering plastics such as packaging, toys, and container applications. Typical examples of commodity plastics are polypropylene (PP), Polyethylene (PE), Polystyrene (PS) or polyvinyl chloride (PVC), among others.

Engineering polymers are defined as those which possess enhanced performance and general properties. Their superior mechanical

performance, chemical stability and thermal capacities, allows the use of these materials in specific, highly demanding applications such as aeronautics or aerospace fields. It has been in these applications where they have demonstrated the potential to replace typically used materials such as metal or ceramics. These polymers tend to have higher costs due to the larger amount of engineering resources engaged in their development and manufacture. As example, polysulfones (PSUs), polyimides, aramids, polyketones or poly(phenylene ether) are typical polymers included within the definition of engineering polymers.

There is an additional category of polymers beyond commodity and engineering: Special polymers.

Special polymers present chemical moieties or physical fillers in their polymeric chains, thus providing novel properties and behaviours. Smart or advanced polymers are types of special polymers which possess the ability to respond to external stimulus or withhold properties beyond what would be possible with commodity or engineering plastics. Special polymers englobe most of the research and works regarding novel developments in polymer science.

1.2.2 Polymerization processes and mechanisms

The term polymerization refers to the chemical reaction in which molecules with high molecular weight are generated from monomers. The two main types of polymerization reactions are the chain-reaction polymerization (also called chain-growth) and step-reaction polymerization (which is also known as polyaddition).

1.2.2.1 Chain-growth polymerization

The chain-growth polymerization mechanism usually involves at least two chemical entities and can be typically divided into three different steps. The basic two chemical components are a monomer, which almost always possess at least one unsaturated group, and an active centre, responsible of triggering the reaction. The five different polymerization types used in the synthesis of addition polymers are radical polymerization, ionic (cationic or anionic) polymerization, coordination catalytic polymerization (named also Ziegler-Natta polymerization), ring-opening polymerization and living polymerization.[1]

The first step of the chain-growth polymerization reaction is the Initiation. It starts with the generation of an active centre (i.e. for radical chain-growth polymerization is a free radical derived from a catalyst). When this active centre (primary) meets a monomer, it reacts by breaking apart the unsaturation, linking with the active centre but in exchange, transferring the capability to react to its structure, thus generating a growing active centre (for radical polymerization, the free electron is transferred to the added monomer) (Scheme 1.1).

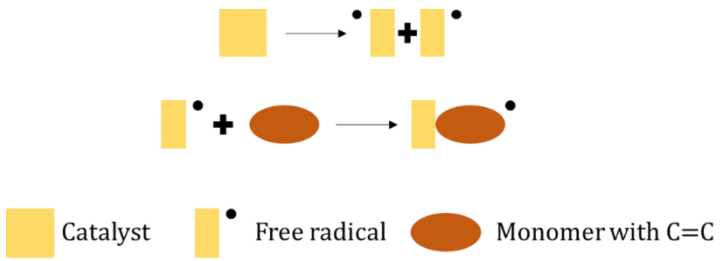

Scheme 1.1. Initiation process in the Radical Chain-Reaction polymerization. The catalyst first decomposes into free radicals which in turn, react with monomers containing unsaturated groups and the active center (free electron) is transferred to the chain end.

The second step is the propagation. In this process the polymer chain is generated by the repetitive reaction of monomers with a molecule containing the growing active centre (which, is a free radical charge, in radical polymerization, an anion for anionic polymerization or a cation for cationic polymerization). This way, a new monomer attaches to the existing chain, breaking the unsaturated bond and passing the active centre through the chain, ready to react again with another monomer (Scheme 1.2).

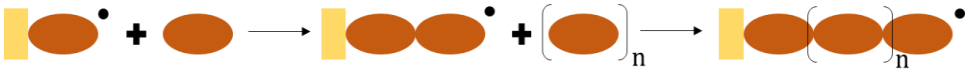

Scheme 1.2. Propagation process in the Chain-Reaction polymerization. The initiated chain with the free radical reacts with more monomers, bonding them and transferring the electron to the chain end.

Since the incorporation of a monomer to the growing polymer chain involves the conversion of the π bonds from the double bond to σ bonds, the polymerization reaction is exothermic. As the overall system's energy is lowered when this reaction takes places, it is a thermodynamically favoured reaction at low temperatures. In other words, the bonds generated in the polymer are more stable than the initial double bonds from the monomers. The final step is the termination. It takes place when two active centre meets. This occurs between two end-chains of the growing polymers or with some left over of the primary active centre.

For the specific example of the radical chain-growth polymerization, the two free electrons, acting as active centres, combine to create a stable simple bond between atoms (Scheme 1.3). From the kinetic point of view,

the locus of the polymerization is located only in those few chains where an initiator has triggered the process and contains an active centre.

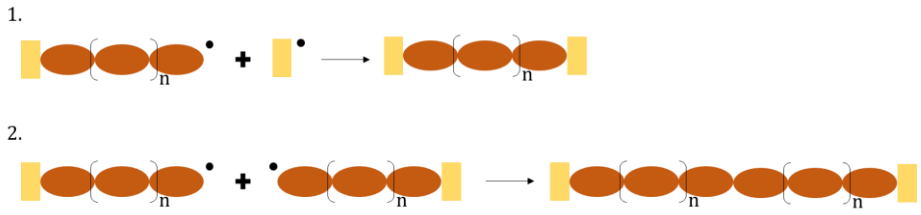

Scheme 1.3. Scheme of the termination process in the Chain-Reaction polymerization. The propagated chains can finish the reaction by either reacting with an initial free radical (1) or by encountering another chain with a final free electron (2).

An alternative end-step for the polymerization mechanism in step-growth reaction is the chain-transfer. In this process, the active centre moves from one growing chain to an inactive molecule or polymer chain, terminating one polymerization process but starting another.

Interestingly, living polymerization is a class within chain-growth mechanism in which neither the termination nor chain-transfer step exists. In the system, all monomer is depleted, and the chains remain active. If more monomer is added, the reaction will go on. Due to the extreme control of the polymer growth that can be achieved in living polymerization it is found in most of the developments in within polymer science. Living polymerization can also be divided into different types depending on the nature of the used active centre.

1.2.2.2 Step-reaction polymerization

Step-growth polymerization reaction involves the use of at least two different types of multi-functional monomers with end groups capable of reacting with one another, forming this way, a chain of alternate monomers.

Although the minimal monomer's functionality has to be two for the synthesis of a linear polymer (di-functional) it can be higher, thus generating a ramified structure. Step-growth polymerization mechanism can be divided into (poly)addition or (poly)condensation polymerization processes. The main difference between them is that, in condensation polymerization, a small molecule such as water or hydrochloric acid (HCl) is generated as by-product (Scheme 1.4). Due to being processes with high activation energies, polycondensation reactions need catalysts and high temperatures to fasten its kinetics and reach high molecular weight products.

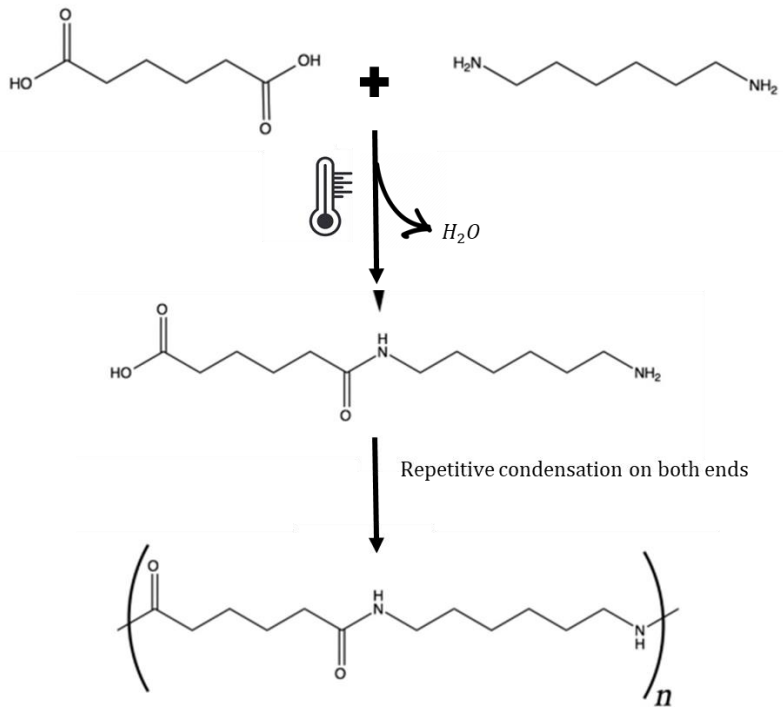

Scheme 1.4. Polycondensation reaction scheme of adipic acid and 1,6-hexamethylenediamine to produce nylon 6,6. It can be seen that for the reaction to occur, needs temperature. On the polymerization process, a molecule of water is released for each reaction between the acid and the amine groups. This reaction will generate a complete linear polymer unless a monomer with a higher functionality than the current ones is added.

1.2.2.3 Ring-opening polymerization

Ring-opening polymerization (ROP) is one of the main processes of producing synthetic polymers within chain-growth polymerization mechanism.

Although ROP reactions follow the initiation, propagation, and termination phases (Scheme 1.5), from the kinetic point of view, due to the similar speed between initiation and the rest of steps, ROP is not completely considered as a chain-growth reaction.[2,3]

The overall addition of monomers to the growing chain is similar to the observed for polycondensation processes but it does not come followed by the loss of a small molecule as subproduct (except for the ROP of Leuchs' anhydrides or the radical ROP of 2,2-diphenyl-4-methylene-1,3-dioxolane).

In ROP, a reactive centre such as a radical (RROP), cationic (CROP) or anionic (AROP) can attack a ring of a cyclic monomer, thus releasing the ring strain which turns into a more stable or more entropic structure while creating polymer chains.[4] ROP is a common synthetic route for many commercially polymers, e.g., polyesters (poly(lactic acid), poly(ethylene glycol), poly(norbornene) or polysiloxanes.[3] Another relevant pathway is the metathesis ROP (ROMP) (Scheme 1.5).

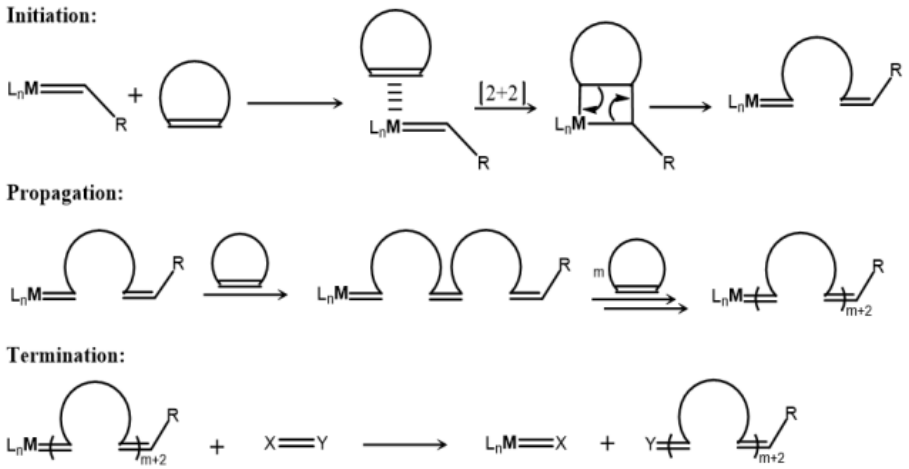

Scheme 1.5. Simplified general mechanism of Ring-Opening Metathesis Polymerization (ROMP) of cyclic olefins.[6]

In ROMP there are two main components that allow the polymerization process to thrive. Even though the driving force of the process is the energy released from the ring strain, a metal catalyst is also needed. As the number of molecules in the overall process is reduced (generating a positive value for $-T\Delta S$), the released ring strain enthalpy must be high enough to compensate and move forward the reaction (have a negative value of free energy ΔG).

$$\Delta G = \Delta H - T\Delta S$$

Equation 1.1. Gibbs free energy equation. For the reaction to be spontaneous, the ΔG value must be negative.

The first metal catalysts used for ROMP reactions were undefined systems. A milestone was set when Schrock, Grubbs and Chauvin won the Nobel Prize in 2005 for the works on the synthetic and mechanistic pathways of well-defined catalyst complexes of Molybdenum and Ruthenium (Figure 1.1).

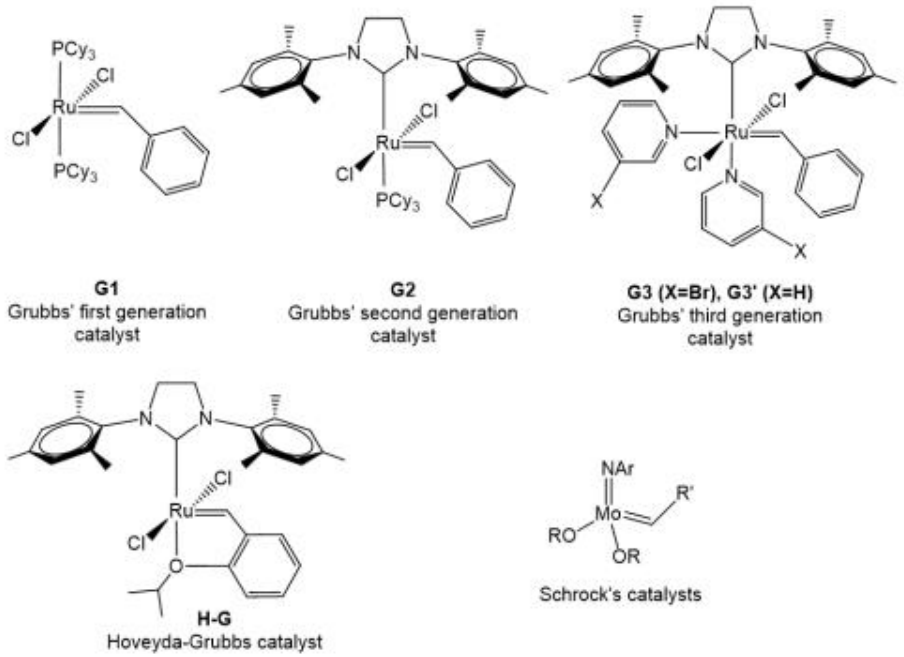

Figure 1.1. Different Grubb's and Schrock's catalysts structures.[5]

Those catalysts provided with the potential development of a much wider variety of synthetic polymer structures. Plenty of new generation of catalytic structures leading towards improved robustness or refined kinetics has been synthesized since those first studies.[6]

1.2.3 Polymer structure

The molecular structure of polymers, also known as macromolecular architecture, describes how monomers transform first into monomeric units and afterwards organize into macromolecules. In this description is included the type, composition, sequence, microstructure, and tacticity of the monomeric units that make up polymer chains (chain structure), as well as their molar weight and its distribution, how polymer chains are

connected inside the macromolecule (topology) and any potential attached functionality.[7]

The simplest structure that polymers can be found is linear (Figure 1.2, a). Linear polymers present a single, long continuous chain without any attachments or ramifications. If some of the monomers present several reactivity groups, either a branch or a crosslinking point can be generated. Branched polymers (Figure 1.2, b) are considered those who present lateral chains of small molecular weight. Crosslinking (Figure 1.2, c) occurs when some of these branches attach between main chains covalently bonding the two structures. If within the same molecular structure there are enough crosslinking points, a network can be generated (Figure 1.2, d).[8]

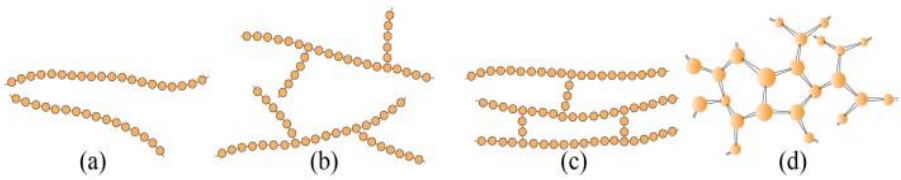

Figure 1.2. Figure from 14.7 in Callister.[8] Representation of the basic polymer structures. (a) linear, (b) branched, (c) cross-linked and (d) network. Each dot represents a monomer molecule.

When a polymer is composed of only one type of monomer, the name given to that macromolecule is homopolymer. If two different or more monomer species are used the generated molecule is referred as heteropolymer (for example, for two is labelled as copolymer and if there are three different monomers within the structure, it is called terpolymer).

If the synthesized copolymer follows a regular periodicity among the two different used monomers, it is known as alternating copolymer (Figure

1.3, b). In chain-reaction polymerization where, in case of using two different monomers do not necessarily need to react with each other, structures of random copolymerization (Figure 1.3, a), block copolymers (Figure 1.3, c) or graft copolymers (Figure 1.3, d) can be found.

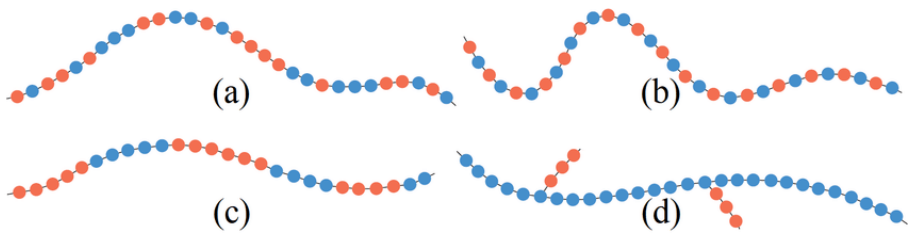

Figure 1.3. Visual representation of different types of copolymer chemical structures. Blue and red dots represent two different kind of monomers linked through covalent bonds. a) the depicted structure is a random copolymer. b) the depicted structure is an alternating copolymer. c) the depicted structure is a block copolymer and d) the depicted structure is a graft copolymer.[9]

The variation on the arrangement of the pendant groups along the main backbone is referred as tacticity. Tacticity is mainly classified as isotactic (if all the pendant groups are on the same side of the chain), syndiotactic (when the pendant groups follow a regular alternating pattern) or atactic (when the pendant groups are arranged randomly through the hydrocarbon chain). Moreover, a single polymer chain could present more than a single tacticity in different points of their structure. Tacticity can affect the mechanical, physical and chemical properties of the polymers.

The presence or absence of symmetry in the 3D chain configurations of the polymer can result in crystalline or amorphous physical structure.

Crystalline structures are only observed in polymers with a regular structure (homopolymers, alternating polymers or block copolymers) with highly ordered arrangement of their chains. Another key parameter

of crystalline polymers is that they present a characteristic melting temperature (T_m). The melting temperature is the critical temperature at which crystalline regions are able to flow.

Usually, the crystalline segments have a preference of orientation and generate anisotropic effects on the final product that can be further exploited to fit into certain applications. The presence of asymmetry within the polymer (normally in the shape of lateral chains that could sterically block ordered structures) can prevent the generation of polymeric crystals.

Amorphous polymers present, per definition, a completely disordered structure. Polymeric chains are randomly entangled and do not present a defined T_m but they are more defined by the glass temperature (T_g). When the polymer is at a temperature below its T_g, the molecular chains are rigid, and the material behave like a solid. If the temperature is above the T_g, the free volume between the molecular chains, increases and the material behaves as a pseudo-liquid. The lack of regular inner structure implies also that those amorphous polymers are isotropic (present uniform properties in all directions) and transparent (there are no light interferences through the material).

In the internal structure of some polymers, it is possible to find simultaneously crystalline and amorphous regions (Figure 1.4). When these two structures coexist, those polymers are labelled as semicrystalline.[10] Interestingly, the presence of crystalline regions within a polymer can be tuned. When the polymers are melted, the lack of supramolecular forces prevents any order and therefore, all thermoplastic polymers are in amorphous state.

If the polymer cooled slowly after the melting process, chains have more time to organize themselves in crystalline form. Otherwise, if a melted polymer is cooled rapidly, the molecular chains do not have enough time to successfully orient themselves and thus, are solidified as amorphous. Semi-crystalline polymers possess both a T_g and a T_m.

Semi-crystalline polymers are solid until the polymer is heated to its melting temperature, when is reached, when they demonstrate a fluid behaviour. However, the main difference with fully crystalline polymers is that they begin to soften above their T_g, which is lower than the melting temperature. When the material has a temperature between its T_g and T_m, the material exhibits large elongation capabilities under relatively low applied loads, this is known as rubbery region.[11]

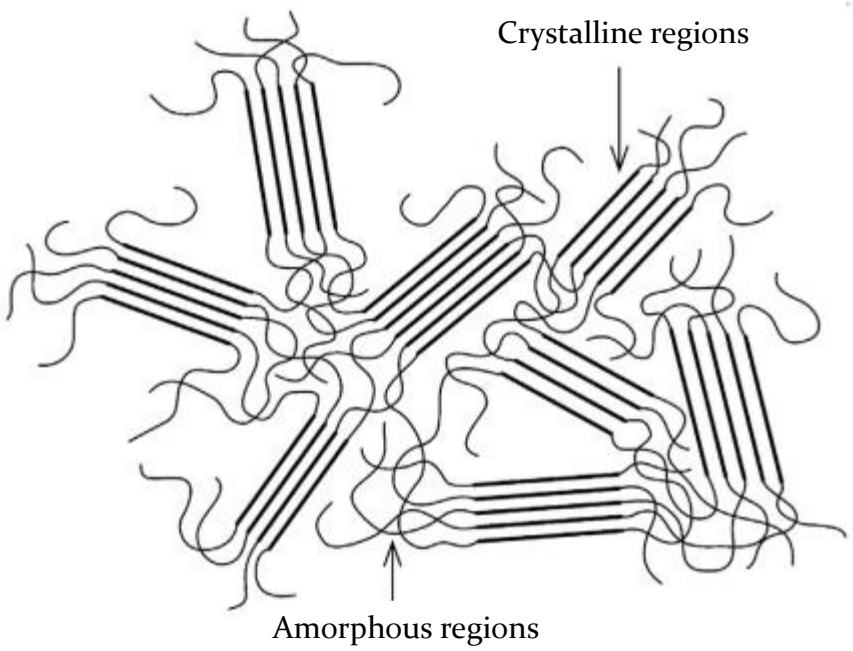

Figure 1.4. Representation of a semi-crystalline polymer model with miscible amorphous and crystalline regions.[11]

1.2.4 Thermal behaviour

Depending on how the polymers behave when heated, they can be classified as thermoplastic or thermoset. Thermoplastic polymers can flow when enough heat is applied and thus, can be remoulded, while thermoset polymers have a more crosslinked network that prevents any kind of flowability even with higher temperatures. This means that while thermoplastic polymers can be recycled, thermoset materials degrade before flowing and thus, cannot be recycled as material.

In the inner structure of thermoplastic polymers is based on covalent bonds generated by either addition or condensation polymerization. Between the main chains, secondary and weaker supramolecular forces appear, stabilizing and maintaining together the overall macromolecule. These secondary forces are easily broken when thermal energy is applied but appear again at low temperatures. Therefore, thermoplastic polymers can present a physical rigid structure that can be melted and then, re-shaped in a new way and maintaining that new structure once cooled. Thanks to the additional freedom of the polymer chains compared to the crosslinked chains of thermoset materials, the total or partial arrangement of the thermoplastic segments can be produced randomly (thus generation amorphous segments) or ordered (crystalline).

Although thermoset polymers also present those supramolecular forces, the number of covalent links that cannot be weakened by heat is much higher than in thermoplastics, preventing them to melt. Nonetheless, there are some benefits of having a higher crosslinked network such as enhanced mechanical properties (creep, deformation, dimensional stability…) or increased thermal stability and insulating properties. Thermosets are typically amorphous. Once fully polymerized, the highly

crosslinked, random three-dimensional network prevents any further chain movement, inhibiting thus the potential rearrangement into generating a regular or crystalline structure. Nonetheless, semi-crystalline thermosets can be synthesized under controlled synthesis procedures to generate polymeric materials tailored to specific (and normally, high demanding) applications.[12]

1.2.5 Polyurethanes

The structure-properties relationship of polyurethanes (PU) allows this kind of polymers to be applied almost everywhere. Thus, through modification of the initial raw materials or the used synthesis procedure, a perfect insulator, a foam, a liquid coating, an adhesive or even a vascular stent, can be obtained, among very others (Figure 1.5).

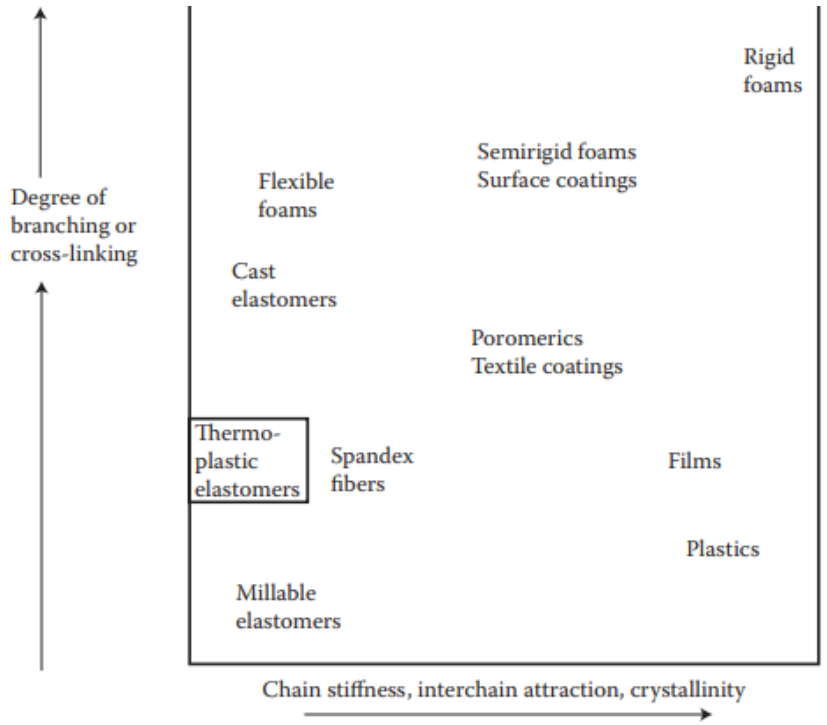

Figure 1.5. Structure-property relationships in polyurethanes.[13]

PU was first developed in 1937 by Dr. Otto Bayer and his co-workers[14] attempting to synthesize an alternative material for rubber during WWII. Afterwards, the industrial production of this polymer, quickly escalated until becoming one of the most used, versatile and studied materials world-wide.

The urethane bond (carbamate), generated by the reaction of an isocyanate group from a polyisocyanate and an alcohol from a polyol, is the structural base of a polyurethane (Scheme 1.6).[15] However, besides urethane groups, a typical PU may contain aliphatic and aromatic hydrocarbons, esters, ethers, amides, urea or isocyanurate groups too. Within the synthesis process, the presence of catalyst, the molecular structure of the polyisocyanate, the ratio between components or the presence of other active hydrogen groups such as those from water or amines (apart from alcohol groups), several side reactions may occur which affect the final properties of the polymer.

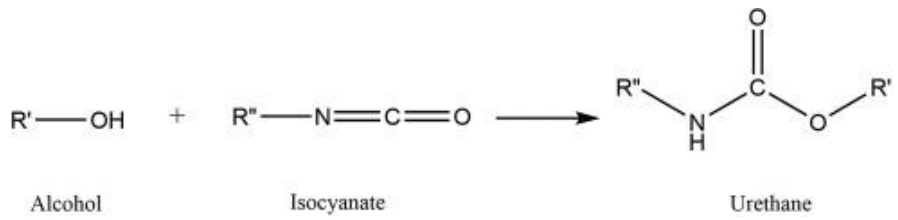

Scheme 1.6. Urethane group formation from the reaction of an active hydrogen from an alcohol and an isocyanate.

Polyisocyanates can be generally divided into aromatic, that typically present improved mechanical and reactive properties or aliphatic, generally much less toxic, and light stable. Due to the delocalization of the electronegative charge from the carbon of the isocyanate group into the aromatic substituent, aromatic isocyanates are usually more reactive than its aliphatic or cycloaliphatic counterparts. Similar increase in

reactivity is found when an electron withdrawing substituents are located near the isocyanate group. Some common examples of the most used isocyanates are represented in Figure 1.6.

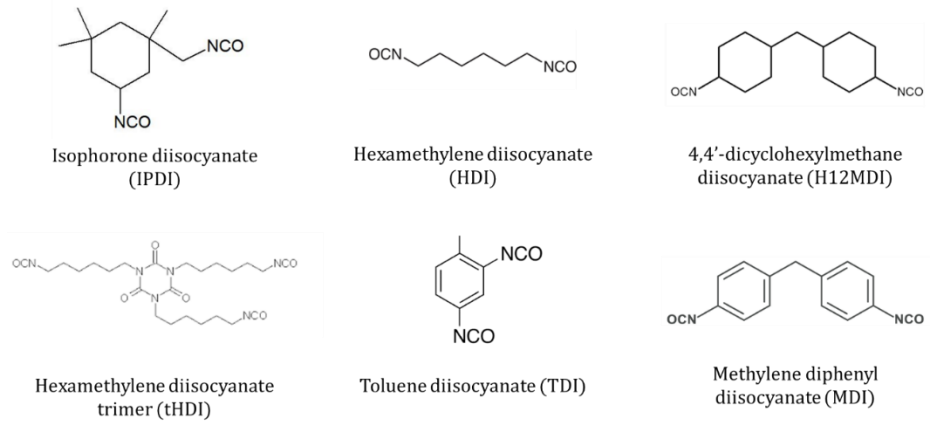

Figure 1.6. Structure overview of a few representative aliphatic, cycloaliphatic and aromatic polyisocyanates.

Additionally, PU properties depend greatly on the exceptional polymer microstructure of alternating soft and hard blocks. Soft block or soft segment (SS) within PU are composed of long (between 400 and 6000 Da), flexible, and elastic polyol chains with low glass temperature (T_g) that can be from either polyether, polyester or polycarbonate and are organized randomly in the polymer macrostructure (amorphous). Depending on the molecular weight and linearity of the macrodiol, the properties of the obtained PU will vary. Although historically the main source of polyols for PU synthesis have been from non-recyclable sources, efforts towards moving to renewable resource-based products have been pursued during the last years.[16] The rigid, highly polar, hard segment (HS) comprises both (poly)isocyanates and a low molecular weight polyol or amine used to increase the overall HS molecular weight, named chain extenders. The HS, with internal supramolecular interactions (hydrogen bonds), is the main responsible for the physical crosslink and internal

mechanical reinforcement of the polymer, leading it to behave as a crystalline polymer.

Depending on the type and structure of the chosen starting monomers, PU can be found to perform more as a crystalline, segmented (semicrystalline) or amorphous polymer. Mechanically, PU behaves as a viscoelastic non-ideal solid, having a viscous and an elastic response against an external excitation. Moreover, the effect of those responses can vary depending on both internal and external factors such as crosslinking density, moisture or temperature.

Depending on the desired final application, PU can be manufactured as thermoplastic (TPU) and thermoset (TS). The transition from TPU to thermoset can be produced during its synthesis, processing or post-processing stages. For TPU, the chemical reaction is generated between a macrodiol, a diisocyanate and a dihydroxy or diamine chain extender. For thermoset PU, instead of using a small difunctional molecule as chain extender, tri or higher functional molecules are used aiming to generate a more crosslinked network. Nonetheless, the thermodynamic differences between hard (crystalline) and soft (amorphous) segments induce molecular segmentations, obtaining thus a matrix from soft domains reinforced of discrete and ordered hard segments (Figure 1.7).

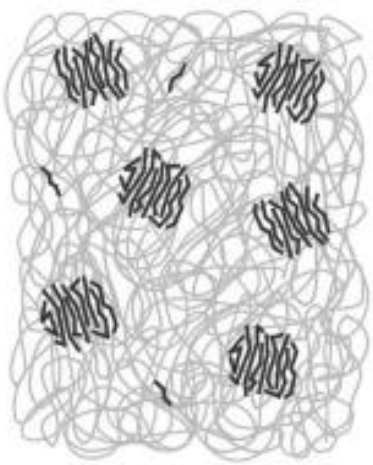

Figure 1.7. Schematic representation of the phase separation in polyurethanes.

This microphase separation is what allows PU to perform so well as an elastomeric material. The degree of compatibility between distinct phases is determined by several factors, including temperature, crystallinity and previous thermal history. In comparison to traditional rubbers, elastomer PU are generally manufactured as thermoplastic polymers since they are easier to process and recycle.[13]

On top of the potential variables derived from the PU building blocks, the synthesis procedure can also affect greatly the final behaviour of the polymer. Generally, PU can be synthetized in batch through one or two-steps procedures or by semicontinuous processes as in reactive extrusion.[17]

In one-step batch synthesis, it is mixed simultaneously a polyisocyanate, a macrodiol and the chain extender. Some additives are included in these reactions to either modify the properties, to increase the speed of it (using catalysts) or decrease the overall viscosity (use of solvents). Typically one-step synthesis of PU are carried in reactors, reactive extruders or even in continuous injection machines for moulding.

Although it is not as industrially attractive as one-step processes, two-step synthesis allows for an improved architecture control of the polymer structure. In two-step polymerization, first a pre-polymer with terminal isocyanate groups is synthesized and it is later reacted with the chain extender in the second step, increasing greatly its molecular weight until the reaction is completed.

The use and content of toxic volatile organic compounds (VOCs) drove scientists towards generating polymerization methods that avoided those components. Water-borne PU were presented as a solution for obtaining

environment-friendly and non-toxic PU. To create PU polymers compatible with aqueous media, major modification in the polymer backbone is necessary. Thus, ionic moieties known as internal emulsifiers that contain hydrophilic groups are bonded into the polymer chain and allow the material to stabilize in the water, creating a binary colloidal system.[18]

Driven with the same idea of reducing the potential associated risks of synthesizing polyurethanes, non-isocyanate polyurethanes (NIPUS) were proposed to reduce the use of potentially toxic isocyanates. NIPUs are mostly synthesized by the polyaddition reaction between a cyclic carbonate and an amine (Scheme 1.7).

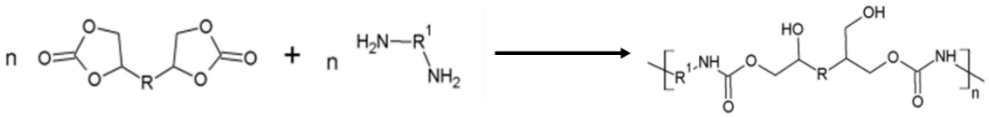

Scheme 1.7. Polyaddition reaction between a cyclic carbonate and an amine to generate (hydroxy)Polyurethanes.

However, it is also possible to synthesize NIPUS through reactions of rearrangements, ring-opening polymerizations or polycondensations.

There is plenty of bibliography and studies regarding the different strategies in NIPU synthesis, its applications, and potential future trends.[19,20]

1.3 New applications of polymers, challenges and upcoming needs

Basic commodity polymers that have been with us for more than 70 years, have already proven themselves indispensable for the day-to-day applications. However, as science, technology and the overall human species move forward, new challenges appear that push forward the frontiers of what synthetic polymers need and can do.

Generally, the creation of new polymeric materials finds its inspiration in biological systems. Biological materials possess an incredibly dynamic way of responding to external stimulus, providing an adaptative and tuneable response to the received signals and needs. Advanced polymers are those with the capability of creating a response after an external stimulus, thus replicating what is seen in nature. Additionally, the application of those novel, smart polymeric materials, are the key to true breakthroughs and innovations that help shaping the future of humankind. For clarification, in the following text advanced and smart polymers will be used as synonyms.

One of the many ways of classifying advanced materials is by the external trigger they are sensitive to. Temperature-responsive polymers are those whose, with a temperature modification can change their solubility, colour, or conformational structure. There are three main types of temperature-responsive polymers: Shape memory polymers (SMP), liquid crystalline polymers (LCP) and responsive polymer solutions (RPS).

Thanks to a deeper understanding of the biological interactions and regulations in nature and in human physiology, there are now advanced polymers synthesized and programmed to react with certain enzymes or

changes in the homeostasis, for example, with the apparition of inflammatory markers among others. Those inflammatory signals can generate physical or chemical modifications triggered through a reduced pH (with respect to healthy tissue), the presence of reactive oxygen species (ROS), the presence of matrix-remodelling enzymes (MMPs) or an increase in temperature as well as the appearance of inflammatory cells within the polymer environment that, if the polymer possesses the right backbone modifications, can devour it partially or completely.

Adapting physically responsive polymers to biological applications is leading potential solution to inflammatory-based diseases,[21,22] increasing the availability for inflammatory drugs in-site[23,24] as well as setting early diagnostics tools for the detection of "slow"-advancing diseases[25] or imaging.[25]

As our awareness of the limits of the planet grows, new technologies and materials arise to overcome long-lasting issues. As previously stated, polymers are one of the foundations of our current society. However, until not so long ago, single-use plastics were tolerated, and recycling was just another option. The realization of the ecological impact of those decisions is making society to carefully make choices regarding the materials used in their routine.

While thermoplastic polymers, due to their intrinsic structure, allow for a complete reprocessing and thus, recycling, thermosets do not have this possibility. Aiming for obtaining materials with thermoset properties but with the recycling capability of thermoplastics, researchers have introduced dynamic covalent bonds (DCB) to the backbone and side chains of the polymer. The idea is that with a certain stimulus, DCB are capable of producing a temporary but stable crosslinked network that can

break and alter the thermal behaviour of the polymer. There are two types of DCB, dissociative and associative.[26] In dissociative, the DCB are broken with a stimulus and the crosslinking density is greatly decreased. Those bonds can regenerate after certain time, allowing to reprocess the material. In associative DCB networks, the fracture and reforming of the chemical bonds occur simultaneously, maintaining stable the crosslinking density.[27]

Among the different advanced materials, and within the same idea of increasing the lifespan of synthetic materials, those with the capability of healing themselves from external damage (that could make them partially or completely lose their functions) without the need of human intervention, are considered a pillar for application and improvement in almost all fields of polymer application. Polymeric materials that possess the described qualities have the designation of self-healing polymers.

Up to this point, all the previously described advanced polymers present the capability of introducing substantial changes and improvements in a wide variety of fields. However, most of these systems are still developed in laboratory scale and, normally, with high priced products. Both factors limit greatly its further application into industrial processes and thus, have no real impact in our daily life.

Nonetheless, there are sectors where these high prices are compensated with the obtained results and are limited to low production processes. In fields such as aeronautics or health, the implementation of advanced polymers is easier and can be used as catalyst to generate further improvements in the development of those technologies, aiming to soften the entrance of those materials to become used in daily applications.

1.3.1 Self-healing technologies

Through evolution, living organisms have developed different repairing mechanisms that allow them to receive both internal or external damage and still maintain their basic functions. Although the mechanisms differ depending on the type of organism, the outcome is similar in all cases. Even though in humans the process of self-healing is continuous, it may be best exemplified and understood by exemplifying the different steps occurring during the healing of a skin wound. The healing mechanism is separated in differentiated steps. After a damage, the body suffers a change in its haemostasis and starts closing the wound by a coagulation process where several different cellular populations and biochemical signals intervene. Afterwards, other cell types as well as soluble mediators such as cytokines improve the flow of blood and more nutrients to the damaged site. This is known as an inflammatory process. Cells from the same type as their neighbours start proliferating by the presence of growth factors, and finally, the production of extracellular compounds contribute to an extremely optimized process that finishes with a new tissue almost indistinguishable from the original one. In the vegetal kingdom, high molecular weight molecules such as oligosaccharides or oligopeptides contained in a healing liquid, flows towards a wound and induce a chain of biochemical reactions that hardens the released liquid and lead to a similar macroscopic healing after receiving a damage. These chains of events have served as inspiration to researchers to develop new artificial healing pathways.

The early approaches and, in some cases, the current methods of repairing polymer materials after suffering some damages have been welding, patching, and gluing. Despite being a relatively easy and practical approach for most fields, the concerns regarding sustainability

as well as the difficulty of accessibility in components from high performing fields (aeronautic, aerospace, building…) have pushed towards obtaining improved polymeric systems which are more resistant to damage and take longer to become non-functional (Figure 1.8, (a) and (b)). An ideal self-healing system should be able to repair itself autonomously (without any kind of human intervention) and forever without any compromise in their reliability whatsoever (Figure 1.8, (d)). The reality is that the incorporation of a self-healing system is not eternal but has a limited range of recovery cycles that, nonetheless, are able to expand the service lifetime of the material (Figure 1.8, (c)).

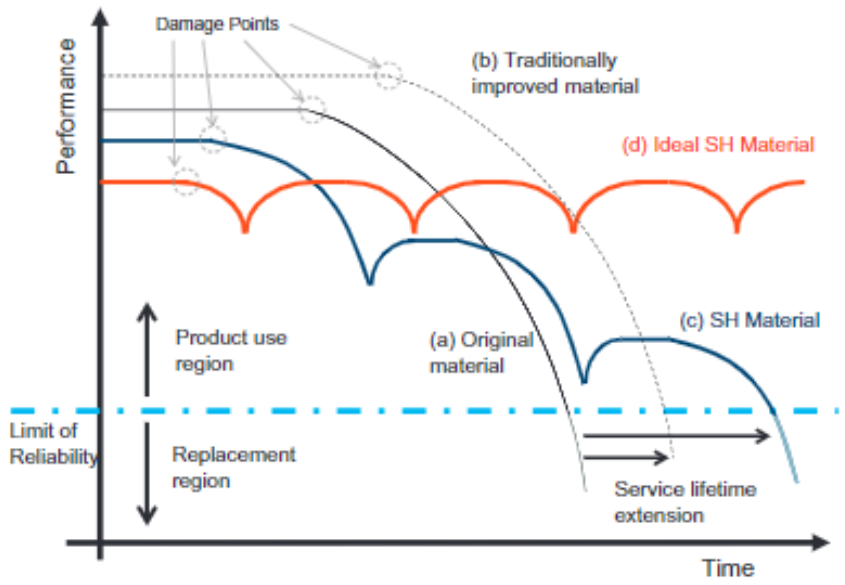

Figure 1.8. Material's performance over time graph comparing an original material (a) with an improved version (b) and with the incorporation of a self-healing mechanism (c). (d) is used to exhibit how an ideal Self-healing material should behave. There is also showed the limit where the material is no longer useful for its purpose (reliability). Obtained from Aguilar et al.[28]

Self-healing polymers can be divided into two main categories depending on their self-healing mechanism. If the polymers have inherent properties due to its molecular structure, they are classified as Intrinsic or

homogeneous self-healing polymers. Typically, the intrinsic approach comprehends both physical and chemical mechanisms such as interchain diffusion, supramolecular bonding or dynamic covalent bonds, among others. Plastic materials whose self-healing capabilities are provided by external healing agents that are embedded within the polymer matrix (such as in microcapsules or in a vascular system) are classified as extrinsic or heterogeneous.

1.3.1.1 Extrinsic self-healing systems

The first synthetic self-healing material as it is known today, even though some early works already had played with the concept, was reported in 2001 when White *et al.*[29] dispersed microcapsules containing a healing agent (Ring Opening Polymerization monomers) and a metathesis catalyst (Grubbs) within a thermoset epoxy resin. When the material was damaged, followed by the appearance of micro-cracks, the imbedded microparticles also fractured, releasing the core's content and filling the generated crack. After a short period of time where the healing agent is left to flow and cover the maximum volume of the damage, the catalyst triggers the polymerization reaction, bonding the two faces together again and thus, repairing the damage (Figure 1.9, A). Five different types of encapsulated healing agent systems have been proved to be effective (Figure 1.9).[30] At least one healing agent is encapsulated in the single-capsule system, which can be a reactive chemical, a solvent, or a low-melting-point metal. The capsule/distributed catalyst healing technique involves the encapsulation of a self-healing agent into brittle capsules and dispersing the catalyst/trigger or a second type of capsules throughout the matrix.[30,31] A final approach is the synthesis of all-in-one particles.

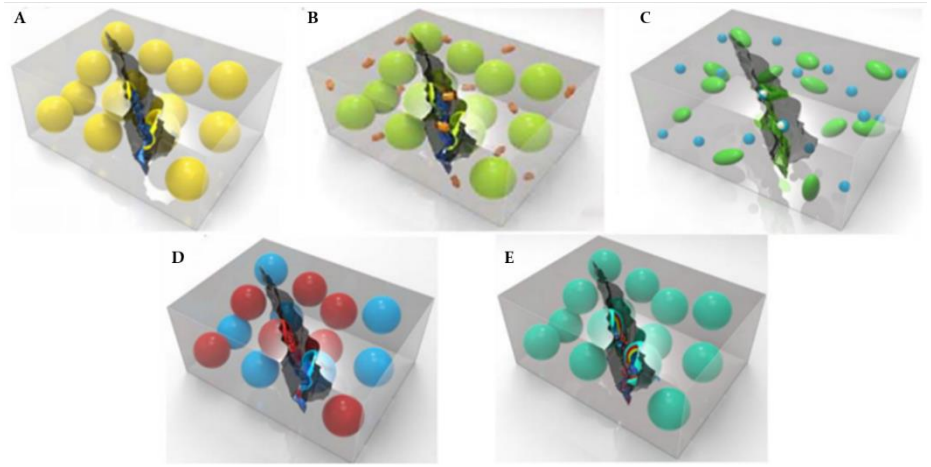

Figure 1.9. Summary of capsule-based (extrinsic) self-healing systems, (A) single capsules, (B) capsule (green)/dispersed catalyst (orange), (C) phase-separated droplet/capsules (green), (D) double-capsule (blue capsules with hardener, red capsules with healing agent) and (E) all-in-one microcapsules (multiple shell walls depicted with different colors). Figure from Zhu et al.[30]

There are certain parameters that need to be controlled to achieve a successful self-healing reaction. First, both the monomers used as self-healing agents and the embedded must have good stability to not react with themselves after being stored for long periods of time nor being deactivated when in contact with the polymer matrix. Moreover, they need to exhibit enough flowability to fill the generated cracks by capillarity and the reactive window with the other chemical trigger must be high to promote a quick healing but slow enough to provide with a full crack covering. Additionally, the mechanical properties of the final polymer should match as much as possible those of the matrix.[32]

Despite being the first approach matured for the SH technology, over more than 20 years of work in capsule-based extrinsic systems have pushed the technology towards being a reference in several high demanding fields due to its ease of application, the variety of the healing chemistry used, its self-healing capacity and the potential for high production manufacturing.[33,34]

With all, micro-capsule-based systems possess an inherent flaw regarding the potential cycles of self-healing of the material. Once the content of the particles is released and hardened in a certain area of the material, there is no possibility of healing again and thus, the mechanism is limited to one autonomous reparation per volume before becoming conventional again.

Even presenting this limitation, several attempts towards the generation of commercial self-healing materials, have sustained themselves in the application of microparticle-based extrinsic self-healing systems. More specifically, in fields where materials already possess longevity and used in locations with limited accessibility such as thermoset composite materials.[30]

Attempting to complement the first self-healing technology, vascular extrinsic systems were designed trying to replicate nature's design for incorporating a network of vessels able to transport substances through the body.

The research of C. Dry *et al.*[35], which proposed a smart-concrete system with embedded channels capable of delivering an adhesive system when a crack appeared, is considered the first approach towards vascular self-healing system. Nonetheless, the vascular self-healing system proposed by Toohey *et al.*[36] is considered pioneer towards setting the bases for the upcoming research in this heterogeneous self-healing area.

Although the first manufacturing of vessels was obtained by direct ink writing (DIW)[36] of sacrificial material afterwards filled with the healing monomer, there are other techniques and materials that allow the same introduction of the vessels within the composite structure. As an example, sacrificial fibres, usually from polylactic acid (PLA)[37], are

originally woven with the tissue sheet, then removed and replaced with the healing agents of choice following the composite manufacture process. Other approaches involve the use of hollow glass fibers[38] or the incorporation of electro-spun core-shell fibres, which are not in need of removing processes as they already contain encapsulated the self-healing system.[39] Similar to capsule-based systems, vascular self-healing chemistry are capable of holding different types of self-healing monomers that can either react in contact with an embedded catalyst[40] in the matrix or use an interpenetrating network with two different vascular systems that contain monomers capable of reacting with each other when in contact such as a two-part epoxy system such as the one developed by Hansen *et al.*[41]

Since its proposal, vascular self-healing systems have been thoroughly studied due to the potential variety of healing agents to be used, the possibility of being refilled and thus, increase their healing cycles and the large-scale damage that can be healed. However, problems of proper scale-up processes, the limited number of healing cycles and the manufacturing capabilities hold back the potential and the implementation of this technology.[42]

As an overview, due to chemical differences between the repairing agents and the polymer matrixes, extrinsic self-healing polymers are mostly limited to restoring the mechanical performance and are not aiming to extend the material's functionality over time.[43]

1.3.1.2 Intrinsic self-healing systems

While extrinsic self-healing materials need an external structure containing healing substances, intrinsic self-healing polymers contain moieties with reversible interactions within their polymer backbone.

Those added structures can be finely tuned through modifications in the polymeric architecture to respond to specific stimuli or to work under determined conditions. Intrinsic self-healing materials ought most of their capabilities to an increase in the polymeric chain mobility in the damaged area. The application of an external stimulus (UV light, temperature, electrical charges…), enable a temporary, focused and significative increase in the inter-chain mobility followed by a process of bond restoration.

Typical dynamic bonds present in intrinsic self-healing systems are either physical, chemical or a combination of both. The most accepted theory on how physical healing is produced is the one proposed by Wool and O'Connor in 1989.[44] In their work, represented in Figure 1.10, they explained how the molecular inter-diffusion takes place when the chain mobility is enhanced by either increasing the temperature above the polymer's glass transition temperature (T_g) or the incorporation of a solvent, leading to chain entanglements and therefore, the material's healing.

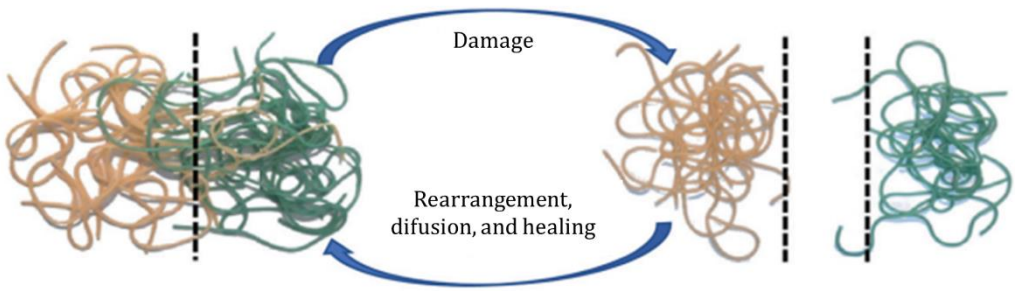

Figure 1.10. Schematics on how inter-chain diffusion on physical self-healing processes works.Obtained from Islam et al.[33]

Beyond the molecular design and composition, intrinsic self-healing materials are rather limited in the area of damage that they are capable

to heal. In those systems, bonding generation occur at the nanometric scale and therefore, the general self-healing effect can only be achieved at the micro-scale. Therefore, in order for the self-healing system to work, the damaged interfaces should be macroscopically close enough to each other to successfully promote physical interactions and the overall reorganization process.

Aiming to create an optimal commodity self-healing material with good mechanical behaviour and high healing efficiencies, one of the current approaches is based on the combination of covalent dynamic bonds with supramolecular, non-covalent interactions.

However, as their functionalities remain latent most of the time, intrinsic systems need specific conditions and stimuli to trigger the reactions and start the healing mechanism. This need of an additional parameter is one of the main factors limiting their incorporation in a variety of fields where a fully autonomous system is needed.

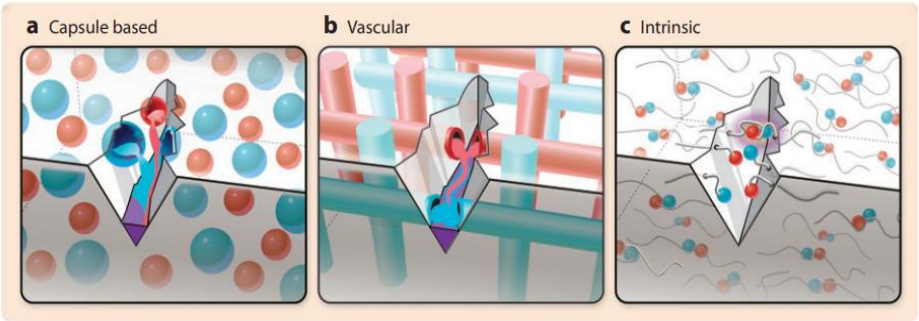

Figure 1.11. Graphical overview of the different approaches towards achieving self-healing materials. a) Extrinsic, capsule-based self-healing. In this approach the self-healing monomers are embedded in microcontainers and their content is released upon integrity failure from the shell. b) Vascular self-healing. Instead of using discrete containers distributed through the material, this approach mimicks the vascular system found in nature to distribute self-healing monomers through the material. c) Intrinsic self-healing materials have the "dormant" functionality of reorganizing themselves through a variety of physical or chemical pathways, thus recovering themselves from generated damages indefinitely. Figure from Blaiszik et al.[32]

Even though each technology presents their benefits and drawbacks, they can be used as complementary due to the healing capacity they possess. As was explained perfectly by Blaiszik *et al.*[32], while most intrinsic systems can only recover small damages as they require proximity, extrinsic systems based on capsule or vessels can deliver more healing agents towards the damaged area. As, per definition, an ideal heal-healing system would be the one capable of both maintaining the material stasis and recover from any medium-sized damage received, both approaches should be seen not as competitors but as complementary towards the same end goal (Figure 1.12).

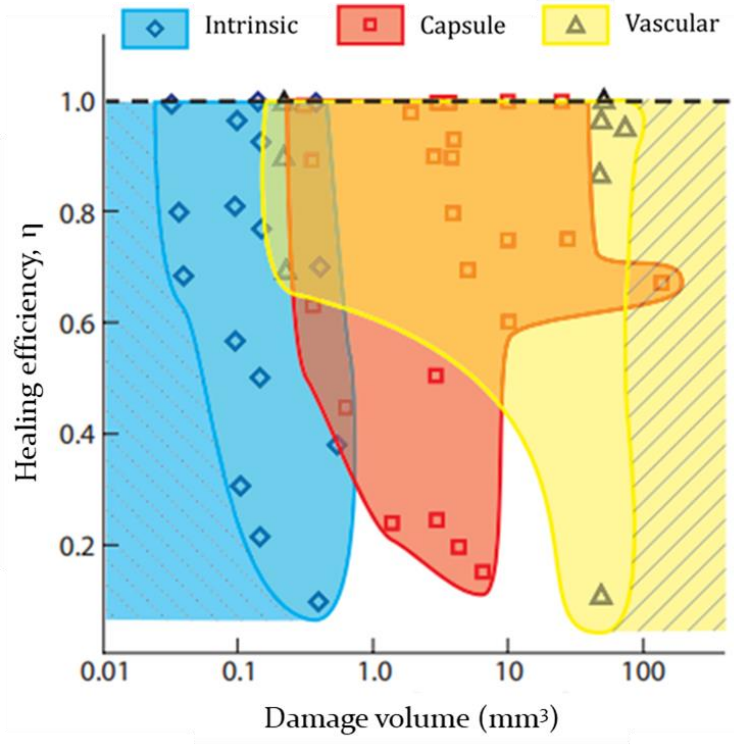

Figure 1.12. Performance map for self-healing technologies. It can be seen how the intrinsic system covers the smaller produced defects while extrinsic-based systems are able to heal large damages. Figure obtained from Blaiszik et al.[44]

1.3.1.3 Healing evaluation

Although the self-healing effect is generated at the molecular scale, it is measured macroscopically by analysing different mechanical properties. In typical self-healing quantification assays, a bulk mechanical property is measured before and after some applied damage and expressed as a % obtained from the following equation, where η is the self-healing efficiency, *χvirgin* is the initial value of the measured property and *χhealed* is the obtained value after the damage and healing process:

$$\eta\ (\%) = \frac{\chi_{healed}}{\chi_{virgin}} * 100$$

Equation 1.2. Self-healing efficiency equation expressed as %.

There are several analytical techniques to identify local molecular rearrangements that lead to the self-healing effects. Methods such as Infrared,[45] Raman[46] or dynamic nuclear polarization in NMR[47] techniques have been reported to be sensitive enough to successfully detect the *in-situ* self-healing process.

Moreover, the characterization methods most frequently performed in newly developed self-healing systems are property-testing techniques such as Dynamic Mechanical Assay (DMA), Static stress-strain tensile tests or lap shear tests, among others.

Nonetheless, within mechanical testing of self-healing systems, the quantification of fracture toughness has been the main reference value since the first studies. Tapered double cantilever beam (TDCB) specimens are used to rigorously study the fracture toughness recovery (Figure 1.13).

The main advantage of TDCB specimen over other types is that, thanks to the specific geometry, the generated crack length is independent from

the critical load and the fracture toughness, thus simplifying[48] the calculation of healing efficiency to the following equation:

$$\eta(\%) = \frac{K_{IC,healed}}{KIC_{virgin}} * 100 = \frac{P_{C\ healed}}{P_{C\ virgin}} * 100$$

Equation 1.3. Simplified self-healing efficiency (%) calculation for TDCB specimens.

Where P_C is the critical load and η is the healing efficiency.

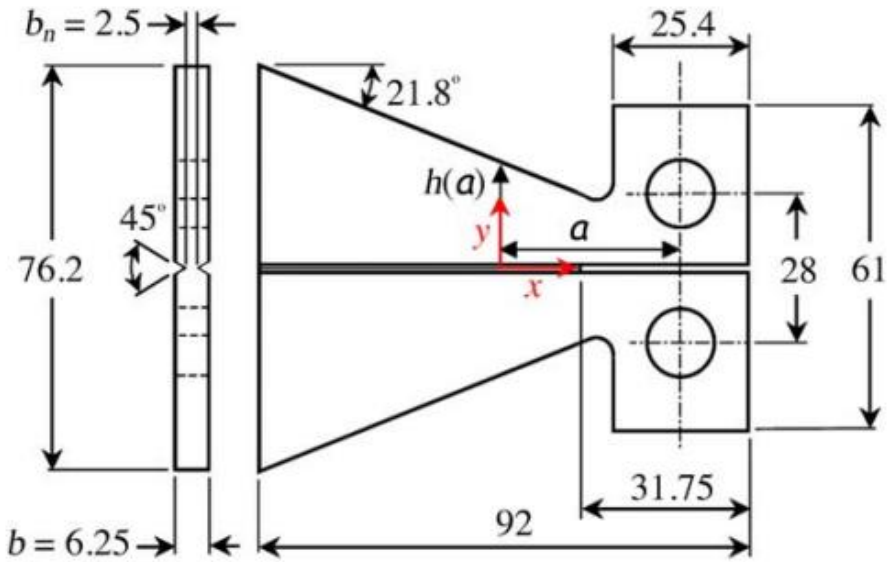

Figure 1.13. Scheme of the geometry of a Tapered Double Cantilever Beam (TDCB) specimen. All the values are expressed in mm. Figure from Brown et al.[62]

Other typical mechanical testing for the characterization of self-healing properties can be tensile,[49] impact[50] or bending tests.[38] All those testing methodologies use the same procedure as fracture toughness to study the self-healing capacity: the quantified recovery of a specific characteristic over a period of time. This studied characteristic varies depending on the applied test, as an example either the tensile strength, impact strength or the material's stiffness, respectively, can be used for the quantification of

the self-healing efficiency with each mentioned characterization techniques.

However, it should be noted that lately, some effort has been put into developing testing methodologies that could replicate more accurately the fatigue stresses that self-healing polymeric composites suffer through their lifetime. P.S. Tan *et al.*[51] proposed a methodology based on a damage mechanics theory which relies on in-plane shear stress followed by brittle damage of the matrix to simulate the non-linear response of the composite materials in the presence of damage and thus, predict the failure conditions. This is added to the material's potential to recovery and therefore, the real self-healing capability of the manufactured composite materials can be quantified.

Although it appears to successfully simulate closely real load stresses, the overall complexity within its methodology and calculation for the self-healing system is still preventing it from being the main procedure for self-healing testing.

Other techniques that can be used to assess the healing performance are based on observational processes such as scratch or deep cut recovery for self-healing coatings. Usually, those observations are produced with optical microscopy [52] or scanning proves such as AFM.[53]

1.3.1.4 Self-healing technology implementation and future perspectives

Nowadays, it can be stated that the self-healing technology is providing of an incredible versatile approach for obtaining new sustainable smart materials for the near future. However, there are still challenges to overcome before achieving a successful implementation of self-healing technology in polymers.

Pricing is still one of the main blocking factors in the implementation of self-healing technologies. In the current situation, one of the main questions to answer is "*How much more expensive can a self-healing polymer be to be worthy*?". There are a few niches, such as high technical application fields (aeronautic, aerospace, biomedical, construction, military…) where the need for improved smart materials is a must and the price sensitivity is more relaxed.

Therefore, most of current study areas are focused on these fields looking for a rapid transition to commercially availability. However, although the potential ease of implementation, those developments for such critical fields should target very specific requirements for both adapting to the manufacturing processes and for truly repairing a high-performance system.

Other perspectives that the self-healing technology need to address are the real-life applications and stability as well as the needs and properties in each specific case. For real-world applications, it is critical that further testing on the development of self-healing technologies is conducted in the environment that the materials will be exposed to during their operating lifetime. In addition, efforts should be placed into designing tests aimed at recognizing the behaviour of the material after its operating time.

Due to the high multidisciplinary of the self-healing technology, there have been plenty of novel developments applied to improve the chemical reactivity, the material's behaviour or the design of the initial self-healing polymeric chain. Additionally, the appearance of new tools such as IA or computational modelling can provide new insights to polymer

architectures or blends that can help in selecting the best combination of building blocks towards achieving a better performing system.[54]

Future lines of work within the development of novel self-healing systems could fall within the implementation of dual extrinsic-intrinsic mechanisms. It has been already explained that extrinsic self-healing systems hold the capability of repair large damages while intrinsic mechanisms can provide a theoretical limitless number of healing cycles. The incorporation of microcapsules containing intrinsic self-healing polymers with the aim of filling the produced cracks and covalently bond with the substrate, could potentially generate an ideal self-healing system.

1.3.2 Additive manufacturing technologies

Rapid prototyping and additive manufacturing (AM) are two synonyms for the more widely known term of 3D-printing. The overall technology concept is to design an object with a three-dimensional software (computer aided design/ computer aided manufacturing – CAD/CAM) with the capability of afterwards slicing the created design in the z-plane. Next, a layer-by-layer addition of material is deposited until it is completely manufactured. Although originated only 40 years ago, in a greater or lesser extent, 3D printing has produced an impact in all manufacturing-related businesses.

The first 3D printing technologies were patented during the 80's decade. More specifically, the first one was awarded in 1986 to Charles Hull for a stereolithography-based printer (SLA). Nonetheless, in 1987 and in 1992,

patents for selective laser sintering (SLS) and fused deposition modelling (FDM) were secured by what now are some of the big industrial players in the 3D printing world (DTM and Stratasys, respectively).[55]

As years passed, researchers and engineers found more and more applications for the recently discovered techniques, thus, new breakthroughs in the fields of medicine, aerospace, construction, or automobile industry were achieved. However, the economic barriers from the high costs of the printers and the lack of availability of materials for it, held the public adoption of the technologies.

The expiration of some of the existing patents allowed more companies to access the restricted data and provide of more affordable equipment as well as increased investment into the creation of new operating materials that could adapt into them.

Among plenty of initiatives for easing the incorporation of 3D-printing into our everyday lives, the RepRap project could be highlighted.

RepRap was a project lead by engineers from the British University and allowed worldwide users to share and download different software and designs completely free.[56] More importantly, it was directed to the creating of a self-replicating manufacturing machine through the premise of "a 3D printer, printing copies of themselves". It became so relevant that in 2017, most of the manufactured objects by 3D printers were processed through RepRap (Figure 1.14).[57]

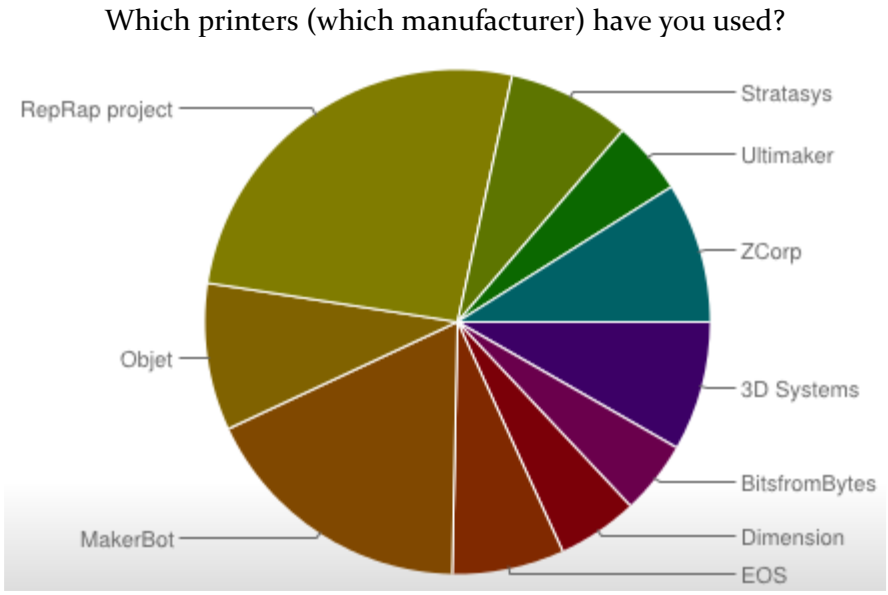

Figure 1.14. Results of a survey taken in 2013 to the 3D printing community for the most used printers and manufacturers.[56,57]

Overall, the genuine integration of 3D printing into our daily lives has occurred in the recent decade, when fields that require sophisticated or exceptionally specialized things can now produce the same objects with the same qualities using less complicated techniques and much more quickly. Perfect examples can be found in dental, implant or hearing aid companies where now most of its manufacturing processes are carried through 3D printing technologies.

1.3.2.1 Types of 3D printing

3D printing technology has advanced a lot since the early beginnings until employing a wide variety of techniques[58] mostly based on the physicochemical changes of materials to undergo from liquid to solid state. Due to business interests, some terms and abbreviations are directed towards describing the same process (for example, FDM is a

trademark for Stratasys but is the same as fused filament fabrication, or FFF, from RepRap project). Thus, to ease the classification of techniques, the American Society for Testing and Materials has developed a list of 7 different heading which comprehend all current 3D printing technologies:

a. Vat Photopolymerization (Vat)
b. Direct Energy Deposition (DED)
c. Material Jetting (MJ)
d. Sheet lamination (SL)
e. Powder Bed Fusion (PBF)
f. Binder Jetting (BJ)
g. Material Extrusion

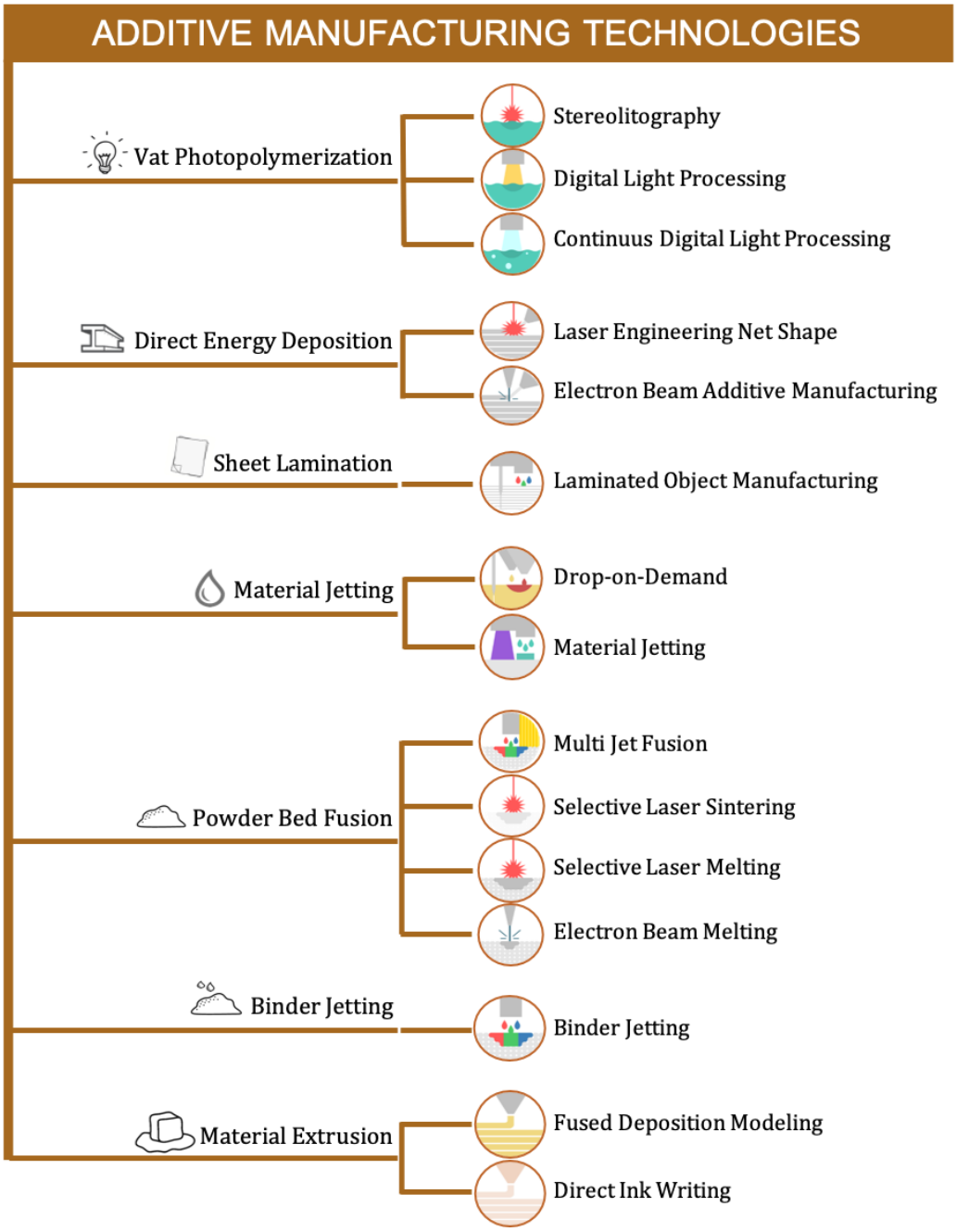

Figure 1.15. Infographic summary on AM technologies.

a) Vat photopolymerization

Although getting his name due to the use of a vat (synonym of tub or tray) of liquid polymer resin, the main characteristics of vat 3D printing is the use of a photon source (light, laser, or UV) as stimulus to generate solid, free-standing polymeric structures through chain-reaction polymerization. All vat 3D printing methods use resins containing monomer or oligomers as initial materials and molecules sensitive to light-based stimuli (UV absorbers, dyes, pigments…). Those embedded additives react upon contact with the energy source and interact with the neighbouring molecules, triggering the polymerization and creating the designed object. Noteworthy, the highly crosslinked network generated in the polymerization process carried in VAT printing leads to the generation of thermoset polymers, thus becoming irreversible. This means that the generated objects cannot be obtained in liquid form again.

As most 3D printing techniques, VAT photopolymerization needs a post-process that ensures a complete functional object. In these techniques, photocured pieces are immersed in an isopropyl alcohol bath to remove the object from any adhered residual monomer and afterwards, placed in an UV-curing oven to ensure a complete cured process.[59]

Two main different techniques fall under the umbrella of VAT polymerization. Those are stereolithography (SLA) and digital light processing (DLP).[59] The main difference between them is the used light source for the photopolymerization and manufacture of the desired object. In SLA, a focused UV light traces the shape of each cross section of the generated layer attaching it to a platform (the first layer, Figure 1.16).

Then, the platform moves in the z axis, leaving space for the photocuring of the next layer of material that will adhere to the previous one. Although normally the object is created upside-down, there are now 3D printers capable of printing it bottom-up. The final resolution of an SLA printer is proportional to the diameter of the laser beam, called also spot size. DLP 3D printing differs from SLA by using both a more conventional light source and a projector (Figure 1.17).[59,60]

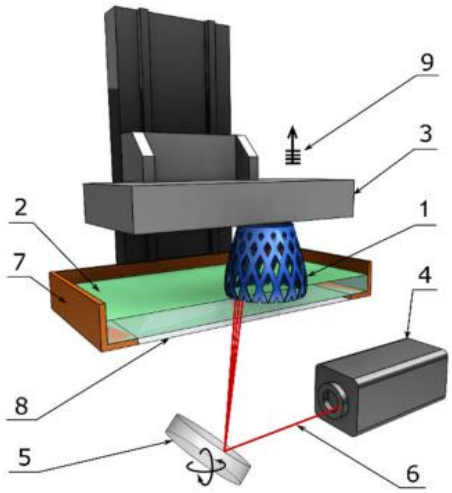

Figure 1.16. Structure and components of an SLA printer. 1- printed object, 2-photosensitive resin, 3- building platform, 4- Laser source, 5- XY scanning mirror, 6- laser beam, 7- resin vat, 8- transparent window, and 9- layer-by-layer movement. Obtained from Pagac et al. [69]

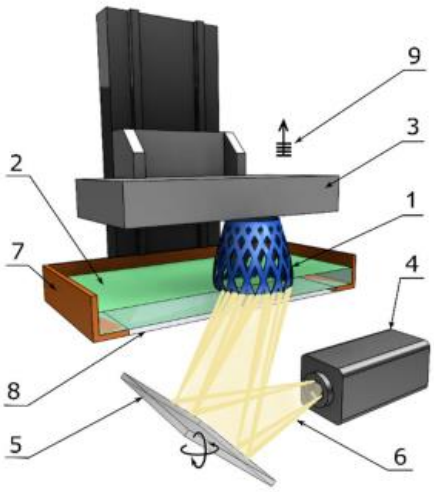

Figure 1.17. Structure and components of a DLP 3D printer. The only difference between DLP and SLA is in 4-the light source, 5-a digital projector and 6-the used light beam.

The liquid crystal display panel transfers the light source to the overall resin surface in one step, thus greatly increasing the printing speed compared to SLA. Due to the lack of pixels when using SLA, higher resolutions are obtained compared with objects printed with typical DLP. On the other hand, higher printing speeds are achieved with DLP in comparison with SLA.

A variant of the DLP is the continuous DLP (CDLP) also named as continuous liquid interface production (CLIP). The three main modifications are that the used projector is LED-based, that the transparent window is oxygen-permeable and the layer's manufacturing. Oxygen is a scavenger of the radical photopolymerization reaction, thus, its presence in the resin partially inhibits the conversion from liquid to solid state. This effect that normally would be considered as a drawback, creates a flow of uncured resin that provides a more accurate resolution of the printed structure and avoids the presence of potential peel forces with the transparent window (Figure 1.18). In cDLP, compared with DLP, the layer-by-layer structure is created continuously, this improving greatly the printing speed and the coherency between z-stacked layers.[61]

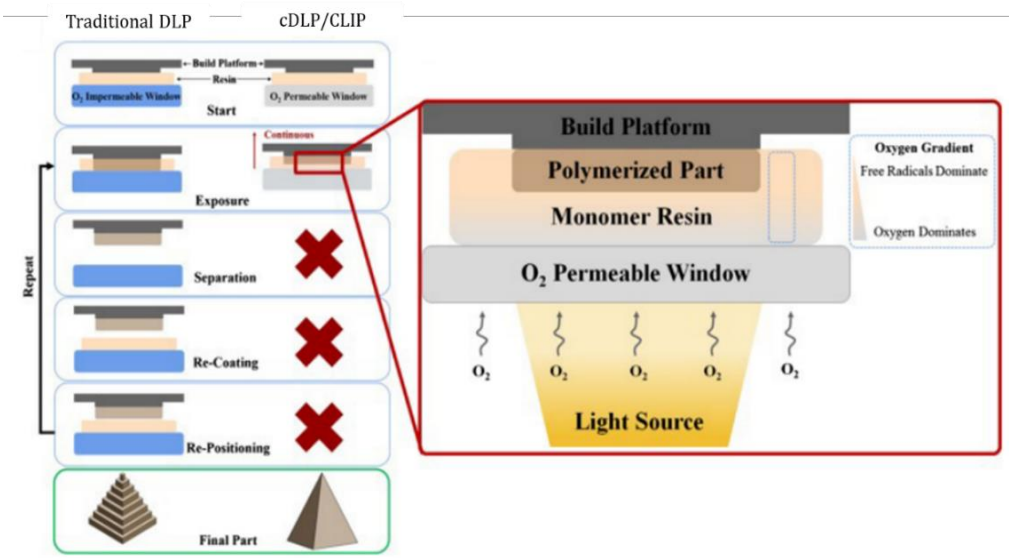

Figure 1.18. Comparison between traditional DLP and cDLP. Moreover, the effect of oxygen in the photopolymerization/printing process is highlighted. Obtained from Düzgün et al. [72]

Recently, some researchers have started to create 3D micro or nanoscopic objects through photopolymerization beyond the diffraction limit using a technique called two-photon absorption[62] or two-photon lithography

(2PL). Due to the required optical complexity, it is a much more expensive technique but has found its niche in medical applications.

b) Direct Energy Deposition (DED)

As DED 3D printing is focused on the creation of metal objects only a brief description of the technique will be provided here.[63]

DED is based on the application of a beam from a highly energetic source (electron or laser beam) that is able to both melt and deposit a metal source provided by either a metal wire or from powder. The main advantage of DED against other techniques that use metals as printing materials is the speed provided by the simultaneous deposition and fusion effect and by the multi-axial arm that can deposit the material in any direction, thus proceeding with the object manufacturing at any direction at will. Either thermal or surface machining can be used as post-process to obtain the required finished product.

c) Material Jetting (MJ)

Through the finely controlled firing droplets of reactive substances that will be afterwards cured by either radiation (heat or light) or an additional chemical crosslinker, it is possible to generate a layered manufacturing process. Drop-on-demand (DoD) is a synonym for discrete MJ 3D printing processes. However, material jetting can be also performed as a continuous manufacturing technique. Advantages of MJ are its accuracy, the generation of thin layers (down to 16 μm) or the possibility of using several printing heads to generate the desired patterns more rapidly and using different polymers, thus creating a multi-material structure at once.

The droplet generation and firing can be produced by two main effects, thermal or piezoelectric. In thermal-based inkjet printer, a heating resistance induces a small vapor bubble in the used ink, creating a pressure force that propels the droplet out of the nozzle. As drawback, this type of printheads usually have less durability and additionally, have a poor variety of materials due to the need for them to be thermally resistant.

Piezoelectric actuators use the piezoelectric effect (the generation of a conformational mechanical change when an electric field is applied) to fire the droplet outside the material. The firing in piezoelectric systems can be generated from an acoustic wave from the sudden change of conformation or by physical impulses of the piezoelectric membrane.

Several parameters such as the applied voltage and amplitude, the jetting frequency, the firing speed (and applied pressure) or the surface tension of the used ink can impact in the final resolution and quality of the manufacturing process, for example, by creating satellites or clogging the nozzle (Figure 1.19).[64]

Due to the rather inconsistent mechanical properties of the printed structures during the process, a support structure is needed. The preferred option for material jetting printing is the use of dual systems where the desired material is ejected from one nozzle and the support material form the second. The support structures usually use the same curing method as the selected constructing material but can be removed by different methods such as sonication, chemical baths, by melting (if wax is used as supporting material) or pressurized water.[65]

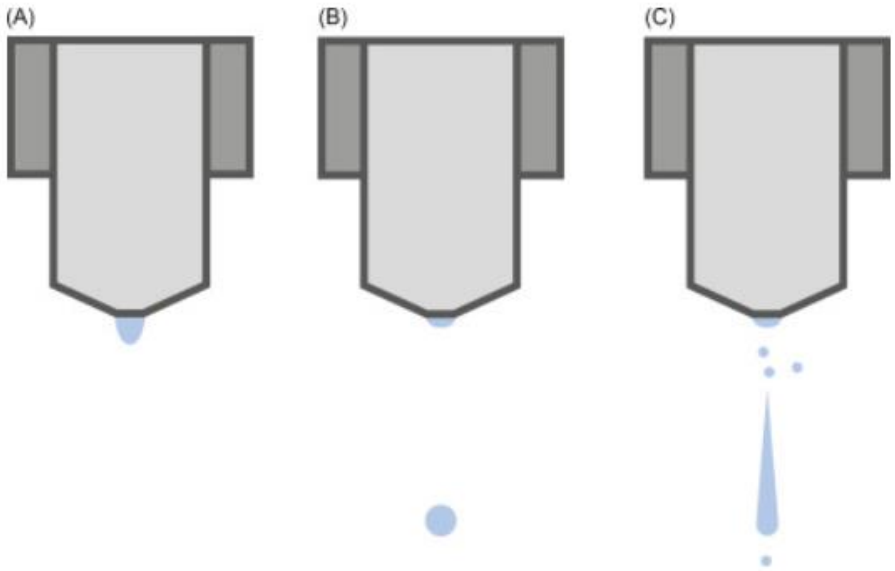

Figure 1.19. Droplet formation in DoD 3D-printing. In (A) is represented what would be seen if no-jetting happened. (B) is the representation of an ideal jetting and in (C) the generation of satellite drops can be observed.[64]

d) Sheet lamination (SL)

SL 3D printing technique uses conventional A4 paper sheets as printing material. To obtain adherence between sheet papers (and layers) an adhesive coating is applied to each side of it. Then, a blade is used to cut each cross-section of the CAD-CAM generated layer, cross-hatching the excess material and, after stacking all the necessary sheets, manufacturing the object. It benefits from the wide use of colours and different types of existing papers to create any kind of structure. As drawback, this process generates a lot of non-reusable waste material.

As a post-process, the paper object can be coated with some resin to provide of more mechanical integrity and improve its final aesthetics.

e) Powder Bed Fusion (PBF)

PBF 3D printing consists of fusing (sintering or melting) beads of powder material by using different energy sources. For manufacturing the desired object, a platform located inside the modelling chamber is filled with the appropriate amount of powdered material. Afterwards, an energy source that, depending on the specific technique can be heat, light or electrons is applied following the patron of the layer and creating a solid layer from the beads. Once the first layer is created, the platform is lowered, and a second layer of fresh material is spread over the first layer. It is necessary to maintain a temperature below the glass transition temperature or melting point of the used material inside the manufacturing chamber to assure a solid behaviour of the beads previously to being irradiated. While using polymeric beads (such as polyamide, polyurethane…) there is no need for the creation of supporting structures, as the rest of non-sintered beads act as them.

There are 4 different techniques using the principle of PBF: multi jet fusion (MJF), selective laser sintering (SLS), selective laser melting (SLM) and electron beam melting (EBM).

MJF is a 3D printing technique created by Hewlett-Packard (HP). It uses the same basic principle as most 3D printing as it creates a software design of the object and z-slices are generated, allowing to print the material layer-by-layer. Although more materials are in their development pipeline, it mostly uses polyamide 12. First, a fusing agent and a detailing, limiting agent are jetted over the beads to create the wanted structure. Then, a heating lamp moves through the surface, melting the jetted material and afterwards, another layer of beads is applied (0.08 mm) and the process is repeated until the object is manufactured. By optimizing the volume of the printing chamber, it is

possible to obtain truly industrial productive speeds using this technique.[66]

SLS is directed also to the creation of thermoplastic-based objects and uses a laser beam to do so. SLS can provide robust and well-defined objects with complex geometries using low costs but does not have a high manufacturing speed. For this reason, it is already used regularly in fields with low-volume production such as medical, automobile, or aeronautic.

Both SLM and EBM use metal as base materials to produce the designed structures. Instead of sintering the beads as produced in SLS, in these techniques the material is melted and fused together. As metals require more energy to move from solid to liquid state, the applied energy sources are more energetic than the used in SLS. Nonetheless, SLM and EBM provide a real powerful tool for creating personalized metal parts where otherwise could be necessary the use of multiple pieces. The use of electrons instead of photons (EBM vs SLM) increase greatly the resolution of the technique and the price required for it.

Most post processes for PBF require removing of non-adhered beads to the created surfaces by applying pressurized air or annealing the remaining material through the application of temperature.

f) Binder Jetting (BJ)

3D-printing manufactured structures using Binder Jetting are very similar to those done with PBF. Contrary to PBF, in BJ a liquid binder is used as an external additive that is afterwards cured and attaches the material in the shape of beads.

BJ can be applied to a whole range of materials such as polymers or ceramics and, similarly to SLS or MJF, the manufactured designs do not

require any supporting structures as the surrounding powder acts as one. Thanks to the application of different dyes, it is possible in BJ to generate coloured structures without post-processing methods. Nonetheless, aiming to reinforce the printed object, infiltration of different kinds of resins is advised.

g) Material Extrusion

Material extrusion 3D-printing is also referred as FFF or FDM and it is one of the widest and most affordable type of commercial 3D printer techniques. The overall mechanism works by extruding a semisolid or solid material through a nozzle and stacking layers one above the others in a build plate.

The physical force that drives the extrusion of the material outside the printer can be generated by either a pneumatic, a piston or a screw-based system.

In typical material extrusion printers, rollers or pistons control the feed rate of the material to the different type of nozzles. Afterwards, by using heat, the thermoplastic polymer is melted and deposited in the x-y plane it while cooling the material gradually back to solid state. It is important that the cooling process is controlled due to potential warping effects in the polymer that can damage or even collapse the manufactured structure. Once the layer is generated, the platform moves into the z plane and the printing process continues until the completion of the designed object. For very complex geometries, extrusion 3D printing provides the possibility to generate supporting structures of a different material but requires a dual extruder. The material forming those structures can be easily removed once extrusion has finished. For faster printing speeds and more efficiency, the second material can be

incorporated into the process by adding a second extruding nozzle and printing in parallel with the main one.

Direct Ink Writing (DIW) is a fabrication method that uses a semi-solid and ceramic-based ink as material and deposits it continuously in defined paths to create the 3D structure prior to solidify it. Although it is mostly classified within the material extrusion processes, droplet-based approaches such as inkjet printing can be considered also as DIW techniques.[67]

From the perspective of enabling the incorporation of new materials, DIW is the most versatile 3D-printing technique, as the main requirements are a controlled rheological behaviour and a defined curing method. This ease for including new materials makes DIW as one of the most promising 3D-printing technologies for scaling-up to industrial scale, develop materials impossible to test in other technologies (such as soft structures) as well as creating the first true multi-material 3D-printed objects thanks to the incorporation of microfluidic devices in the printheads.[68]

1.3.2.2 Advanced polymeric materials for 3D printing and current challenges

One of the main limiting factors that prevent the full adoption of 3D printing into more fields appears to be the lack of usable materials that fit into specifically targeted applications.[58] Separating polymer-based materials from the rest (ceramic or metallic), 3D-printing technologies have been mostly limited by the use of PLA and polybutadiene-styrene (PBS) for material extrusion technologies, Nylon and polyamide (PA) for Binder Jetting and Powder Bed Fusion and some acrylic-based photocurable resins for vat photopolymerization. As the obtained final

properties of those materials can be relatively similar, the range of implementation is way smaller than the true potential of the technology. This issue has already been identified by researchers and different works are in development towards solving it.

The discussion of advances in the development of polymer materials for 3D-printing systems can be separated in novel, general materials and in advanced, smart materials. Briefly, while general materials are aimed towards broadening the number of potential materials that can be adapted for AM, smart materials are those "programmed" to respond to external stimuli.

The trends regarding development of general materials with improved properties are as broad as the final application purposes. However, due to the additional complexities of generating a single material that can provide for a range of diverse functionalities, most works for novel polymer-based materials for 3D-printing are focused on the creation of either composite or multi-materials.[69] For example, up to now in photopolymerization-based AM techniques,[70] acrylate-based monomers and oligomers were the most common resin compositions.

To provide materials capable of sustaining much higher temperatures than the achieved up to this date, some new photopolymerizable inks have been modified to contain ceramic precursors that, after the printing process, can be further processed until generating a ceramic-polymeric hybrid.[71,72]

Other strategies for the creation of novel materials involve the incorporation of additives to conventionally used precursors to increase their mechanical properties while maintaining their low density or wide availability. For example, studies of the incorporation of TiO_2 in ABS for

material extrusion AM allowed to greatly increase the ultimate tensile strength of the composite versus the neat material or other blends.[73] On other works, the in-situ generation of PLA-Carbon fiber composites by EM has already been explored by several authors to create lightweight structures for aerospace applications.[74]

On the other hand, there is an increasing need for successfully printing soft materials for biological or soft-robotic applications, among others. Recent studies such as those from D.K. Patel *et al.*, which synthesized a highly stretchable elastomer derived from ABS for photopolymerization AM,[75] K. Du, *et al.*, that created a PDMS-based elastic material[76] or J. Odent *et al.*, which used an ionic composite hydrogel for ME applications, advanced the frontiers of soft polymers in 3D-printing manufacturing.[77] Moreover, the recent generation of soft composites or multimaterials capable to obtain structural and functional improvements are thoroughly discussed in recently published reviews.[69]

Although the recent efforts in the development of soft polymeric materials, there is still an urgent demand for soft materials capable of being adapted for each necessity at will. The hardness adaptability of those polymers could provide researchers of a novel tool to innovate in fields (mainly health and biomedical applications) where has not been easy until now.

As a concluding remark, due to the drastic advance of the digital design and AM technologies, 3D printable materials with tailored properties are nowadays considered to be the limiting factor of an upcoming potential productive revolution.

1.3.2.3 Transition to 3D Bioprinting

The application of 3D-printing technologies to the layer-by-layer manufacturing of complex 3D functional living tissues is called 3D bioprinting. The combination of the inclusion and the controlled deposition of biocompatible materials, while supporting biochemical components or living cells into the systems, has added a new degree of complexity to an already challenging field. Thus, 3D bioprinting is an incredible translational area where physicists, engineers, biochemists, medical doctors or biologists need to work together to fill out each part of an intricate puzzle thus creating functional and physiologically relevant structures.

Similarly to what occurs in 3D printing, several approaches and techniques are integrated in what has been developed as 3D bioprinting. The main used methodologies are biomimicry, autonomous self-assembly, and mini-tissue building blocks while Inkjet bioprinting, microextrusion bioprinting, and laser-assisted bioprinting (LAB) are the leading current used printing technologies.

Biologically inspired engineering is defined as biomimicry. Biomimicry is based into looking how the natural organisms have used millions of years of evolution and adaptation to solve similar problems that researchers are facing now. In 3D bioprinting, biomimicry is focused on replicating those exact same biologically relevant structures that are seen in the nature as exemplified in Figure 1.20 (e.g. replicating gradients of textures and stiffness). However, in order to fully replicate what is seen inside biological systems, it is imperative to first have a deep and extensive knowledge about the composition, self-regulating forces and functionality of each component.

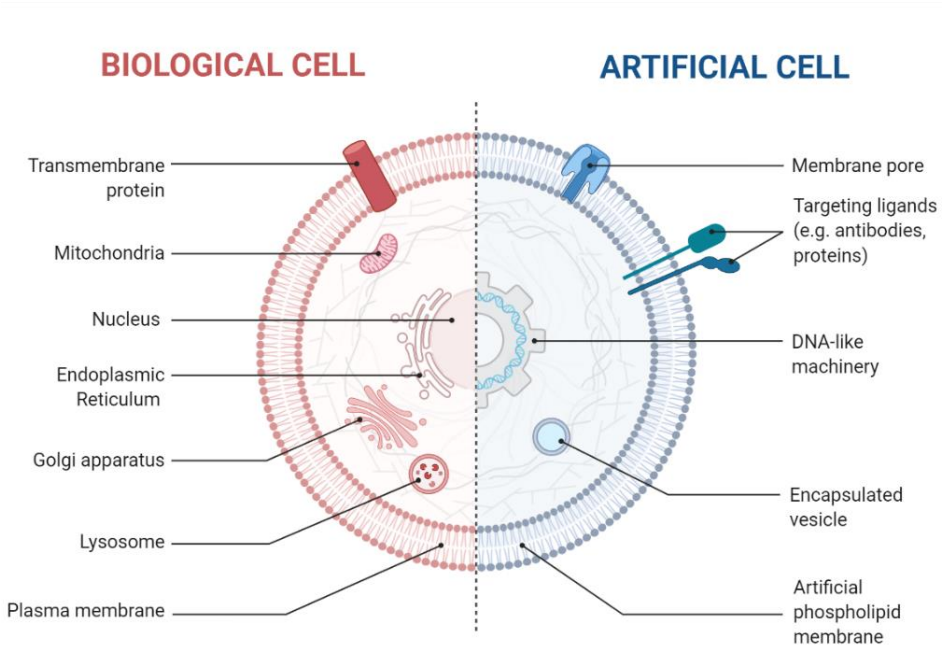

Figure 1.20. Representative Biomimicry approach to generate an artificial cell.

Autonomous self-assembly relies on the signals generated by the incorporated cells into the printed structure to drive all the following steps of organization and histogenesis, replicating thus the same behaviour as seen in the early embryonic stages of the organ development (Figure 1.21).[78]

Nonetheless, some previous manipulative signals must be implemented in the printed materials to tune the response towards the intended final purpose (e.g. short adhesion peptides or growth factors).

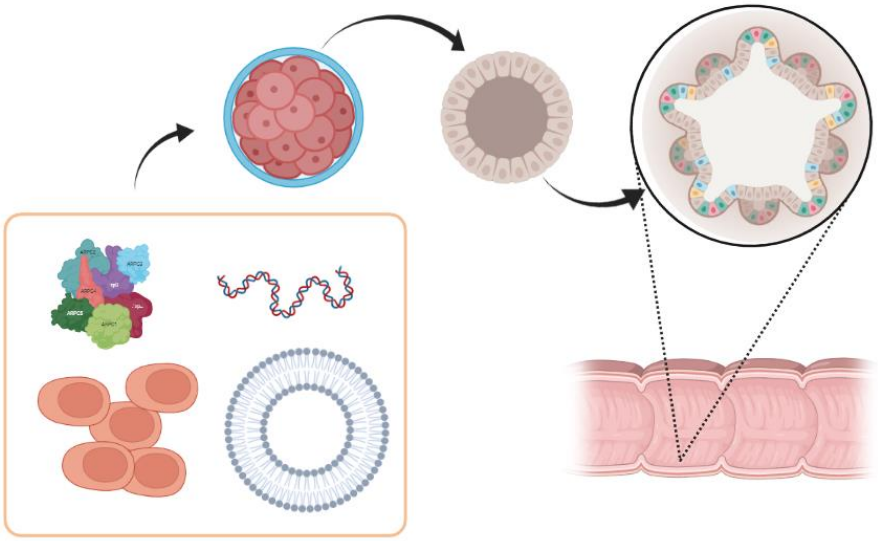

Figure 1.21. Self-assembly procedure scheme. By the inclusion and autonomous behaviour of cellular and extra-cellular components, more differentiated structures are self-generated.

The concept behind the approach of using mini-tissues uses similar precepts as the mentioned above with the difference of having a miniaturized fully functional tissue as the stablished smaller functional component (Figure 1.22).

In this approach, there is first the step of generating a series of small-sized structures capable of performing almost the same functions as the major organ they are looking to replicate and afterwards, those will be assembled (or self-assembled) into a major, more physiologically representative macro-systems.

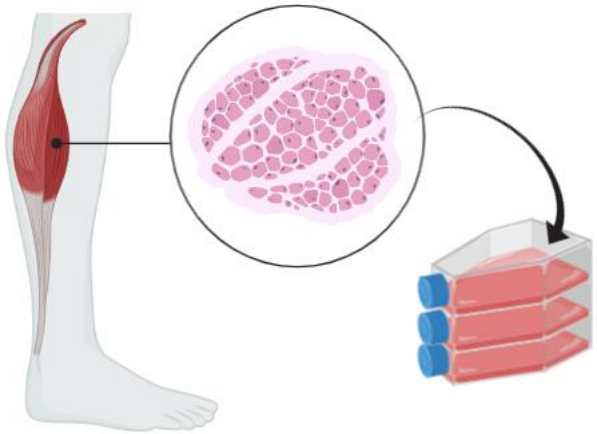

Figure 1.22. Graphical representation of a Mini-tissue.

1.3.2.4 Printing strategies

Inkjet bioprinter, known also as Drop-on-demand printers works by shooting small droplets of liquid biomaterial into a targeted location while maintaining a high resolution and speed (Figure 1.23.1). Inkjet actuators, as previously mentioned (MJ), can use different types of impulses to create and eject drops of the selected (bio)material. Heat-based inkjet works by electrically heating the print-head, partially expanding (evaporating) the bioink and thus, producing a pressure pulse. Although the printhead can reach temperatures above 200 °C, there has been plenty of studies demonstrating that only a 4 to 10 °C heating increase is generated in the printed drop and thus, no significant harm to either cells or genetic material is produced.[79,80] Even considering all these studies, there is always some potential risks when exposing cells to high temperatures or strong mechanical stresses. Acoustic actuators apply their forces through the generation of acoustic waves by using piezoelectric crystals or ultrasound fields. By modifying the pulse's duration and amplitude it is possible to finely tune the droplet size or the

rate of ejection as well as to obtain an improved control of the printed directionality.

As all technologies, there are some drawbacks that need to be taken into account when using those systems. The main ones are the necessary use of low viscosity liquids and the potential limitation for high cell densities. The first one implies that some crosslinking mechanisms must take place after the printing process, thus limiting its speed or making the overall process more complex (addition of UV light, modification of natural extra cellular matrix (ECM) components…). Having high cellular densities in the inks may prevent the generation of homogeneous drops or cause nozzle clogging when the printing starts. Therefore, the cell count in bioinks for inkjet bioprinting needs to be tested for each application before starting with the manufacturing process.

Among the different existent bioprinting techniques (inkjet, micro-extrusion or laser assisted biopring), micro-extrusion bioprinting is the most affordable and commonly used of them all (Figure 1.23).

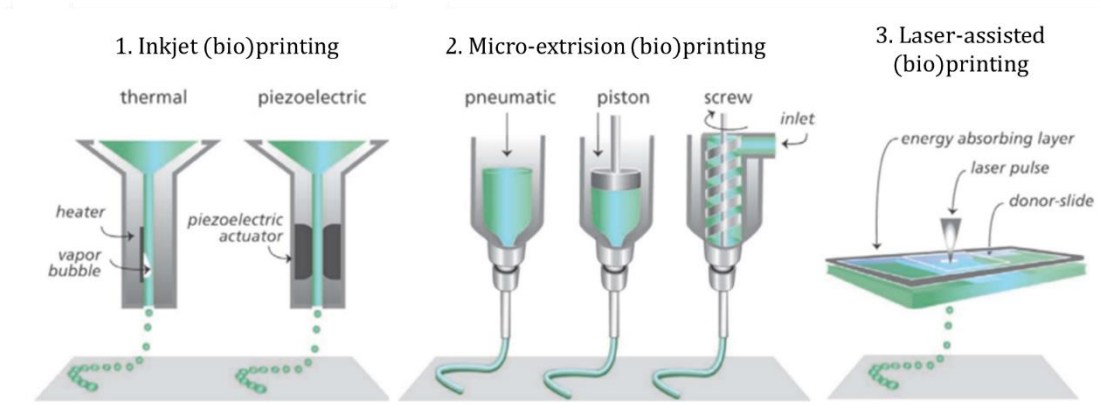

Figure 1.23. Representative figures on the printing mechanisms for the most-used 3D-bioprinting techniques. The overall mechanism is the same for "normal" 3D-printing systems except for the use of biologically-based or cellularized inks. 1. Inkjet (bio)printing with a heat (left) and piezoelectric (right) actuators for the droplet generation. 2. Physical forces applied to extrude the ink for ME (bio)printing, pneumatic (left), piston (center) and screw (right). 3.Overview of the sandwich panel in LAB.

Replicating extrusion mechanisms for "normal" 3D printing, a bioink is controllably deposited onto a substrate through a micro-extrusion head following a pre-settled path directed by a CAD-CAM software and manufacturing the desired structure layer-by-layer. The main dispensing systems currently used for micro-extrusion methods are pneumatic and mechanic (piston or screw, Figure 1.23.2). One of the main benefits of using micro-extrusion bioprinting is the wide availability of materials that can be used, especially those presenting high viscous behaviour. This capability also means that printing biomaterials containing high density of cells is possible, which allowed researchers to create multicellular spheroids with complex structures and biological relevance.[81]

On the other hand, the cell viability exhibited after micro-extrusion processes is between 40 to 86%, with higher cell mortality proportional to the used dispensing pressure and the afterwards generated shear stresses. To prevent cell death while maintaining good resolution and speed, there are improvements towards new nozzles, motor systems o the application of multi-deposition syringes in process which could reduce printing times and allow for the printing of multiple materials simultaneously.[82]

Using the same principles developed to transfer metals in AM, LAB uses a focused pulsed laser beam directed to an absorbing layer that creates a bubble and propels the biomaterial towards a substrate in a very precise manner (Figure 1.23.3). One main difference of LAB comparing with the other bioprinting techniques is the absence of nozzle. Problems related to clogging or viscosity limits from the inks or high cell densities are therefore avoided. Nonetheless, LAB technique requires a lot of time to prepare the system for the co-printing of different materials or cell types due to the careful preparation of the absorbing layer (ribbon). Even

though it is still a rather expensive technique for rutinary 3D bioprinting, due to the potential in-situ generation of clinically relevant tissues, it can found a niche in in-situ regenerative surgery.[83]

1.3.2.5 Synthetic polymeric materials used in 3D bioprinting, applications and current challenges

In contrast to conventional 3D printing, several properties (such as biocompatibility or printability around the corporal temperature) must be fulfilled by the printed material to be considered a bioink. All those compromises, taken to ensure an optimal printability and biological stability of the system, fall under the biofabrication window concept.[84] Although sometimes the nomenclature for bioink include both the cellular component and the material, in this section the term "*bioink*" will be used as reference for only the material used in 3D bioprinting.[85]

The selection of the optimal components for 3D bioprinting applications is one of the main pillars for achieving a final representative and functional synthetic tissues.[86]

Polymers obtained from natural sources and applied in the biomedical field are defined as natural biomaterials. Their capability of mimicking the cellular environment, self-assembly capabilities, excellent biocompatibility or biodegradability, make them versatile and useful for 3D bioprinting studies. However, those materials usually suffer from different drawbacks such as lack of reproducibility, poor mechanical stability or no tuneability, that ultimately prevent their inclusion and implementation into industrial processes.[87] Although synthetic polymeric materials lack of bioactive markers and some can exhibit low cytocompatibility, they can be tuned at will, present outstanding mechanical properties and prevent the lack of uniformity observed in

their natural counterparts.[88] In order to support cell survival and further biointegration, most natural and synthetic materials are generated in the shape of hydrogel structures.[85,89]

Within the use of synthetic polymers, more than 10 different types have been reported to be applied in 3D bioprinting studies.[90] In short, PLA, with its derivatives as polylactic-co-glycolic acid (PLGA), polyethylene glycol (PEG), polyether ether ketone (PEEK), polycaprolactone (PCL) or PU are the most widely used. Among these polymers, PEG and PU can be highlighted.

PEG is hydrophilic, present cellular and protein repellence and it's an extremely biocompatible polymer. For all those reasons, it has been widely used also for vehicle in drug delivery systems, soft tissue engineering or surface modification. The main current drawbacks of pure PEG polymers are their poor mechanical properties[91] and non-degradability, thus, the incorporation of PEG into copolymer systems such as Pluronic (copolymer PEG-[polypropylene glycol]-PEG) or its use as chemically modified structure to allow different printing strategies (e.g. with (meth)acrylates for photopolymerization) are the main used approaches in PEG-based materials applied in the 3D bioprinting field.

PU, with an outstanding capability of enduring repetitive contraction stresses, has found its niche as material used in 3D-bioprinting for the creation of artificial muscles, nerves or cartilages. Most of the PU manufacturing processes for biological applications were limited by the use of organic solvents, non-compatible polyols or traces of free-isocyanate molecules after the synthesis processes. Nonetheless, thanks to using non-toxic waterborne PU and the inclusion of biocompatible or biodegradable polyols such as PEG or PCL have allowed PU to become a commodity polymer in 3D bioprinting. Moreover, as in conventional AM,

it is possible to introduce other chemical groups to allow different post-polymerization pathways to widen the field of applicability in other 3D-bioprinting technologies.[92]

As one of the main drawbacks of synthetic polymers is their lack of bioactivity, several modifications have been applied aiming to obtain different biological responses that those produced by their native structures.

The potential functionalization of the polymer chains include the use of cell-binding peptides such as arginyl-glycyl-aspartic acid (RGD),[93] drugs, genes, proteins, amino acids and more.[94,95] Those modifications have proven to widely increase cell compatibility with different non-natural materials and tune the overall cellular response.

1.3.2.6 Current applications of 3D bioprinting

Even though the ideal target for 3D bioprinting is the complete artificial substitution of tailored tissues and organs for each individual patient (personalized regenerative medicine), the development and current applications of 3D bioprinting can provide a wider range of capabilities.

Due to the high availability of hard synthetic biomaterials, tissue engineering of hard organs focused on bone and cartilage has been one of the primaries and more successful aims of development.[96] Coming from a wide variety of simple 3D-bioprinted models, different authors have created more and more complex systems which are becoming synthetic replicates of bone tissue with variable porosity and their own vasculature.

Thanks to the layered structure of the skin, it is now possible to create stratified structures with different composition that try to replicate the

most complex organ of the body. Moreover, studies about in-situ skin bioprinting are being held for clinical trials.[97]

3D bioprinting studies pursuing the regeneration or replacement of softer organs such as liver, lungs, heart or neural have also been reported in the last years. As the number and types of bioinks increase, the possibilities to obtain more representative tissues are increased.[98]

One of the most interesting current applications of 3D bioprinting technology is the generation of high-throughput 3D tissue models for research purposes such as drug discovery, cell behaviour, cancer studies or toxicology profiling.[99] New drug development usually takes about 10 years, almost a billion dollars and only 1 out of 10.000 initial compounds are usually successful.[100] One of the main bottlenecks is passing from in-vitro to in-vivo testing. Among the leading reasons for this repeatedly reported phenomenon, is related to the lack of clinical relevance of typical 2D in-vitro systems.

Nowadays, multidisciplinary teams are joining to create 3D models through different approaches that are capable of representing more accurately real biological environments.

Although the 3D model is slightly more expensive than the current 2D, the obtained information is much more relevant and thus, the overall economic impact is positive on the drug validation process.[101] A similar prospect is used for studying of different diseases such as cancer. By generating relevant 3D models able to better replicate the overall environment, it is possible to study and test different combinations of drugs or molecular pathways and easily translate it to clinical applications.[102]

1.3.2.7 Future perspectives of 3D bioprinting:

Several problems are blocking the already game-changing 3D bioprinting technology from moving to the next stage and become a suitable substitute for organ and tissue replacement. As per today, some steps of the bioprinting process are still performed manually, leading to potential errors and an overall slowness of the model/piece generation. Moreover, for obtaining objects capable of being implanted there is still a lack of enough in-vivo vascularization of the manufactured tissue. Improvements in materials that can allow a better diffusion through the material[103,104] or the generation of artificial vascular systems[105] are already on their way to solve this recurrent issue. Also, due to extreme complexity and heterogeneity of biological organs, improvements in the printing resolution and methods are needed.

However, the factor which withholds the most potential for improving 3D bioprinting technology is the manufacture of novel bioprinting materials (bioinks). The generation of those enhanced materials can be either by the discovery of polymers capable of mimicking more accurately the extracellular environment (improved nutrient diffusion, electrical conductivity, mechanical adaptability) or by the combination of current existing polymers with the right biological markers. Also, it should be taken into consideration the potential of in-situ in-vivo 3D bioprinting to allow a partial substitution or specific support of damaged structures in what would be one of the most advanced approaches of personalized medicine.

In parallel, the manufacture of more relevant 3D cell models can become crucial in the development of platforms capable of enhancing drug discovery or influencing in the discovery of cellular/molecular pathways. To that end, improvements in the material composition and behaviour

are needed to get closer to mimic real cellular environments. An interesting focus of study for the next generation of cellular models could be set into the synthesis of materials capable of reproducing aging or other matrix rearrangements due to the cellular behaviour.

Nonetheless, as a middle ground between the optimal generation of artificial organs and 3D printed models, scientists are now developing surgical models for surgery training. Those models are generated by using acquired images from a patient and afterwards, selecting specific materials with matching mechanical properties with the targeted organ, thus generating a model with the exact inner structure and relevant mechanical behaviour. However, there is still work to obtain materials capable of being 3D printed and hold the overall properties to allow the manufacture of a clinically relevant organ surrogate. Only then, doctors and surgeons will possess a powerful tool to better organize the surgery and minimize any potential risk from unexpected complications.[106]

1.4 References

1. Babooram, K. Brief overview of polymer science. in Polymer Science and Nanotechnology 3–12 (Elsevier, 2020). doi:10.1016/B978-0-12-816806-6.00001-7.
2. Nuyken, O. & Pask, S. Ring-Opening Polymerization—An Introductory Review. Polymers 5, 361–403 (2013).
3. Macchione, M. A., Aristizabal Bedoya, D., Figueroa, F. N. & Strumia, M. C. Synthetic and semi-synthetic polymers for pharmaceutical applications. in Advances and Challenges in Pharmaceutical Technology 45–73 (Elsevier, 2021). doi:10.1016/B978-0-12-820043-8.00005-0.
4. Duda, A. & Kowalski, A. Thermodynamics and Kinetics of Ring-Opening Polymerization. in Handbook of Ring-Opening Polymerization (eds. Dubois, P., Coulembier, O. & Raquez, J.-M.) 1–51 (Wiley-VCH Verlag GmbH & Co. KGaA, 2009). doi:10.1002/9783527628407.ch1.
5. Handbook of metathesis. (Wiley-VCH, 2003).
6. Leitgeb, A., Wappel, J. & Slugovc, C. The ROMP toolbox upgraded. Polymer 51, 2927–2946 (2010).
7. Hu, S., Zhao, J., Zhang, G. & Schlaad, H. Macromolecular architectures through organocatalysis. Progress in Polymer Science 74, 34–77 (2017).
8. Callister, W. D., Rethwisch, D. G., Molera, P., Sal??n Ballesteros, M. N. & Callister, W. D. Ciencia e ingenier??a de los materiales. (2018).

9. T. C. Harris. A Theoretical Model for the Self-Assembly of Amphiphilic Polyrotaxanes into Structured Aggregates. (2017) doi:10.13140/RG.2.2.22058.88003.
10. Young, R. J. & Lovell, P. A. Introduction to polymers. (CRC Press, 2011).
11. McKeen, L. W. Introduction to Plastics and Elastomers. in Effect of Temperature and other Factors on Plastics and Elastomers 1–39 (Elsevier, 2008). doi:10.1016/B978-081551568-5.50003-7.
12. Li, M., Bijleveld, J. & Dingemans, T. J. Synthesis and properties of semi-crystalline poly(decamethylene terephthalamide) thermosets from reactive side-group copolyamides. European Polymer Journal 98, 273–284 (2018).
13. Szycher, M. Szycher's handbook of polyurethanes. (CRC Press, 1999).
14. Bayer, O. Das Di-Isocyanat-Polyadditionsverfahren (Polyurethane). Angew. Chem. 59, 257–272 (1947).
15. Ratner, B. D. Biomaterials science an introduction to materials in medicine. (2013).
16. Alagi, P., Choi, Y. J. & Hong, S. C. Preparation of vegetable oil-based polyols with controlled hydroxyl functionalities for thermoplastic polyurethane. European Polymer Journal 78, 46–60 (2016).
17. Rahmawati, R. et al. Microphase-separated structure and mechanical properties of cycloaliphatic diisocyanate-based thiourethane elastomers. Polym J 51, 265–273 (2019).
18. Honarkar, H. Waterborne polyurethanes: A review. Journal of Dispersion Science and Technology 39, 507–516 (2018).

19. Stachak, P., Łukaszewska, I., Hebda, E. & Pielichowski, K. Recent Advances in Fabrication of Non-Isocyanate Polyurethane-Based Composite Materials. Materials 14, 3497 (2021).
20. Kathalewar, M. S., Joshi, P. B., Sabnis, A. S. & Malshe, V. C. Non-isocyanate polyurethanes: from chemistry to applications. RSC Adv. 3, 4110 (2013).
21. Joshi-Barr, S., de Gracia Lux, C., Mahmoud, E. & Almutairi, A. Exploiting Oxidative Microenvironments in the Body as Triggers for Drug Delivery Systems. Antioxidants & Redox Signaling 21, 730–754 (2014).
22. Deng, Z. & Liu, S. Inflammation-responsive delivery systems for the treatment of chronic inflammatory diseases. Drug Deliv. and Transl. Res. 11, 1475–1497 (2021).
23. Howard, M. D. et al. Nanocarriers for Vascular Delivery of Anti-Inflammatory Agents. Annu. Rev. Pharmacol. Toxicol. 54, 205–226 (2014).
24. Cheng, J., Ji, R., Gao, S.-J., Du, F.-S. & Li, Z.-C. Facile Synthesis of Acid-Labile Polymers with Pendent Ortho Esters. Biomacromolecules 13, 173–179 (2012).
25. Seo, Y. H. et al. Rational design for enhancing inflammation-responsive in vivo chemiluminescence via nanophotonic energy relay to near-infrared AIE-active conjugated polymer. Biomaterials 84, 111–118 (2016).
26. García, F. & Smulders, M. M. J. Dynamic covalent polymers. J. Polym. Sci. Part A: Polym. Chem. 54, 3551–3577 (2016).

27. Chen, M., Zhou, L., Wu, Y., Zhao, X. & Zhang, Y. Rapid Stress Relaxation and Moderate Temperature of Malleability Enabled by the Synergy of Disulfide Metathesis and Carboxylate Transesterification in Epoxy Vitrimers. ACS Macro Lett. 8, 255–260 (2019).
28. Smart polymers and their applications. (Woodhead Publishing, is an imprint of Elsevier, 2014).
29. White, S. R. et al. Autonomic healing of polymer composites. Nature 409, 794–797 (2001).
30. Kosarli, M., Bekas, D., Tsirka, K. & Paipetis, A. S. Capsule-based self-healing polymers and composites. in Self-Healing Polymer-Based Systems 259–278 (Elsevier, 2020). doi:10.1016/B978-0-12-818450-9.00010-6.
31. Zhu, D. Y., Rong, M. Z. & Zhang, M. Q. Self-healing polymeric materials based on microencapsulated healing agents: From design to preparation. Progress in Polymer Science 49–50, 175–220 (2015).
32. Blaiszik, B. J. et al. Self-Healing Polymers and Composites. Annu. Rev. Mater. Res. 40, 179–211 (2010).
33. Islam, S. & Bhat, G. Progress and challenges in self-healing composite materials. Mater. Adv. 2, 1896–1926 (2021).
34. Bekas, D. G., Tsirka, K., Baltzis, D. & Paipetis, A. S. Self-healing materials: A review of advances in materials, evaluation, characterization and monitoring techniques. Composites Part B: Engineering 87, 92–119 (2016).
35. Dry, C. & McMillan, W. Three-part methylmethacrylate adhesive system as an internal delivery system for smart responsive concrete. Smart Mater. Struct. 5, 297–300 (1996).

36. Toohey, K. S., Sottos, N. R., Lewis, J. A., Moore, J. S. & White, S. R. Self-healing materials with microvascular networks. Nature Mater 6, 581–585 (2007).
37. Patrick, J. F. et al. Continuous Self-Healing Life Cycle in Vascularized Structural Composites. Adv. Mater. 26, 4302–4308 (2014).
38. Trask, R. S. & Bond, I. P. Biomimetic self-healing of advanced composite structures using hollow glass fibres. Smart Mater. Struct. 15, 704–710 (2006).
39. Yarin, A. L., Pourdeyhimi, B. & Ramakrishna, S. Fundamentals and applications of micro and nanofibers. (2014).
40. Toohey, K. S., Hansen, C. J., Lewis, J. A., White, S. R. & Sottos, N. R. Delivery of Two-Part Self-Healing Chemistry via Microvascular Networks. Adv. Funct. Mater. 19, 1399–1405 (2009).
41. Hansen, C. J. et al. Self-Healing Materials with Interpenetrating Microvascular Networks. Adv. Mater. 21, 4143–4147 (2009).
42. Lee, M. W., An, S., Yoon, S. S. & Yarin, A. L. Advances in self-healing materials based on vascular networks with mechanical self-repair characteristics. Advances in Colloid and Interface Science 252, 21–37 (2018).
43. Xu, J. et al. Intrinsic self-healing polymers for advanced lithium-based batteries: Advances and strategies. Applied Physics Reviews 7, 031304 (2020).
44. Wool, R. P. & O'Connor, K. M. A theory crack healing in polymers. Journal of Applied Physics 52, 5953–5963 (1981).

45. Otts, D. B., Zhang, P. & Urban, M. W. High Fidelity Surface Chemical Imaging at 1000 nm Levels: Internal Reflection IR Imaging (IRIRI) Approach. Langmuir 18, 6473–6477 (2002).
46. Urban, M. W. Vibrational spectroscopy of molecules and macromolecules on surfaces. (Wiley, 1993).
47. Blanc, F. et al. Dynamic Nuclear Polarization NMR Spectroscopy Allows High-Throughput Characterization of Microporous Organic Polymers. J. Am. Chem. Soc. 135, 15290–15293 (2013).
48. Brown, E. N. Use of the tapered double-cantilever beam geometry for fracture toughness measurements and its application to the quantification of self-healing. The Journal of Strain Analysis for Engineering Design 46, 167–186 (2011).
49. Lee, M. W., Sett, S., An, S., Yoon, S. S. & Yarin, A. L. Self-Healing Nanotextured Vascular-like Materials: Mode I Crack Propagation. ACS Appl. Mater. Interfaces 9, 27223–27231 (2017).
50. Salman, S. D., Leman, Z., Sultan, M., Ishak, M. & Cardona, F. Effect of kenaf fibers on trauma penetration depth and ballistic impact resistance for laminated composites. Textile Research Journal 87, 2051–2065 (2017).
51. Tan, P. S., Somashekar, A. A., Casari, P. & Bhattacharyya, D. Healing efficiency characterization of self-repairing polymer composites based on damage continuum mechanics. Composite Structures 208, 367–376 (2019).
52. Zhang, F. et al. Self-healing mechanisms in smart protective coatings: A review. Corrosion Science 144, 74–88 (2018).

53. Brancart, J. et al. Atomic force microscopy–based study of self-healing coatings based on reversible polymer network systems. Journal of Intelligent Material Systems and Structures 25, 40–46 (2014).
54. Rahman, Md. W. & Shefa, N. R. Minireview on Self-Healing Polymers: Versatility, Application, and Prospects. Advances in Polymer Technology 2021, 1–12 (2021).
55. Flynt, J. A Detailed History of 3D Printing. 3D insider http://3dinsider.com/3d-printing-history (2022).
56. RepRap, C. RepRap. RepRap https://reprap.org/wiki/RepRap.
57. Moilanen, J. Results from 3D printing survey 2013. Longitudinal results https://www.este.it/images/file-pdf/3D-Printing_Survey2013.pdf (2022).
58. Saptarshi, S. M. & Zhou, Dr. C. Basics of 3D Printing. in 3D Printing in Orthopaedic Surgery 17–30 (Elsevier, 2019). doi:10.1016/B978-0-323-58118-9.00002-6.
59. Pagac, M. et al. A Review of Vat Photopolymerization Technology: Materials, Applications, Challenges, and Future Trends of 3D Printing. Polymers 13, 598 (2021).
60. Shahrubudin, N., Lee, T. C. & Ramlan, R. An Overview on 3D Printing Technology: Technological, Materials, and Applications. Procedia Manufacturing 35, 1286–1296 (2019).
61. Düzgün, D. E. & Nadolny, K. Continuous liquid interface production (CLIP) method for rapid prototyping. Journal of Mechanical and Energy Engineering 2, 5–12 (2018).
62. Kawata, S., Sun, H.-B., Tanaka, T. & Takada, K. Finer features for functional microdevices. Nature 412, 697–698 (2001).

63. Majumdar, J. D., Madapana, D. & Manna, I. 3-D Printing by Laser-Assisted Direct Energy Deposition (LDED): The Present Status. Trans Indian Natl. Acad. Eng. 6, 933–953 (2021).
64. Zikulnig, J. & Kosel, J. Flexible Printed Sensors—Overview of Fabrication Technologies. in Reference Module in Biomedical Sciences B9780128225486000000 (Elsevier, 2021). doi:10.1016/B978-0-12-822548-6.00010-8.
65. Gülcan, O., Günaydın, K. & Tamer, A. The State of the Art of Material Jetting—A Critical Review. Polymers 13, 2829 (2021).
66. Materialise, C. Powder based 3D printing, without the lasers. Materialise https://www.materialise.com/en/manufacturing/3d-printing-technology/multi-jet-fusion (2022).
67. Lewis, J. A. Direct Ink Writing of 3D Functional Materials. Adv. Funct. Mater. 16, 2193–2204 (2006).
68. Rocha, V. G., Saiz, E., Tirichenko, I. S. & García-Tuñón, E. Direct ink writing advances in multi-material structures for a sustainable future. J. Mater. Chem. A 8, 15646–15657 (2020).
69. Zhou, L., Fu, J. & He, Y. A Review of 3D Printing Technologies for Soft Polymer Materials. Adv. Funct. Mater. 30, 2000187 (2020).
70. Layani, M., Wang, X. & Magdassi, S. Novel Materials for 3D Printing by Photopolymerization. Adv. Mater. 30, 1706344 (2018).
71. Halloran, J. W. Ceramic Stereolithography: Additive Manufacturing for Ceramics by Photopolymerization. Annu. Rev. Mater. Res. 46, 19–40 (2016).

72. Zeng, Y. et al. 3D printing of hydroxyapatite scaffolds withgood mechanical and biocompatible properties by digital light processing. J Mater Sci 53, 6291–6301 (2018).
73. Torrado, A. R. et al. Characterizing the effect of additives to ABS on the mechanical property anisotropy of specimens fabricated by material extrusion 3D printing. Additive Manufacturing 6, 16–29 (2015).
74. Li, N., Li, Y. & Liu, S. Rapid prototyping of continuous carbon fiber reinforced polylactic acid composites by 3D printing. Journal of Materials Processing Technology 238, 218–225 (2016).
75. Patel, D. K. et al. Highly Stretchable and UV Curable Elastomers for Digital Light Processing Based 3D Printing. Adv. Mater. 29, 1606000 (2017).
76. Du, K. et al. Digital Light Processing 3D Printing of PDMS-Based Soft and Elastic Materials with Tunable Mechanical Properties. ACS Appl. Polym. Mater. 3, 3049–3059 (2021).
77. Odent, J. et al. Highly Elastic, Transparent, and Conductive 3D-Printed Ionic Composite Hydrogels. Adv. Funct. Mater. 27, 1701807 (2017).
78. Mironov, V. et al. Organ printing: Tissue spheroids as building blocks. Biomaterials 30, 2164–2174 (2009).
79. Goldmann, T. & Gonzalez, J. S. DNA-printing: utilization of a standard inkjet printer for the transfer of nucleic acids to solid supports. Journal of Biochemical and Biophysical Methods 42, 105–110 (2000).

80. Xu, T. et al. Viability and electrophysiology of neural cell structures generated by the inkjet printing method. Biomaterials S0142961206001372 (2006) doi:10.1016/j.biomaterials.2006.01.048.
81. Huerta-Reyes, M. & Aguilar-Rojas, A. Three-dimensional models to study breast cancer (Review). Int J Oncol 58, 331–343 (2021).
82. Willson, K., Ke, D., Kengla, C., Atala, A. & Murphy, S. V. Extrusion-Based Bioprinting: Current Standards and Relevancy for Human-Sized Tissue Fabrication. in 3D Bioprinting (ed. Crook, J. M.) vol. 2140 65–92 (Springer US, 2020).
83. Keriquel, V. et al. In vivo bioprinting for computer- and robotic-assisted medical intervention: preliminary study in mice. Biofabrication 2, 014101 (2010).
84. Chimene, D., Lennox, K. K., Kaunas, R. R. & Gaharwar, A. K. Advanced Bioinks for 3D Printing: A Materials Science Perspective. Ann Biomed Eng 44, 2090–2102 (2016).
85. Gungor-Ozkerim, P. S., Inci, I., Zhang, Y. S., Khademhosseini, A. & Dokmeci, M. R. Bioinks for 3D bioprinting: an overview. Biomater. Sci. 6, 915–946 (2018).
86. Donderwinkel, I., van Hest, J. C. M. & Cameron, N. R. Bio-inks for 3D bioprinting: recent advances and future prospects. Polym. Chem. 8, 4451–4471 (2017).
87. Ullah, S. & Chen, X. Fabrication, applications and challenges of natural biomaterials in tissue engineering. Applied Materials Today 20, 100656 (2020).

88. Mao, H. et al. Recent advances and challenges in materials for 3D bioprinting. Progress in Natural Science: Materials International 30, 618–634 (2020).
89. Decante, G. et al. Engineering bioinks for 3D bioprinting. Biofabrication 13, 032001 (2021).
90. Vanaei, S., Parizi, M. S., Vanaei, S., Salemizadehparizi, F. & Vanaei, H. R. An Overview on Materials and Techniques in 3D Bioprinting Toward Biomedical Application. Engineered Regeneration 2, 1–18 (2021).
91. Peak, C. W., Carrow, J. K., Thakur, A., Singh, A. & Gaharwar, A. K. Elastomeric Cell-Laden Nanocomposite Microfibers for Engineering Complex Tissues. Cel. Mol. Bioeng. 8, 404–415 (2015).
92. Shie, M.-Y. et al. 3D Printing of Cytocompatible Water-Based Light-Cured Polyurethane with Hyaluronic Acid for Cartilage Tissue Engineering Applications. Materials 10, 136 (2017).
93. Tibbitt, M. W. & Anseth, K. S. Hydrogels as extracellular matrix mimics for 3D cell culture. Biotechnol. Bioeng. 103, 655–663 (2009).
94. Zou, Y. et al. "Click" chemistry in polymeric scaffolds: Bioactive materials for tissue engineering. Journal of Controlled Release 273, 160–179 (2018).
95. Nair, L. S. & Laurencin, C. T. Biodegradable polymers as biomaterials. Progress in Polymer Science 32, 762–798 (2007).
96. Beheshtizadeh, N., Lotfibakhshaiesh, N., Pazhouhnia, Z., Hoseinpour, M. & Nafari, M. A review of 3D bio-printing for bone and skin tissue engineering: a commercial approach. J Mater Sci 55, 3729–3749 (2020).

97. Albanna, M. et al. In Situ Bioprinting of Autologous Skin Cells Accelerates Wound Healing of Extensive Excisional Full-Thickness Wounds. Sci Rep 9, 1856 (2019).
98. Matai, I., Kaur, G., Seyedsalehi, A., McClinton, A. & Laurencin, C. T. Progress in 3D bioprinting technology for tissue/organ regenerative engineering. Biomaterials 226, 119536 (2020).
99. Murphy, S. V. & Atala, A. 3D bioprinting of tissues and organs. Nat Biotechnol 32, 773–785 (2014).
100. Wouters, O. J., McKee, M. & Luyten, J. Estimated Research and Development Investment Needed to Bring a New Medicine to Market, 2009-2018. JAMA 323, 844 (2020).
101. Gaharwar, A. K., Arpanaei, A., Andresen, T. L. & Dolatshahi-Pirouz, A. 3D Biomaterial Microarrays for Regenerative Medicine: Current State-of-the-Art, Emerging Directions and Future Trends. Adv. Mater. 28, 771–781 (2016).
102. Datta, P., Dey, M., Ataie, Z., Unutmaz, D. & Ozbolat, I. T. 3D bioprinting for reconstituting the cancer microenvironment. npj Precis. Onc. 4, 18 (2020).
103. Byambaa, B. et al. Bioprinted Osteogenic and Vasculogenic Patterns for Engineering 3D Bone Tissue. Adv. Healthcare Mater. 6, 1700015 (2017).
104. Rupnick, M. A. et al. Adipose tissue mass can be regulated through the vasculature. Proc. Natl. Acad. Sci. U.S.A. 99, 10730–10735 (2002).
105. Zhang, Y. et al. 3D Composite Bioprinting for Fabrication of Artificial Biological Tissues. Int J Bioprint 7, (2021).

106. Martín-Noguerol, T. et al. Hybrid computed tomography and magnetic resonance imaging 3D printed models for neurosurgery planning. Ann. Transl. Med. 7, 684–684 (2019).

CHAPTER

2

OBJECTIVES

2.1 Thesis objectives

As already discussed, advanced polymers have the capacity of promoting key scientific developments and thus, impacting greatly in fields ranging from ecology to personalized medicine. However, there are still plenty of obstacles to achieve advanced polymeric materials as well as successfully generating them at industrial scale. Therefore, the aim of the present thesis is:

(I) To study and develop a polymer-based *self-healing system* capable of *successfully* performing *autonomously* at harsh environments (*low temperatures*) aimed for its application in composite materials. Due to the low reactivity and potential lack of flowability derived from the environmental conditions, a proper monomer and catalyst selection will be critical for its successful performance. Additionally, the system's inclusion into the final compounds should be studied and designed to fit within industrial manufacturing practices to ensure its optimal transference to real applications. The work carried to demonstrate the system's feasibility is presented in Chapter 3.

(II) To generate novel polymeric materials with the capacity of achieving and tunning at will the appropriate properties of softness, viscoelasticity and transparency from its synthetic chemical design to be used as photocurable 3D printing materials. To manufacture 3D printed objects possessing variable mechanical properties through its composition (i.e., hardness) using a single polymeric material. The results derived from the studies in the synthesis and characterization of UV-curing polymers with tuneable properties are shown in Chapter 4.

(III) To create relevant 3D cellular models through high-throughput 3D bioprinting. To achieve it, a study and optimization of both the polymeric bioink systems and the overall 3D bioprinting platform should be performed. The studies and works carried on about this topic are reported in Chapter 5.

CHAPTER

3

SELF-HEALING SYSTEM FOR LOW AND ULTRA-LOW TEMPERATURES

Composites: Part A 145 (2021) 106335

Contents lists available at ScienceDirect

Composites Part A

journal homepage: www.elsevier.com/locate/compositesa

Development of a Highly Efficient Extrinsic and Autonomous Self-Healing Polymeric System at Low and Ultra-Low Temperatures for High-Performance Applications

Guillem Romero-Sabat,*[a] Elena Gago-Benedí,[a] Joan Josep Roa Rovira,[b] David González-Gálvez,[a] Antonio Mateo,[b] Sandra Medel,[a] Ainhoa Tolentino Chivite[a]

[a] LEITAT Technological Center, Carrer Innovació 2, 08225, Terrassa, Barcelona, SPAIN

[b] Department of Materials Science and Metallurgical Engineering, Universitat Politècnica de Catalunya, Campus Diagonal Besòs-EEBE, Barcelona 08019, SPAIN

*gromero@leitat.org

https://doi.org/10.1016/j.compositesa.2021.106335

Received 26 November 2020; Received in revised form 5 February 2021; Accepted 13 February 2021

Available online 5 March 2021

Abstract

There is a growing demand of self-healing materials to overcome the costs derived from repairing and substituting pieces and components due continuous damages. Among the pursued strategies, the development of self-healing systems capable of operate at real low temperatures remains unsolved. In this study, we report the development of an extrinsic self-healing system for composite materials that has demonstrated an efficiency above 100% at low/ultra-low temperatures. This mechanism is based on the Ring-Opening Metathesis Polymerization (ROMP) of a blend of 5-ethylidenenorbornene/dicyclopentadiene (ENB/DCPD) monomers in the presence of ruthenium-based 3rd generation Grubbs' catalyst (G3). The blend was microencapsulated in formaldehyde-free polyurea vessels and dispersed into three different commercial epoxy resins. Tapered Double Cantilever Beam (TDCB) specimens of the modified resins were manufactured, tested, and healed at low/ultra-low temperature conditions completely autonomously. All samples showed high self-healing efficiency, demonstrating the potential incorporation in real composite materials for high performance fields.

KEYWORDS: *Smart materials; Particle-reinforcement; Damage tolerance; Mechanical testing; Self-Healing.*

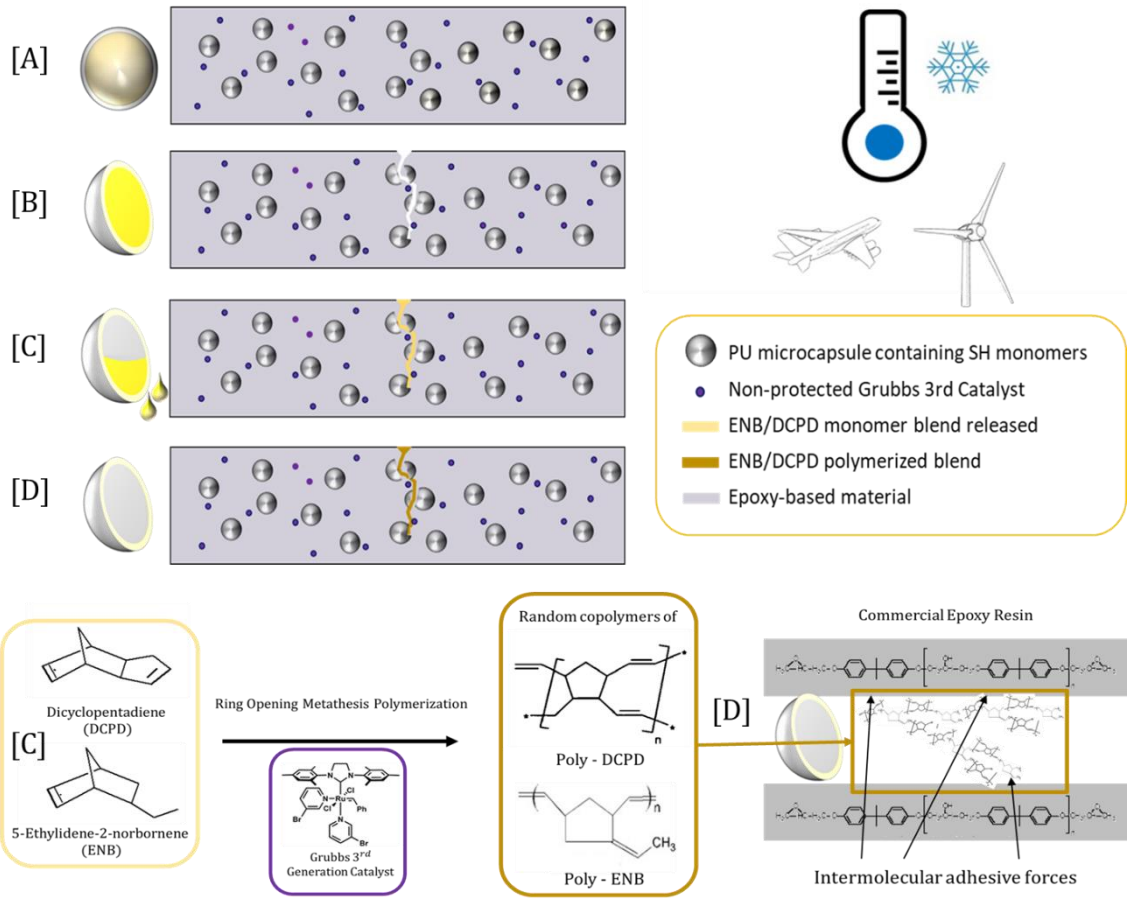

Scheme 3.1. Scheme of the extrinsic ROMP-based self-healing system developed in this work for epoxy-based materials used in high demanding fields efficient at ultra-low temperatures. The self-healing mechanism reported in this work follows the same ROMP-based chemistry as previous bibliography [10,12,19,26]. In short, strained cyclic olefins with no bulky groups around the double bonds such as 5-Ethylidiene-2-norbornene (ENB) and Dicyclopentadiene (DCPD) are microencapsulated and dispersed in epoxy-based materials. When a crack appears (due to erosion or external damage, for example), it breaks the composite along with the capsules, the monomers are released from their vessels and reacts at low temperature (-20 °C) in presence of a Ru-based catalyst (3rd Generation Grubbs Catalyst) previously embedded into the material to generate a crosslinked random copolymer of poly-ENB/DCPD, generating an adhesive layer and attaching both sides of the damaged composite. With this, the material is healed and its operating shelf-life, increased.

3.1 Introduction

Fibre reinforced plastics (FRP) are becoming more and more popular due to their improved properties allowing their use in applications that traditionally have been reserved to other compounds such as metallic and ceramic materials.[1] The main advantage of this class of composite materials is their low density, which, in combination to their mechanical properties, enable the obtention of materials that are both strong and lightweight. Weight reduction is critical in several fields, as allows an enhanced performance while providing an overall cost reduction. Thus, the lightweight materials market is growing much faster than the overall materials market.[2]

With all, these materials present some undesired properties. Among those, erosion resistance due to constant loading conditions (I.e. dynamic and impact damage) is usually poor.[3,4] This erosion process can pose a severe threat to the overall integrity of the polymeric composite structure at the long pace, preventing the full inclusion of FRPs in structural pieces for its application in fields where high standards are required. Moreover, the current maintenance of FRP is posing both a technical challenge for critical structural parts as well as a great economical expense, mostly related to the fact that the possible caused damage is not always visible to the naked eye but at microscopic level.[5] In order to fully introduce those materials in some of the high-performance fields such as the automotive, wind power or aeronautic industries that will work in harsh, real conditions, there is a need for increasing the FRP on-site resistance to the erosion damage and thus, enlarging its optimum operating life in a way that not includes a higher expense in human maintenance of the materials.

Among the studied strategies used for increasing FRPs durability, service life and reliability, the development of Self-Healing (SH) materials has received a lot of attention during the last decade. By mimicking biological systems, these composite materials are designed with the ability to trigger a self-repairing response without any or with very little external human intervention when an internal or external damage is produced. Through this strategy, is possible to enhance the lifespan of these polymer composites preventing simultaneously a catastrophic failure of critical part as well as significantly reducing the maintenance of these structures. For all these reasons, SH materials are called to be the next generation of materials for high performance applications.[6,7]

SH materials can be classified broadly into two types: intrinsic and extrinsic.[6] The SH process in intrinsic-type materials is due to the material's inherent characteristics and functionalities,[8,9] whereas in extrinsic SH materials the damage is recovered by the release of a healing agent inside the cracks from separated microcontainers embedded in the matrix.[10,11] Although intrinsic SH materials can provide a reiterative and therefore, theoretical longer SH activity, they are in need of a relative strong external stimuli such as heat or light as well as they have lower healing volume than extrinsic systems.[12–14] In epoxy-based FRP, with some exceptions in the recent years,[13,15] the main applied system is the extrinsic SH. While vasculature-like structures have been reported as SH containers, they still present scale-up and implementation problems,[13,16,17] leaving the incorporation of microcapsules as the prime methodology for this approach. Overall, experimental results and literature seem to indicate that up to now, the SH approach with the highest potential of being used in real-life applications is the one based in microcapsule addition.[18]

The microcapsule SH mechanism starts when the epoxy-based composite material becomes eroded and thus, micro-cracks are generated, spreading through the material. Crack propagation causes the rupture of the embedded, fragile microcapsules and the release of the healing agent that flows into the damaged area (Scheme 3.1 [A, B, C]). Consequently, the healing agent encounters with another embedded chemical trigger (such as a catalyst or another reactive healing agent) and polymerizes, forming a thin layer that leads to a bonding of the crack faces back together, preventing the crack propagation, delaying the erosion effect, healing the system and therefore, increasing the material's lifetime (Scheme 3.1, [D]).

From the wide variety of healing agents used for extrinsic SH applications (such as metathesis, polycondensation and epoxy-based systems),[16] the Ring Opening Metathesis Polymerization (ROMP) system, on which this work is based upon, has been extensively reported in the literature and it has proven to be an excellent polymerization technique for these SH thermoset materials. Studied first by White *et al.,* the ROMP of blends of cyclic olefins is used to synthesize linear and ramified polymers through the action of ruthenium-based catalyst (Grubbs', Hoveyda-Grubbs').[19] These catalysts can be either directly dispersed into the resin or encapsulated in waxy materials in order to avoid a deactivation by contact with the curing agent or exposure to air.[20] Even though there is a broad number of SH studies reporting the use of Grubbs catalyst, to the best of our knowledge this is the first work reporting the use of the 3rd generation of Grubbs catalyst, with a reactivity that can be up to six orders of magnitude higher than 2nd generation,[21] for SH applications.

5-Ethyldiene-2-norbornene (ENB) and dicyclopentadiene (DCPD) mixtures, (ENB/DCPD) microencapsulation has been reported using *in-situ* polymerization in urea-formaldehyde[22,23] and melamine-urea-

formaldehyde.[24] However, problems regarding the use of solvents or toxic formaldehyde, represent a drawback in the use of those materials. Above them, polyurea (PU) rises as a good alternative as it is stable at the different processing conditions —it has been used for other self-healing systems—[25], and the methodology is formaldehyde and solvent-free. The main problem may be envisaged from the use of isocyanates for the polyurea formation, but the risks are minimized by using non-volatile polyisocyanates and by assuring non-free isocyanates in the final product (using amine excess and following isocyanate consumption by FTIR).

Furthermore, current microcapsule-based SH materials have good performance under favourable and standard conditions, but have failed to provide a good repairing performance at harsh conditions, especially, at very low temperatures where the real operation conditions of the materials used in aerospace or windmill industry take place. In the last years, some ROMP-based systems with potential to operate at sub-zero temperatures have been demonstrated and microencapsulated, but the self-healing tests were only performed at room temperature and low yields were obtained.[26] Alternatively, Kalista and co-workers reported a system able to work at low temperatures but with the need of external sources of energy (ballistic impacts) to initiate the self-healing process.[27] Dong-Min, et al. demonstrated a successful dual microcapsule low temperature (-20 °C) self-healing, but for coating applications.[14] Regarding intrinsic self-healing systems, several works mention a development of a self-healing system operating at low temperature while really they refer to room temperature or near ambient temperature.[28,29] Only a few works such as the ones from Wu et al. or Xue et al. show a successful, real self-healing behaviour at low temperature[30,31] and, in none of them, the selected matrix is either a thermoset or epoxy-based. The failure of intrinsic systems for low temperature applications may be

hypothesized to be related to the need of a significant chain mobility to achieve the regeneration process.[12,32] Thus, all of these systems fail to provide an effective extrinsic-type and autonomous (understood as the unnecessity of needing any external agent, such as heat, pressure or radiation)[12] SH solution for internal structural components for the real environmental conditions that the materials will face.

Hence, in this study the authors report the development of i) an extrinsic self-healing system based on metathesis polymerization of ENB/DCPD blend, able to flow without phase separation at -70 °C and to react, in presence of 3rd generation Grubbs' catalyst from -20°C; ii) ENB/DCPD blend microencapsulation by interfacial polymerization in solvent-free non-toxic polyurea (PU) generating core-shell microcapsules with up to 70 wt.% load; iii) the incorporation of these microcapsules into different system of epoxy-based material without the necessity of protecting the metathesis catalyst; and iv) the demonstration that this system present an autonomous healing efficiency in fracture toughness assay with tapered double cantilever beam (TDCB)[33] higher than 100%, at cryogenic temperatures for all different epoxy systems.

3.2 Experimental section

3.2.1 Materials

Three different epoxy systems (Table 3.1) were used as polymeric matrixes for the specimen's manufacture. Grubbs 3rd generation (G3) and Hoveyda-Grubbs 2nd generation (HG2) catalysts were purchased from Sigma-Aldrich. 5-Ethyldiene-2-norbornene (ENB) and dicyclopentadiene (DCPD) were used as healing agents and purchased from Sigma-Aldrich (US). Voranate™ M 2940 (Dow, US) was used as polymeric isocyanate

(polymeric methylene diphenyl diisocyanate pMDI). Ethylendiamine (EDA), Diethylenetriamine (DETA) tetraethylenetriamine (TETA) and arabic gum from acacia tree were purchased from Sigma-Aldrich and used as received.

Table 3.1. Curing conditions of the different epoxy resin systems.

Resin system curing rate			Parts per weight	Curing process
Epoxy component	Amine curing agent	Accelerator		
Epikote RIMR 135	Epikure RIMH 137	-	100 : 35	Ramp at 0.5 °C/minute to 45 °C. Hold at 45 °C for 1h. Ramp at 1°C/min to 75°C. Hold at 75 °C for 4 hrs. Cool to ambient at 1 °C/min. Hold at RT for 19h. No post-cure process is performed
Araldite LY 556	Aradur HY 917	DY 070	100 : 90: 0.5-2	Ramp at 1 °C to 65 °C. Hodt at 65 °C for 1h. Rampt at 1 °C/min to 80 °C. Hold at 80 °C for 16h. Cool to RT at 1 °C/min. No post-cure cycle is performed
CTD 7.1 Part A	CTD 7.1 Part B	-	101 : 29.6	The sample is cured for 7 days at 25 °C. No post-cure process is performed

3.2.2 Sample preparation

ROMP monomers selection. At low temperatures, fast reaction kinetics are beneficial for the self-healing process. Therefore, strained cyclic olefins having no bulky groups around the double bonds, such as 5-ethylidene-2-norbornene (ENB) and dicyclopentadiene (DCPD), were selected due to their extensively reported high ROMP activity.[34] The ENB monomer has a higher ROMP reactivity than DCPD, however; DCPD is a good candidate since it provides enhanced mechanical properties to the final polymer such as fracture toughness and strength, which are achieved due to the cross-linked structure obtained after polymerization.[23]

Nevertheless, the melting point of DCPD (32.5 °C) limits its use as monomer as it is waxy at 20 °C and solid at sub-zero temperatures therefore, it cannot flow and fill the cracks. On the contrary, mixtures of ENB and DCPD present much lower melting points. It has been reported that mixtures of ENB/DCPD in a ratio of 95:5 are suitable to be used as liquid healing agent as low as –50 °C.[26]

Solubility and phase separation of the different ENB/DCPD blends were studied by mixing each monomer at its specific ratio in a vial and kept at room temperature, -20°C and -70°C from 1h to several days. The blends were visually observed periodically to determine possible phase separation. Moreover, their viscosity was quantified at the selected temperatures to demonstrate the blend's fluidity.

Catalyst Selection. Ru-based catalysts, such as those from the Grubbs' family, are reported as ROMP reaction catalysts in SH systems.[34,35] Since fast-initiating catalysts are necessary to promote metathesis at reduced temperatures according to our application,[36] two different Ru-based catalysts with low activation temperatures were selected[36]: Hoveyda Grubbs 2nd Generation (HG2), and Grubbs 3rd Generation Catalyst (G3). Reactivity of the different ring-opening metathesis catalysts (HG2 & G3) was verified in the first place visually and by FTIR through the formation of crosslinked networks of the polymer. Each catalyst (C= 0.1 wt.% to 0.004 wt.%) and ENB/DCPD (95:5 and 80:20 molar ratio) were mechanically mixed in a previously cooled vial (-72 °C) and kept at room temperature, –20 and -70 °C for up to 10 days. The maximum time the sample remained under study was 14 days. After the first qualitative screening, catalyst activity and reactivity were quantified by DSC through the assessment of the heat released from the exothermal ROMP reaction. To ensure that no reaction took place prior to the measurement, the blends were mixed with the selected catalyst at -72 °C and approximately,

samples of 5 mg of the mixtures were added to a cooled aluminium pan, hermetically closed and allowed to rest for 10 minutes prior to perform a heating ramp at 5 °C/min. In these experimental assays, the influence of the concentration of the catalyst of each kind was studied as a mean to determine the minimal quantity at such temperatures.

Procedure of ROMP monomers microencapsulation. ENB/DCPD microcapsules were prepared via interfacial polymerization. Initially, an oil-in-water emulsion was prepared by slow addition of the oil phase, composed of the healing agent (ENB/DCPD 80:20 wt.%) and the isocyanate (pMDI, quantity depending on the core/shell ratio), over 3.5 wt.% gum arabic aqueous solution and the mixture was stirred (2500 – 5000 rpm) in a homogenizer (Dispermat CV3-Plus with Homogenizer SR 03-01, VMA-Getzmann GMBH, Germany) for 20 minutes.

Later, the emulsion was transferred to a jacketed reactor, stirred at 400 rpm and EDA or TETA (1 – 5% aqueous solution, 1.1 – 1.5 eq) was added dropwise from a pressure compensated funnel. After the addition was completed, the temperature was increased and the mixture was stirred until a complete reaction of the pMDI with the amine occurs.

The resulting milky dispersion was filtered under vacuum (2 μm, Nylon) and washed with water twice. Finally, the cake was dried at 30 °C under vacuum to render a raw white solid.

Microcapsules dispersion in epoxy resins and Tappered Double Cantilever Beam (TDCB) specimens preparation. The unfilled, neat specimens were manufactured by carefully mixing the different components of each resin system on the specified proportions as stablished by the manufacturer (Table 3.1). For the synthesis of the SH specimens, a dispersion process based on previous bibliography was performed.[37] First, a specified amount of SH microcapsules (0 to 30 wt.%) and ruthenium-based catalyst (0.004 – 0.1 wt.% respect monomer weight)

were added into the epoxy component of the resin. Next, the mixture was mechanically stirred at 500 rpm using a Dispermat CV3 (VMA-Getzmann GMBH, Germany) at room temperature for 15 minutes. Then, the remaining resin components were added, followed by 5 minutes mixing at 800 rpm.

The mix was poured finally into a silicon mould with the TDCB geometry defined in previous works,[38] and cured in a staged protocol recommended by the manufacturer for a full cure process (Table 3.1). The additive containing self-healing resins were cured following the same procedure as the neat ones.

3.2.3 Characterization methods

Particle size. The average particle size and particle size distribution of the microcapsules were measured by laser diffraction using a Mastersizer 3000 (MAZ3000, 0.1 to 1000 µm range, Malvern Panalytical, UK).

Thermogravimetric Analysis (TGA). TGA was carried out with a Q500 thermobalance (TA Instruments, US). Resin samples were heated from 25 °C to 1000 °C at a 10 °C/min heating rate under air and nitrogen flow. The weight loss was recorded as a function of temperature.

Differential Scanning Calorimetry (DSC). The DSC was cooled to -75°C and then, a cooled sample of approximately 5mg was introduced ensuring the temperature did not surpass -70 °C. Each sample was heated in a ramp of 5 °C·min^{-1} from -65 °C to 150 °C and the onset temperature (T_{onset}) as well as the peak temperature (T_p) were recorded. Due to the system's high exothermic polymerization reaction, the $T_{onset}$of the system is used as reference to point the starting temperature of the self-healing.

Fourier transform infrared-attenuated total reflectance (FTIR-ATR). The infrared spectra were obtained by using an IR Affinity-1S CE

FTIR spectrophotometer (Shimadzu, Japan) in the 4000-500 cm^{-1} range and with a 1 cm^{-1} resolution (32 scans collected).

Microcapsules and composites morphology. Scanning Electron Microscope (SEM) micrographs were obtained with a SEM Touchscope JEOL JSM-6010LV (JEOL instruments, Japan) and a Phenom XL Desktop SEM at acceleration voltages of 5 kV. Prior to the SEM observation, the specimens were coated with a thin conductive layer by using a sputter coater (Cressington scientific instruments, 108 Auto).

For the characterization of inner part of microcapsules, thin slices of microcapsules embedded in Epikote:Epicure epoxy resin (see Section 2.4) are produced by using a RM2255 manual rotary microtome (Leica Biosystems, Germany).

After curing, the homogeneity of the microcapsules dispersion into the cured resin and their integrity were evaluated by SEM (Touchscope JEOL JSM-6010LV, JEOL, Japan). Thin slices of the material (40 μm thick) were obtained by Microtome (Leica MR 2255) and further metallized with Au.

Focused Ion Beam (FIB). Internal microstructure for the different tested specimens was characterized by micro-machining cross-sections at the central part of the different microspheres by means of focused ion beam (FIB). Cross-sectioning and the subsequent field emission scanning electron microscopy (FESEM) observations were conducted using a dual beam workstation (Zeiss Neon 40). A thin platinum layer was deposited on the region of interest prior to FIB with the main aim of reducing ion-beam damage. Then, a Ga^{+} ion source was used to mill the surface at a voltage of 30 kV. A final polishing of the cross-section was performed at a current of 500 pA in order to get more details related to microstructure of the different microspheres investigated in the present study.

Nuclear Magnetic Resonance (NMR). ^{1}H-NMR spectra are acquired in a Bruker Avance-II+ 600MHz (14 T). NMR spectra of the self-healing

loaded microcapsules were obtained in Deuterated Dichloromethane (DCM-d_2) and compared to the NMR spectra of extracted self-healing mixture after microcapsules swelling in acetone-d_6 and filtration through 0.45 μm pore nylon filters.

Viscosity of monomeric blends. The behaviour of the monomeric blends at different temperatures was quantified by measuring the elucidation time in a Ford 3 cup previously cooled at the selected temperature (-70, -20 °C, room temperature). For reference, a parallel measurement at 20 °C between the same monomer blend in the viscosity cup and in the Bohlin Gemini rheometer (Malvern Panalytical, UK) using a cone-plate geometry and a shear rate from 0 to 83 s^{-1} were performed.

Rheological behaviour of uncured epoxy resins. Instantaneous viscosities of the neat resins and the microcapsules loaded resins were determined at 25 °C under a shear rate from 0 to 83 s^{-1} using a parallel plate geometry in a Bohlin Gemini rheometer (Malvern Panalytical, UK).

Self-healing testing. As a mean to evaluate the self-healing performance and efficiency, a modified method based on the previously stablished by White *et al*. has been followed.[19] Shortly, the specimen was placed in an ultrafreezer at –80 °C for 48 h to ensure a homogeneous ultra-low temperature. Afterwards, in order to assure the correct direction of the propagation of the breaking line, a notch was made into the specimen using a sharp razor blade.

The cold specimen was loaded in the instrument and the tension-displacement test started while controlling the load in order to stop the experiment when a drop of force during the assay is detected. The temperature was registered during the assay using an infrared thermometer IAN 291541 (Powerfix Profi, Germany). Immediately after the test, the specimen was placed in a chest freezer of ultralow temperature (EHF, 78/86 from Equitec, Spain) and allowed to heal

keeping cryogenic conditions (–20 °C) for 48 h. After the healing time, the sample is cooled to –80 °C to ensure it remains cold during the assay and the test is performed again.

The overall duration of the measure, from the moment the specimen was removed from the ultrafreezer until it was placed again did not exceed 6 minutes and the specimen temperature did not achieve temperatures above -20 °C.

The specimens were tested by using the Instron 1341 machine working under loading control mode. The tests were conducted under displacement mode at a constant deformation speed of 5 mm·s^{-1}, which, carefully developed by previous investigations [19] helps to control the crack growth along the centre line of the brittle specimen.

The fracture healing efficiency in the case of quasi-static fracture conditions (η), can be calculated by using the following equation provided by previous studies[19,39]:

$$\eta\,(\%) = \frac{K_{c\ healed}}{K_{c\ virgin}} * 100 \qquad (1)$$

Equation 3.1. Self-healing efficiency equation for quasi-static fracture conditions.

Where η is defined as the ability of a healed sample to recover fracture toughness, Kc_{virgin} is the fracture toughness of the virgin specimen and Kc_{healed} is the fracture toughness of the healed specimen.

Typically, in order to calculate the sample toughness, it would be necessary to integrate the equation obtained from the load-displacement curve. However due to the specific geometry of the TDCB specimen, the sample toughness is equal to the critical load (Pc) multiplied by a geometrical constant (α), thus giving: $K_c = \alpha * P_c$; that can be simplified[40], therefore, reducing the equation to the following:

$$\eta\,(\%) = \frac{P_{c\ healed}}{P_{c\ virgin}} * 100 \qquad (2)$$

Equation 3.2. Simplified self-healing efficiency equation for quasi-static fracture conditions. Due to the TDCB geometry, the fracture toughness (Kc) can be substituted by the critical load (Pc) [40].

Pc, the critical load, is defined either as the point where the TDCB specimen breaks or the point in the load (N) vs displacement (d) curve where the load drops, meaning that the tensile test starts to propagate the crack generated by the razor blade. Moreover, surface morphology of the cured virgin and healed TDCB specimens were carefully studied by SEM to observe the possible differences in the microcapsule structure.

3.3 Results and discussion

3.3.1 Fluidity and Reactivity at different temperatures

The liquidity of the ENB/DCPD mixtures were studied at 1, 4, 24 and 72h. Neither phase separation nor appearance of solids was found at –70 and at -20 °C in monomer mixtures from 100:0 to 80:20 ENB/DCPD ratios. Although there was a proportional increment of the quantified values of viscosity as the temperature lowered and the ratio of DCPD monomer was increased (Figure 3.1), the maximum efflux time obtained was 16.6 s for the 80:20 blend at -70 °C, only 3.7 seconds above the liquid reference of 100:0 ENB, thus supporting the fluid behaviour observed at all studied temperatures and blends. For further research in this study, ratios of 95:5 and 80:20 were selected as, based on literature,[41] they were respectively the mixtures with higher reactivity and with more crosslinking capacity.

A first qualitative comparative assay between catalysts at different concentrations proved G3 to be the most active catalyst for the selected ENB/DCPD blends both at room temperature and at -20 °C, in coherence with previous reported data.[42]

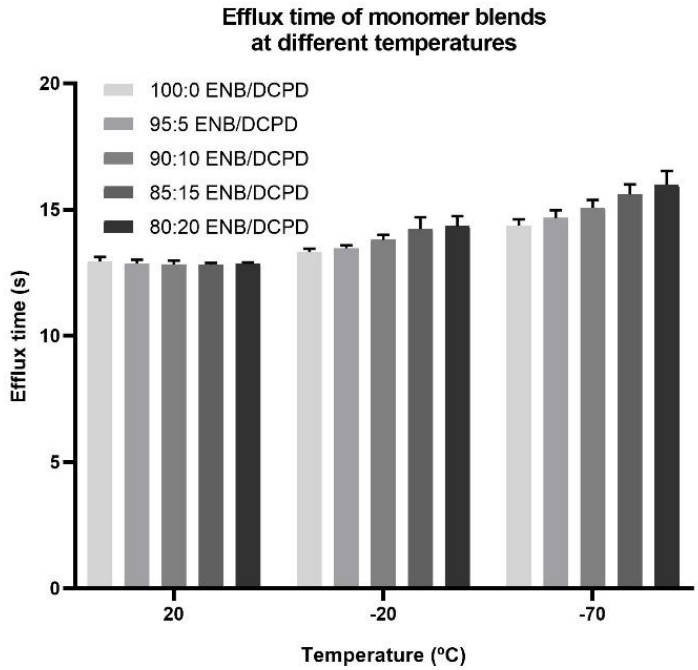

Figure 3.1. Graph showing the efflux time of the different monomer blends at different temperatures with a Ford #3 Cup. Pure ENB (100:0) was used as reference as the solidification temperature of ENB is set at -80 °C. Although at room temperature no difference was observed in the Efflux time, which is related to the material's viscosity, between the different blends, there is an observable increase when either the temperature is lowered or the ratio of DCPD monomer is increased, leading to the highest value at -70 °C and 80:20 ENB/DCPD. However, the time only increased for approximately 3s, demonstrating thus the fluidity of the blends even at ultra-low temperatures. No appearance of solids was observed in any blend at any temperature.

At -70°C there was no evidence of reaction of any blend with any catalyst concentration.

As a mean of obtaining quantifiable values for the reactivity of the catalysts at low temperature, blends of ENB/DCPD were produced again and mixed respectively with a high concentration of 0.1 wt.% of the selected catalysts (Table 3.2). HG2 exhibited both the T_{onset} and the T_p at

higher temperatures than those of G3. Moreover, a proportional reactivity pattern (lower T_{onset}) could be envisioned when a higher load of ENB was used. Over time, HG2 and G3 have been shown similar yields but G3 is a considerably better catalyst at low-T, presumably because dissociation of the electron-deficient 3-bromopyridine ligand is extremely rapid and/or because rebinding is slow, both of which contribute to favorable turnover conditions.[43] Acknowledging thus the lower reactivity of HG2 vs G3 for low temperature applications, HG2 was discarded from further work in this study.

Table 3.2. Summary of the T_{onset} and T_p of the different ENB/DCPD blends with 0.1 wt.% of HG2 and G3 catalyst.

	ENB/DCPD (wt.%)	T_{onset} (°C)	T_p (°C)
Hoveyda- Grubbs 2nd Catalyst at 0.1 wt.%	95:5	0.84	18.04
	80:20	1.90	17.91
Grubb's 3rd Catalyst at 0.1 wt.%	95:5	-22.66	2.36
	80:20	-18.94	4.42

In order to determine the optimal concentration of G3 catalyst for the SH systems, reactivity of 0.01 and 0.004 wt.% with different blends were produced and measured with DSC (Table 3.3).

The obtained results with the monomer reactivity are in coherence with all the data previously observed (Table 3.2) as well as the collected by other researchers.[26,42] First, it is observable that due to the DCPD's lower reactivity compared with the ENB monomer, the increase of DCPD content in the blend causes a decrease in both the T_{onset} as well as on the T_p. Moreover, the increment of catalyst shows evidence of lowering the activation temperature several degrees as assessed in the previous qualitative experiments.

Nonetheless, all the selected ratios at the chosen G3 catalyst concentration confirmed a good cryogenic reactivity and therefore, have potential to be used as a self-healing reactivity blend for the intended application.

Table 3.3. Summary of the T_{onset} and T_p of the different ENB/DCPD blends with 0.01 wt.% and 0.004 wt.% of G3 catalyst. Graphs and results of all other blends can be observed in the Suporting information.

	ENB/DCPD (wt.%)	T_{onset} (°C)	T_p(°C)
Grubb's 3rd Catalyst at 0.01 wt.%	95:5	-22.54	2.69
	80:20	-18.32	4.45
Grubb's 3rd Catalyst at 0.004 wt.%	95:5	-18.76	3.76
	80:20	-17.30	4.81

With all the collected data, the selected system for the encapsulation was ENB/DCPD 80:20 ratio monomer mixture with 0.01% G3 catalyst. This selection was considered a compromise between: i) suitable fluidity at both –20 °C and -70°C as well as good polymerization times at –20 °C, ii) the more crosslinked final polymers with theoretical mechanical improvement provided by higher contents of DCPD and iii) the economic cost of the last generation Grubbs catalyst.

3.3.2 Microcapsules synthesis

Interfacial polymerization methodology allows obtaining a wide range of microcapsules as there are several variables to play with: polyisocyanate and polyamine used, isocyanate/amine ratio, core/shell materials ratio, water/oil phase ratio in the emulsification step, emulsifier (type and amount), polyamine dilution, reaction temperature and stirring rate (both emulsification and polymerization steps). In addition, the microcapsules requirements were defined: minimum quantity of free isocyanate, <20µm diameter, minimum release produced by porosity,

maximum core/shell ratio and high temperature resistance (more than 200°C).

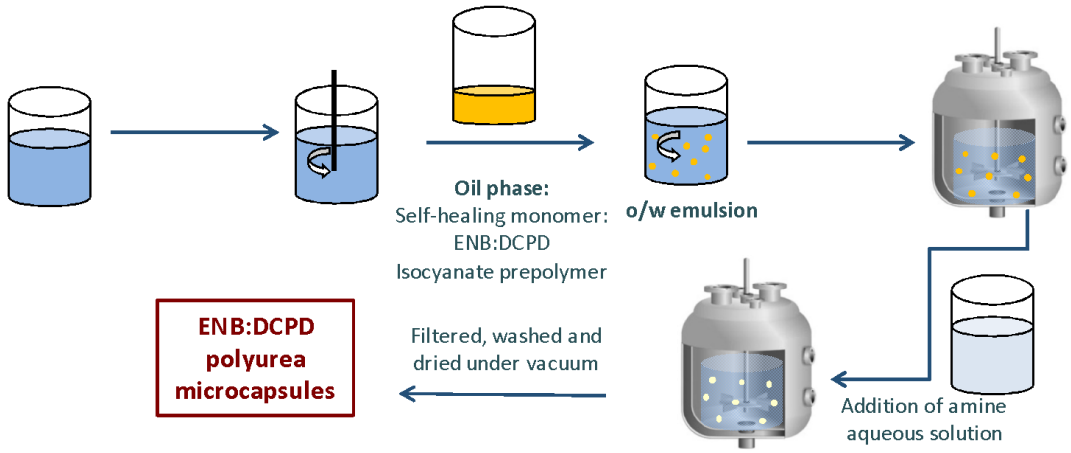

Figure 3.2. Scheme of the protocol for ENB/CDPD microcapsules synthesis.

First, the conditions of ENB/DCPD emulsion in water step were optimized an fixed as 70:30 water/oil ratio and 3-3.5% of Arabic Gum as emulsifier.[44]

In the encapsulation method developed, the oil phase is composed of END/DCPD (80:20 weight ratio), as previously stated, mixed with a low viscosity pMDI (Voranate™ M2940). Once the emulsion is formed, a diluted aqueous solution of the polyamine is added to react with pMDI and form the polyurea wall of the microcapsules (Figure 3.2).[44]

The effect of the variables of emulsion (stirring rate) and polymerization (amine type and concentration, reaction conditions) steps in the morphology, shell polymer conversion and thermal resistance of microcapsules have been studied and compared. This was investigated with the aim of obtaining robust and stable core-shell microcapsules with the maximum loading of healing core and with the highest thermal

resistance for the production of composites. Reaction conditions and properties of the obtained microcapsules (MC1-MC19) are gathered in Table 3.4, and their SEM images in Figure 3.3.

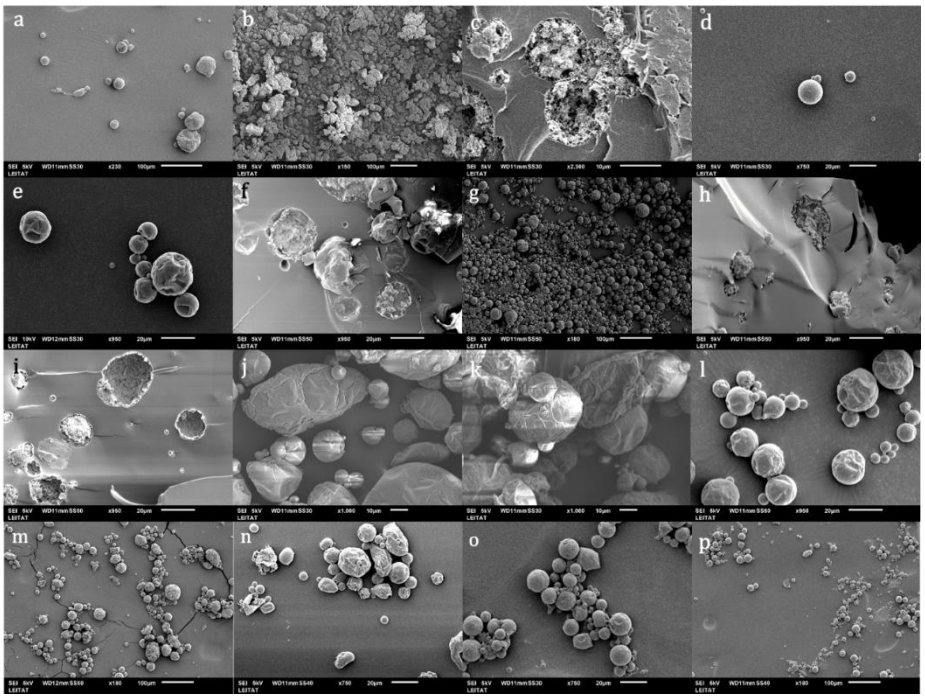

Figure 3.3. SEM images of the different synthesized microcapsules. a- MC1; b-MC3; c-MC4; d-MC5; e-MC6; f-MC7; g-MC8; h-MC9; i-MC11; j-MC12; k-MC13; l-MC14; m-MC15; n-MC17; o-MC18 and p-MC19.

First short alkyl chain polyamines were used (EDA, DETA and TETA) in order to minimize the ENB/DCPD release due to wall porosity (MC1-MC3). Only EDA rendered small individual spherical microcapsules, as DETA and TETA lead to coagulation (Figure 3.3 a).

When comparing the morphology of microcapsules with different core/shell ratios and fixed amine concentrations (1% aqueous solution added at a 1.1 ratio to isocyanates), MC1, MC4 and MC5 it was observed

Table 3.4. Summary of ENB/DCPD microencapsulation reaction conditions and results.

Entry	Emulsion step			Interfacial polymerization step					
	wt.% GA	Time (min)	Stirring (rpm)	Time (h)	Temperature (°C)	Stirring (rpm)	Amine	Amine:NCO ratio	Amine concentration (%)
MC1	3	10	3000	1+1+1	r.t.+50+70	300	EDA	1.1	1
MC2	3	10	3000	1+1+1	r.t.+50+70	300	DETA	1.1	1
MC3	3	10	3000	1+1+1	r.t.+50+70	300	TETA	1.1	1
MC4	3	10	3000	1+1+1	r.t.+50+70	300	EDA	1.1	1
MC5	3	10	3000	1+1+1	r.t.+50+70	300	EDA	1.1	1
MC6	3	10	3000	1+1+1	r.t.+50+70	300	EDA	1.1	4
MC7	3	10	3000	1+1+1	r.t.+50+70	300	EDA	1.1	10
MC8	3	10	3000	1+1+1	r.t.+50+70	300	EDA	1.5	1
MC9	3	10	3000	1+1+1	r.t.+50+70	300	EDA	1.5	4
MC10	3	10	3000	1+1+1	r.t.+50+70	300	EDA	1.5	10
MC11	3	10	3000	1+1+1	r.t.+50+70	300	EDA	2	1
MC12	3	10	3000	1+1+1	r.t.+50+70	300	EDA	1.1	4
MC13	3	10	3000	1+1+1	r.t.+50+70	300	EDA	1.1	4
MC14	3	10	3000	1+1	r.t.+50	300	EDA	1.1	1
MC15	3	10	3000	3 h	70 °C	300	EDA	1.1	1
MC16	3	10	3000	4 h	70 °C	300	EDA	1.1	1
MC17	3	10	3000	o.n.	70 °C	300	EDA	1.1	1
MC18	3	10	5000	1+1+1	r.t.+50+70	450	EDA	1.1	1
MC19	3.5	20	5000	1+1+1	r.t.+50+70	450	EDA	1.1	1

Entry	Core/shell ratio (Theorical)	MC size[a] (μm)	MC morphology	Degradation temperature[b] (°C)	Monomer content[b] (%)
MC1	70:30	21	Spherical	250	69
MC2	70:30	34	Bulk material	-	-
MC3	70:30	38	Bulk material	-	-
MC4	60:40	41	Spherical (matrix)	237	25
MC5	80:20	39	Spherical	217	69
MC6	70:30	23	Spherical (matrix)	246	71
MC7	70:30	25	Spherical (matrix)	-	-
MC8	70:30	23	Spherical	250	54
MC9	70:30	26	Spherical (matrix)	226	58
MC10	70:30	25	Spherical (matrix)	-	-
MC11	70:30	22	Spherical + elongated (mixture core/shell and matrix type)	-	-
MC12	80:20	41	Elongated + artefacts	-	-
MC13	90:10	39	Elongated + artefactsl	-	-
MC14	70:30	21	Spherical	242	63
MC15	70:30	21	Spherical + artefacts	251	70
MC16	70:30	20	Spherical + artefacts	249	69
MC17	70:30	20	Spherical + artefacts	244	67
MC18	70:30	14	Spherical	246	56
MC19	70:30	12	Spherical	246	70

[a] Median size determined in the Mastersizer 3000.[b] Determined by TGA.

that a spherical morphology was obtained at all the studied ratios: 60:40, 70:30, and 80:20 (Figure 3.3- a, c and d). Within this context, if both core/shell ratio and amine concentration were increased above 80:20 and up to 4% respectively to accelerate the reaction (MC12 and MC13), the microcapsules became slightly deformed in one axis presenting an elongated shape (Figure 3.3- j and k). This effect may be associated to insufficient material for wall forming and so particle merging. It is worth mentioning that 70:30 core:shell ratio MCs lead to closest contents of healing agents to theoretical value (70%) of the studied samples, resulting in most efficient encapsulation system. In addition, the rendered materials of 70:30 core:shell proportion showed higher degradation temperature (250 °C) when compared to other ratios.

On the other hand, the aforementioned systems present an incomplete isocyanate consumption during the chemical reaction as shown in the FTIR spectra by means of presence of NCO peak corresponding to the signal at 2272 cm^{-1}. In order to improve isocyanate reaction, the effect of both the equivalents of amine and its concentration in the aqueous solution were studied in microcapsules with 70:30 core/shell fixed ratios (MC1 and MC6-MC11). The increase of amine equivalents produced materials with less load of encapsulated healing monomer and the free-isocyanate presence in the product was only slightly reduced (Figure 3.4). The amine concentration did not show either a strong effect over isocyanate reactivity; furthermore, FESEM images of FIB crosscuts indicated that its increase led to microcapsules with a core-matrix structure instead of a core/shell structure. Within this observation, 1% EDA concentration with 1.1 amine equivalents to isocyanate were determined as best reactants system for polymerization.

Conversion of polyurea shell was further studied by the effect of reaction conditions: temperatures from room temperature to 70 °C and reaction

times in a range of 2h to overnight were applied (MC1 and MC14-MC17 microcapsules). Under milder conditions (MC1 and MC4), still a high quantity of free isocyanate was detected by FTIR (Figure 3.4). Reaction temperature and time were increased until non-free isocyanate was detected, what occurred at 70 °C and overnight reaction (Figure 3.4), and thus full conversion was achieved. However, when the reaction was directly heated to 70 °C, the morphology of the capsules was more irregular when comparing to spherical morphologies obtained in mixtures initially stirred at 50°C for 1h (MC14), as depicted by the SEM micrographs (Figure 3.3- l).

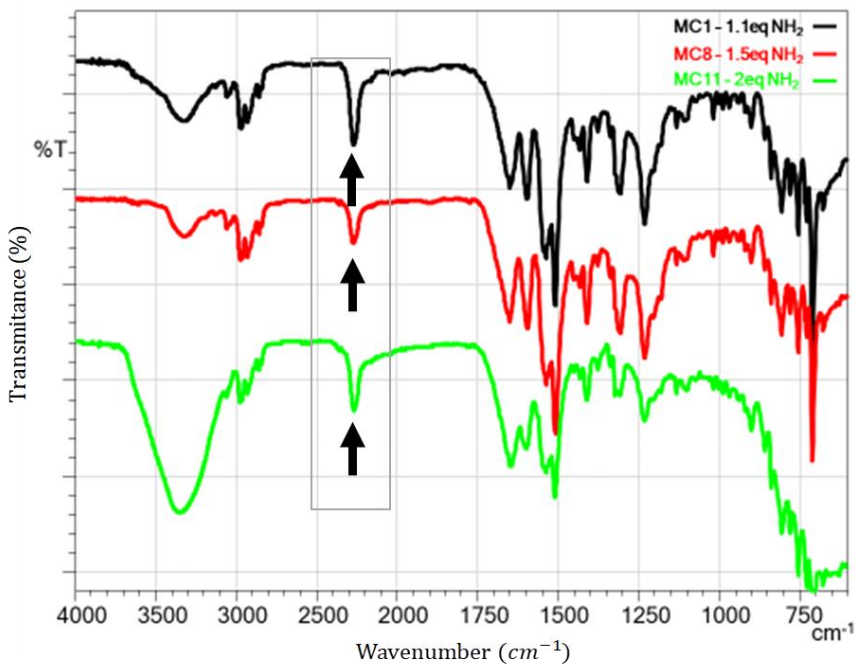

Figure 3.4. FTIR spectra of the microcapsules produced by using 1.1 (black), 1.5 (red) and 2 (green) equivalents of ethylenediamine. The differences in isocyanate content produced by the modification of added equivalents can be observed at 2272 cm^{-1} as pointed by the arrows and the box.

To better improve the encapsulation efficiency, the particle size distribution and shape of the microcapsules were optimized by modifying the parameters of the emulsion step (stirring rate and time), which is

critical over these properties in interfacial encapsulation.[45] Accordingly, an increase in rotor speed during the emulsion step from 3000 to 5000 rpm (MC18) reduced the particle size (D_{50}) from 21 to 14 µm, despite the presence of some irregularities (Figure 3.3- o) and lower healing content, 56%. The increase of emulsion stirring time from 10 to 20 min and the higher surfactant concentration, 3.5% gum Arabic (MC19) lead to core-shell spherical regular microcapsules (Figure 3.3- p and Figure 3.6 Top), with an encapsulation efficiency (relation between theoretical and measured monomer content) close to 100%. Although the modification

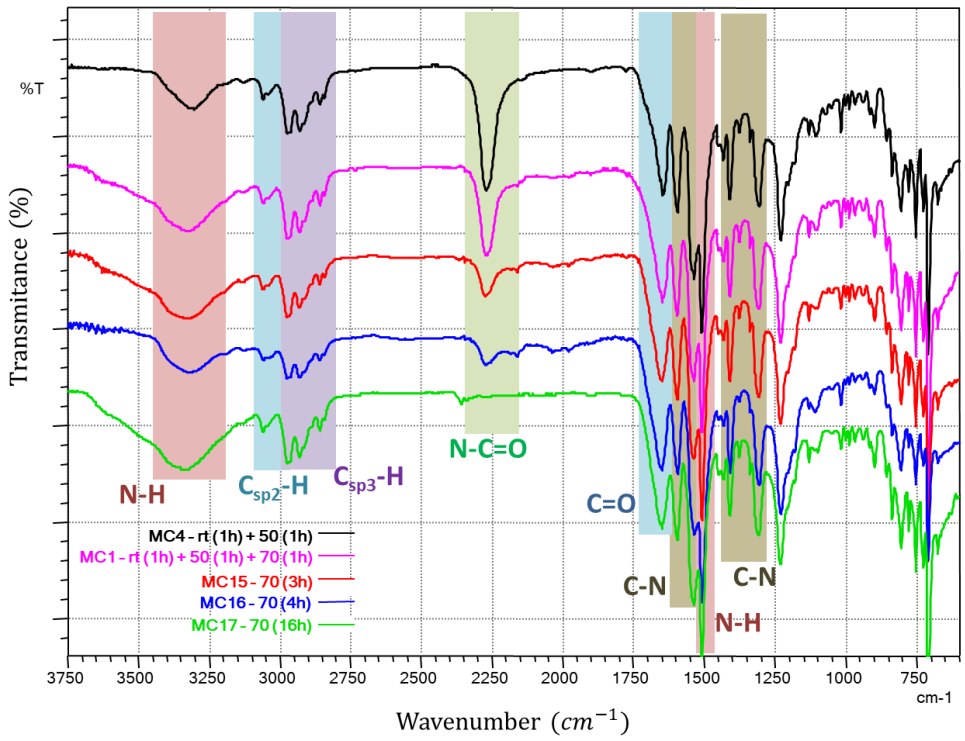

Figure 3.5. Normalised FT-IR spectra of the encapsulation reaction at different temperatures and times. The differences in isocyanate content produced by the modification of procedure can be clearly observed at 2272 cm^{-1} as pointed by the decrease of the peak in comparison with the stable N-H signal at 1500 cm^{-1}.

of some parameters such as stirring velocity or emulsifier concentration and its effect on microcapsule morphology and size distribution are well

known, it's interesting to observe the effect of amine to isocyanate ratio and more importantly, amine concentration in the microcapsule core structure. As clearly depicted in Figure 3.6, an increase of the amine concentration is the main factor producing the change from a matrix-core type (top) to an almost full-reacted sphere (bottom), thus causing a huge decrease in the load capacity of the microvessel.

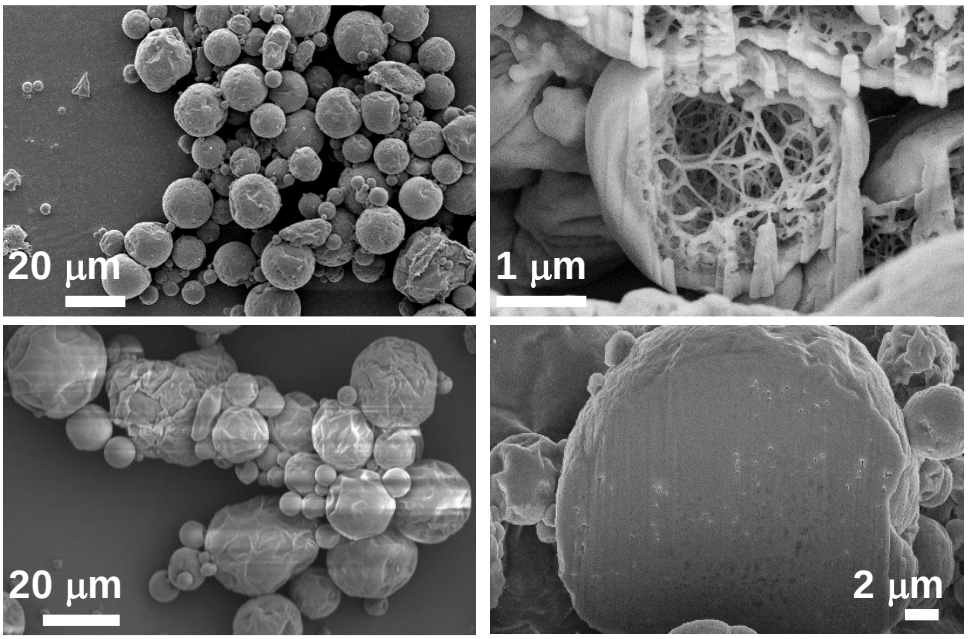

Figure 3.6. SEM (left) and FIB-FESEM (right) micrographs of ENB/DCPD polyurea microcapsules synthesized employing TOP 1.1 eq of amine and 1wt.% of amine aqueous solution (Table 3.4, Entry MC19) and BOTTOM 1.5 eq of amine and 4wt.% of amine aqueous solution (Table 3.4, Entry MC9).

As physical-chemical characterization has demonstrated that MC19 microcapsules fulfilled desired proprieties, they were chosen for their incorporation in the epoxy resin.

3.3.3 Incorporation of ENB/DCPD microcapsules in epoxy resin

Achieving a homogeneous distribution of both SH capsules and ROMP catalyst is imperative to guarantee equal self-healing properties along the

manufactured specimen. Moreover, SH additive homogeneity is necessary to increase the contact probability between the released content and curing agent after damage-induced breakage of the capsules. Homogeneous distribution of both SH capsules and ROMP catalyst has been successfully achieved as it was observed by SEM micrographs of cured epoxy resin with 10 and 20 wt.% (supporting information). Furthermore, the used concentration of SH additives is above the observed quantities for achieving a good reactivity thus, improving until almost a certain point the contact between monomer and catalyst in case of a crack.

Once an optimal distribution of the microcapsules over the resin was verified, as a mean to assess the process limitations, rheological studies of the instantaneous viscosity (mPa·s) on modified resins with different percentage of SH additives were performed prior to specimen manufacturing. Loads of 10, 20 and 30 wt.% of SH capsules were compared to the neat resin. Epoxy resin systems Epikote 135-Epikure 137 and Araldite LY556-Aradur 917 were chosen as references due to their posterior use in industrial infusion process, in which viscosities above 2000 mPa·s are not viable. For this reason, 2000 mPa·s was stablished as the limit-line.

From the rheological studies, we can determine that the viscous behaviour of the neat resin displays a non-Newtonian pattern, more specifically a shear-thinning tendency where the instantaneous viscosity decreases as the shear velocity increases. The same pattern is followed yet enhanced as more SH additives are introduced into the epoxy component. This effect is seen is both resins but more intensely in the Epikote-Epicure system.

In both studied systems, only loads of 10 wt.% always fulfil the viscosity requirements for the final applications, becoming thus the optimal load

for production processes with both epoxy systems in terms of achieving the highest possible load of SH additives while maintaining the potential industrial processability. However, upon certain shear, both epoxy systems loaded with 20 wt.% of MCs, displays values below the limit-line of viscosity. Thus, certain adaptations will allow higher loads if higher self-healing additives charge is needed.

Viscosity of CTD 7.1 epoxy system was not critical as the composite manufacture did not present the previous limitation. However, 10 wt.% of SH microcapsule loading was also used for this system with the aim of having the same quantity of self-healing additives among samples under study.

3.3.4 SH efficiency assessed by fracture test results

Once the SH additive load was stablished at 10 wt.% results of fracture TDCB specimens with and without microcapsules were compared and the SH efficiency was determined.

Initially, due to material shortage, the focus of study was limited to only neat and SH modified Epikote 135/137 epoxy resin specimens. Specimens containing 10 wt.% of SH additives were tested for the epoxy resin system, along with another neat epoxy resin samples used as reference. Samples of both kind of specimens were manufactured with the optimal geometry for fracture SH studies.[38,40,46] Tests evaluating the SH efficiency at cryogenic temperatures with both modified and unmodified resins were evaluated per triplicate and the results are summarized in Table 3.. While neat specimens exhibited a fracture force near 190 N, there is a reduction to 133 N when SH additives are included into the epoxy resin. Unlike other researchers reported,[47] SH additives produced a decrease on the fracture toughness values of the specimens. In this sense, other parameters including microcapsule size, shell composition, aggregation effects and

G3 catalyst interaction with the resin could be held responsible for such effect. Further and deeper research would be needed for this hypothesis verification.

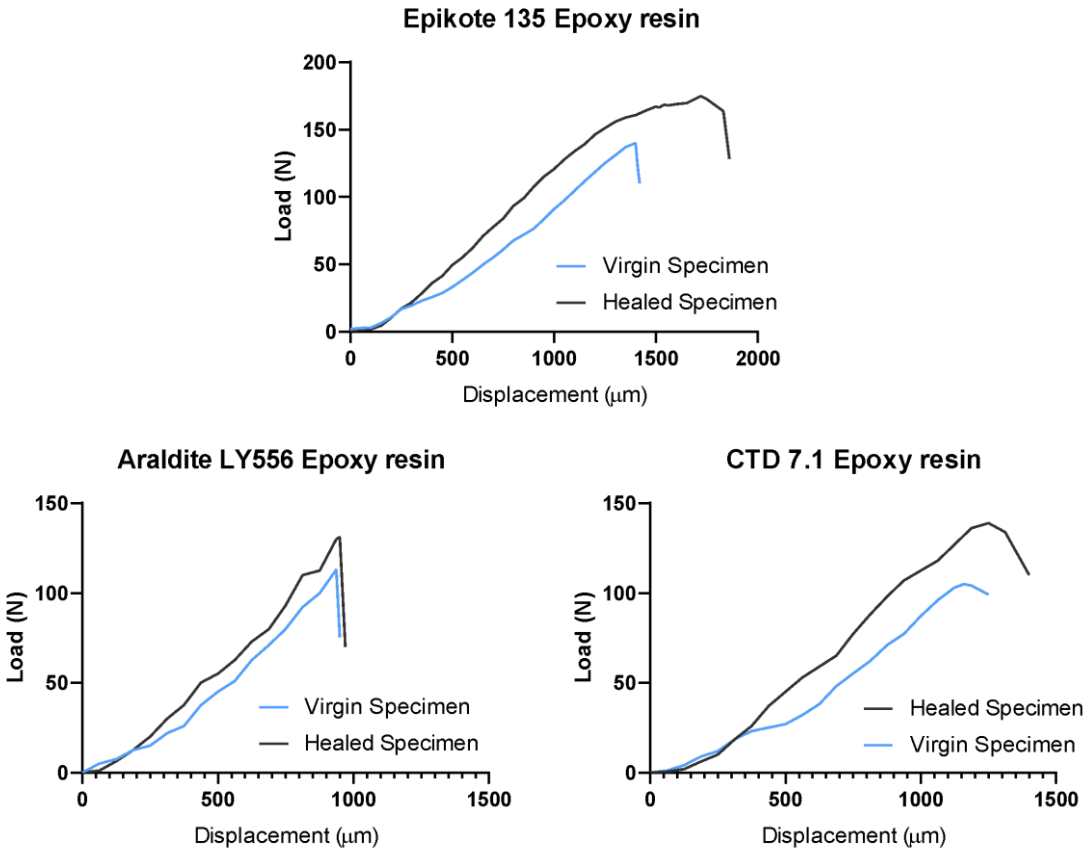

Figure 3.7. Representative force vs displacement curves of epoxy resins manufactured with ENB/DCPD microparticles. Higher values of fracture toughness are observed in the three epoxy systems after the healing process.

The SH efficiency (η_{SH}) was calculated by means of Equation 3.2, using the obtained critical fracture load of both virgin and healed sample at low/ultra-low temperatures. Regardless of initial decrease in values, fracture healing tests in SH modified Epikote 135 epoxy resin exhibited η_{SH} values of 115% at low/ultra-low temperatures.

Accounting for the excellent SH capacity obtained for the first epoxy system, one SH modified specimen of Araldite LY556 and one of CTD7.1 epoxy systems were manufactured in order to observe if these results could be extrapolated into other epoxy resin systems. SH fracture toughness results for those systems are summarized in Table 3.5.

Table 3.5. Epikote, Araldite and CTD epoxy systems Self-Healing results.

Resin	Virgin (N)	Healed (N)	% healing[a]
Epikote 135/ Epikure 137 – 10% Self-Healing additives	133.3 ± 18.9	153.2 ± 24.9	114.8 ± 9.1
Epikote 135/ Epikure 137	187.1 ± 12.3	25.3 ± 3.0	-
Araldite LY556/ Aradur 917 – 10% SHMC	109.5	127.3	116
Araldite LY556/ Aradur 917	132.5 ± 7.4	17.0 ± 2.0	-
CTD 7.1 – 10% SHMC	100	134	134
CTD 7.1	150.5 ± 16.1	20.0 ± 3.3	-

[a] 100% of SH efficiency was considered when the healed sample demonstrates the same level of critical fracture load than the virgin one.

According to the load-displacement curves (Figure 3.7), differences between fracture forces of specimens with and without SH followed the same behaviour of the first studied system, where additives appear to have caused a slight decrease in the toughness of the specimens. Similarly to Epikote modified resin, both Araldite and CTD 7.1 SH specimens demonstrated SH capacity with efficiencies of 116 % and 133 % respectively at low temperatures leading thus to a tougher material after healing in all studied systems, while no effect was observed in reference specimens. This demonstrates the versatility of the SH systems efficiency for different

epoxy resins at cryogenic conditions. The observed trend is in good agreement with those reported in previous studies.[19,26]

The authors acknowledge the simplistic yet most common approach for the SH studies that the TDCB provide in regard to other techniques studying the damage on continuum mechanics[18] that can be more representative but appears to have a higher degree in complexity that falls out of the current scope of this work.

3.3.5 Fracture surface morphology

Several fracture surfaces of different SH specimens were analysed by SEM microscopy after conducting the fracture tests (Figure 3.8). Comparing the fractured surface of the healed samples after performing the SH test to those observed in areas of the modified specimens that were not damaged, the surface morphology and microstructure are completely different in terms of surface roughness. This phenomenon is produced due to the lack of observable microcapsules in the fractured region of the self-healed specimens (Figure 3.8, b). These observations could imply that, during the fracture test, the microcapsules broke and their content effectively interacted with the catalyst, repairing the induced microcracks and thus, performing the desired and observed SH effect shown in Figure 3.7, whereas in the rest of the specimen, no damage was induced and therefore, the SH microcapsules remain intact (Figure 3.8, a). Moreover, the hypothesized specimen embrittlement due to the microcapsules addition, can be attributed to the observed, intact and marked microsphere clusters (yellow highlighted square in Figure 3.8, a). These aggregates, although having a scarce presence in the resin as observed by SEM (SI), may be generating secondary phases and non-coherent interfaces that in turn, could potentially be the reason for the decrease of toughness of the SH modified specimens in comparison with the neat

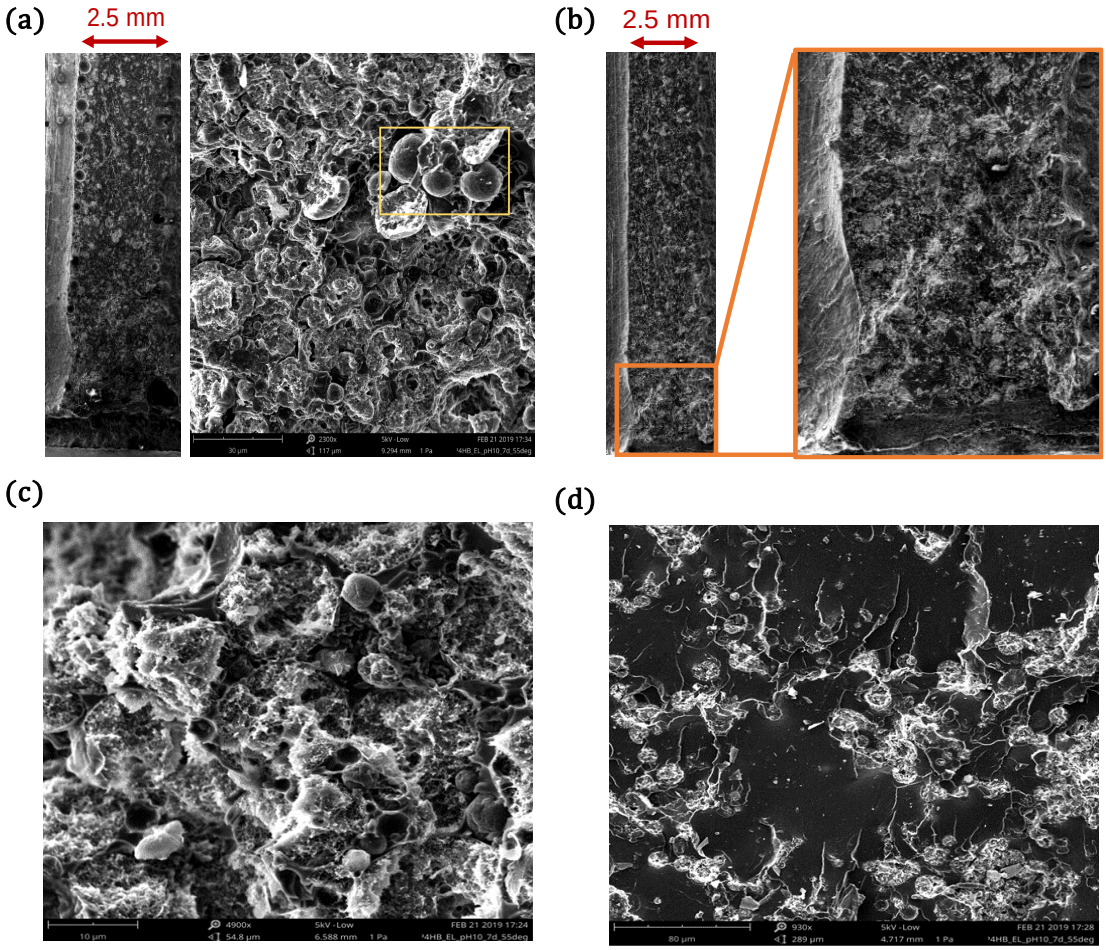

Figure 3.9. TOP- SEM micrographs of the Epikote 135 epoxy composites with SH additives. (a) non-damaged area where the capsules can be seen intact on the yellow square and (b) self-healed specimen where the surface of the specimen does not show any apparent microcapsule due to the SH effect. BOTTOM - SEM micrographs from a tested modified specimen. (c) In the fracture region, where it can be appreciated a reacted core of the microcapsules and its surroundings and (d) far from the fracture zone.

ones. Additionally, a closer inspection of a region of a tested modified specimen, exhibit the reacted SH microcapsules completely integrated in the matrix as well as a bad adhesion between the microcapsules and the resin employed in a non-damaged area of the specimens (Figure 3.8, c). These results contribute to the hypothesis that the SH additives are the main drivers for the samples embrittlement as well as confirm the release and reaction of the SH monomers at the studied temperatures. Even

though the introduction of these SH system could appear to slightly compromise the epoxy material toughness, it should not significantly affect the final composite mechanical properties when the Carbon or Glass fibre reinforcement is added. Moreover, the possible presence of small clusters inside the composite did not compromise the healing effect as shown in Figure 3.7.

3.4 Conclusions

In this work, the comprehensive study was successfully performed regarding fluidity and chemical reactivity of different ENB/DCPD mixtures, catalysts type (HG2, G3) and concentration (0.1 to 0.004%). It has been proven that the system can flow and fill the crack at ultra-low temperatures (–70 °C) and react with G3 catalyst promoting the ROMP reaction at cryogenic temperatures (–20 °C) facing composite real applications. The microencapsulation of the ENB/DCPD mixture in pMDI-based polyurea by interfacial polymerization allowed a wide range of core-shell materials with high healing agent load.

A load of 10 wt.% of SH additives was proven optimal to maintain the viscosity values within the working range given by large-scale manufacturing processes. Extrinsic self-healing system based on ENB/DCPD blend and G3 catalyst did not affect the epoxy system curing process.

The use of TDCB geometry helped in understanding the crack propagation and the fracture properties of microcapsules reinforced epoxy composites.

The developed system demonstrated SH values up to 134% at low and ultra-low temperatures. Crack surface morphology images obtained by

SEM before and after the SH process confirmed the feasibility of the breaking and curing mechanism of the extrinsic system.

Even though most of the research exhibited in this work has been done in different systems of epoxy materials, both the additives size and its concentration have been optimized for an industrial scale-up and application for FRP manufacture.

As a summary, we have developed an autonomous, extrinsic SH system that has demonstrated flowability at ultra-low temperatures (-70 °C) and a highly efficient automatic repair at cryogenic temperatures (–20 °C) without the need of catalyst protection in three different commercial epoxy resins traditionally used in fields as automotive, aeronautics and wind energy. Moreover, due to the excellent results derived from this work, little modifications can be generated to adapt the system to a broad range of polymeric materials and therefore, to an extremely wide field of applications.

3.5 Acknowledgments

We thank Dr. Lorenzo Bautista and Hector Linuesa for useful discussions. We thank Dr. Pau Nolis (Universitat Autònoma de Barcelona) for his technical assistance in NMR spectroscopy. We thank Quimidroga S.A. for providing Voranate™ M 2940. This work has received funding from the European Union's Horizon 2020 research and innovation programme under grant agreement No 685842. J.J. Roa acknowledges the Serra Hunter programme of the Generalitat de Catalunya. This work has also been done in the framework of the doctorate in Material Sciences of the Autonomous University of Barcelona.

3.6 References

1. Mugahed Amran, Y. H., Alyousef, R., Rashid, R. S. M., Alabduljabbar, H. & Hung, C.-C. Properties and applications of FRP in strengthening RC structures: A review. *Structures* **16**, 208–238 (2018).
2. Hopmann, C., Ophüls, M., Hildebrandt, M. & Fischer, K. Flexible Production of Thermoset FRP Components. *Lightweight Des. Worldw.* **11**, 54–59 (2018).
3. Patnaik, A., Satapathy, A., Chand, N., Barkoula, N. M. & Biswas, S. Solid particle erosion wear characteristics of fiber and particulate filled polymer composites: A review. *Wear* **268**, 249–263 (2010).
4. Vigneshwaran, S., Uthayakumar, M. & Arumugaprabu, V. A review on erosion studies of fiber-reinforced polymer composites. *J. Reinf. Plast. Compos.* **36**, 1019–1027 (2017).
5. Mohan, N., Mahesha, C. R. & Rajaprakash, B. M. Erosive Wear Behaviour of WC Filled Glass Epoxy Composites. *Procedia Eng.* **68**, 694–702 (2013).
6. Yang, Y. & Urban, M. W. Self-healing polymeric materials. *Chem. Soc. Rev.* **42**, 7446 (2013).
7. Leeuwenburgh, S. C. G., De Belie, N. & van der Zwaag, S. Self-Healing Materials are Coming of Age. *Adv. Mater. Interfaces* **5**, 1800736 (2018).
8. Dahlke, J., Zechel, S., Hager, M. D. & Schubert, U. S. How to Design a Self-Healing Polymer: General Concepts of Dynamic Covalent Bonds and Their Application for Intrinsic Healable Materials. *Adv. Mater. Interfaces* **5**, 1800051 (2018).

9. Zhong, N. & Post, W. Self-repair of structural and functional composites with intrinsically self-healing polymer matrices: A review. *Compos. Part Appl. Sci. Manuf.* **69**, 226–239 (2015).
10. Ullah, H., M Azizli, K. A., Man, Z. B., Ismail, M. B. C. & Khan, M. I. The Potential of Microencapsulated Self-healing Materials for Microcracks Recovery in Self-healing Composite Systems: A Review. *Polym. Rev.* **56**, 429–485 (2016).
11. An, S., Lee, M. W., Yarin, A. L. & Yoon, S. S. A review on corrosion-protective extrinsic self-healing: Comparison of microcapsule-based systems and those based on core-shell vascular networks. *Chem. Eng. J.* **344**, 206–220 (2018).
12. Wang, S. & Urban, M. W. Self-healing polymers. *Nat. Rev. Mater.* **5**, 562–583 (2020).
13. Hu, Z. *et al.* Multistimuli-Responsive Intrinsic Self-Healing Epoxy Resin Constructed by Host–Guest Interactions. *Macromolecules* **51**, 5294–5303 (2018).
14. Dong-Min Kim *et al.* Low-Temperature Self-Healing of a Microcapsule-Type Protective Coating. *Materials* **10**, 1079 (2017).
15. Hu, Z. *et al.* Efficient intrinsic self-healing epoxy acrylate formed from host-guest chemistry. *Polymer* **164**, 79–85 (2019).
16. Kumar Banshiwal, J. & Nath Tripathi, D. Self-Healing Polymer Composites for Structural Application. in *Functional Materials* (ed. Sahu, D.) (IntechOpen, 2019). doi:10.5772/intechopen.82420.
17. Cohades, A., Branfoot, C., Rae, S., Bond, I. & Michaud, V. Progress in Self-Healing Fiber-Reinforced Polymer Composites. *Adv. Mater. Interfaces* **5**, 1800177 (2018).

18. Tan, P. S., Somashekar, A. A., Casari, P. & Bhattacharyya, D. Healing efficiency characterization of self-repairing polymer composites based on damage continuum mechanics. *Compos. Struct.* **208**, 367–376 (2019).
19. White, S. R. *et al.* Autonomic healing of polymer composites. *Nature* **409**, 794–797 (2001).
20. Rule, J. D., Brown, E. N., Sottos, N. R., White, S. R. & Moore, J. S. Wax-Protected Catalyst Microspheres for Efficient Self-Healing Materials. *Adv. Mater.* **17**, 205–208 (2005).
21. Forcina, V., García-Domínguez, A. & Lloyd-Jones, G. C. Kinetics of initiation of the third generation Grubbs metathesis catalyst: convergent associative and dissociative pathways. *Faraday Discuss.* **220**, 179–195 (2019).
22. Brown, E. N., Kessler, M. R., Sottos, N. R. & White, S. R. In situ poly(urea-formaldehyde) microencapsulation of dicyclopentadiene. *J. Microencapsul.* **20**, 719–730 (2003).
23. Lee, J. K., Hong, S. J., Liu, X. & Yoon, S. H. Characterization of dicyclopentadiene and 5-ethylidene-2-norbornene as self-healing agents for polymer composite and its microcapsules. *Macromol. Res.* **12**, 478–483 (2004).
24. Noh, H. H. & Lee, J. K. Microencapsulation of self-healing agents containing a fluorescent dye. *Express Polym. Lett.* **7**, 88–94 (2013).
25. Urdl, K. *et al.* Self-healing of densely crosslinked thermoset polymers—a critical review. *Prog. Org. Coat.* **104**, 232–249 (2017).

26. Raimondo, M., Longo, P., Mariconda, A. & Guadagno, L. Healing agent for the activation of self-healing function at low temperature. *Adv. Compos. Mater.* **24**, 519–529 (2015).
27. Kalista, S. J., Pflug, J. R. & Varley, R. J. Effect of ionic content on ballistic self-healing in EMAA copolymers and ionomers. *Polym. Chem.* **4**, 4910 (2013).
28. Tiwari, N., Ho, F., Ankit, A. & Mathews, N. A rapid low temperature self-healable polymeric composite for flexible electronic devices. *J. Mater. Chem. A* **6**, 21428–21434 (2018).
29. Ying, H., Zhang, Y. & Cheng, J. Dynamic urea bond for the design of reversible and self-healing polymers. *Nat. Commun.* **5**, 3218 (2014).
30. Wu, X., Luo, R., Li, Z., Wang, J. & Yang, S. Readily self-healing polymers at subzero temperature enabled by dual cooperative crosslink strategy for smart paint. *Chem. Eng. J.* **398**, 125593 (2020).
31. Xue, S. *et al.* Self-healable poly(acrylic acid- *co* -maleic acid)/glycerol/boron nitride nanosheet composite hydrogels at low temperature with enhanced mechanical properties and water retention. *Soft Matter* **15**, 3680–3688 (2019).
32. Nevejans, S. *et al.* The challenges of obtaining mechanical strength in self-healing polymers containing dynamic covalent bonds. *Polymer* **179**, 121670 (2019).
33. Brown, E. N. Use of the tapered double-cantilever beam geometry for fracture toughness measurements and its application to the quantification of self-healing. *J. Strain Anal. Eng. Des.* **46**, 167–186 (2011).

34. Sutthasupa, S., Shiotsuki, M. & Sanda, F. Recent advances in ring-opening metathesis polymerization, and application to synthesis of functional materials. *Polym. J.* **42**, 905–915 (2010).
35. Specht, S., Bluhm, J. & Schröder, J. Continuum Mechanical Description of an Extrinsic and Autonomous Self-Healing Material Based on the Theory of Porous Media. in *Self-healing Materials* (eds. Hager, M. D., van der Zwaag, S. & Schubert, U. S.) vol. 273 143–184 (Springer International Publishing, 2015).
36. Song, K. *et al.* Highly active ruthenium metathesis catalysts enabling ring-opening metathesis polymerization of cyclopentadiene at low temperatures. *Nat. Commun.* **10**, 3860 (2019).
37. Li, Q., Siddaramaiah, Kim, N. H., Hui, D. & Lee, J. H. Effects of dual component microcapsules of resin and curing agent on the self-healing efficiency of epoxy. *Compos. Part B Eng.* **55**, 79–85 (2013).
38. Petersen, D., Link, R., Beres, W., Koul, A. & Thamburaj, R. A Tapered Double-Cantilever-Beam Specimen Designed for Constant-K Testing at Elevated Temperatures. *J. Test. Eval.* **25**, 536 (1997).
39. Kanu, N. J., Gupta, E., Vates, U. K. & Singh, G. K. Self-healing composites: A state-of-the-art review. *Compos. Part Appl. Sci. Manuf.* **121**, 474–486 (2019).
40. Garoz Gómez, D. *et al.* In-depth numerical analysis of the TDCB specimen for characterization of self-healing polymers. *Int. J. Solids Struct.* **64–65**, 145–154 (2015).
41. Sheng, X., Lee, J. K. & Kessler, M. R. Influence of cross-link density on the properties of ROMP thermosets. *Polymer* **50**, 1264–1269 (2009).

42. Yang, G., Mauldin, T. C. & Lee, J. K. Cure kinetics and physical properties of poly(dicyclopentadiene/5-ethylidene-2-norbornene) initiated by different Grubbs' catalysts. *RSC Adv.* **5**, 59120–59130 (2015).
43. Leitgeb, A., Wappel, J. & Slugovc, C. The ROMP toolbox upgraded. *Polymer* **51**, 2927–2946 (2010).
44. Huang, M. & Yang, J. Facile microencapsulation of HDI for self-healing anticorrosion coatings. *J. Mater. Chem.* **21**, 11123 (2011).
45. Salaün, F., Bedek, G., Devaux, E., Dupont, D. & Gengembre, L. Microencapsulation of a cooling agent by interfacial polymerization: Influence of the parameters of encapsulation on poly(urethane–urea) microparticles characteristics. *J. Membr. Sci.* **370**, 23–33 (2011).
46. Guadagno, L. *et al.* Self-healing epoxy nanocomposites via reversible hydrogen bonding. *Compos. Part B Eng.* **157**, 1–13 (2019).
47. Li, H., Wang, R. & Liu, W. Toughening Self-healing Epoxy Resin by Addition of Microcapsules. *Polym. Polym. Compos.* **19**, 223–226 (2011).

CHAPTER

4

SYNTHESIS OF UV-CURABLE PUA WITH ON DEMAND PROPERTIES

Materials Advances

ROYAL SOCIETY OF CHEMISTRY

PAPER

View Article Online
View Journal

Synthesis of UV-curable polyurethane-acrylate hybrids with tuneable hardness and viscoelastic properties on-demand

Guillem Romero-Sabat,[a] Luis Angel Granda [a] and Sandra Medel *[a]

[a] Leitat Technological Center, Carrer de la Innovació, 2, 08225 (Terrassa, SPAIN).

*smedel@leitat.org

https://doi.org/10.1039/d2ma00228k

Received 28th February 2022, Accepted 6th May 2022

Available online 30 May 2022

rsc.li/materials-advances

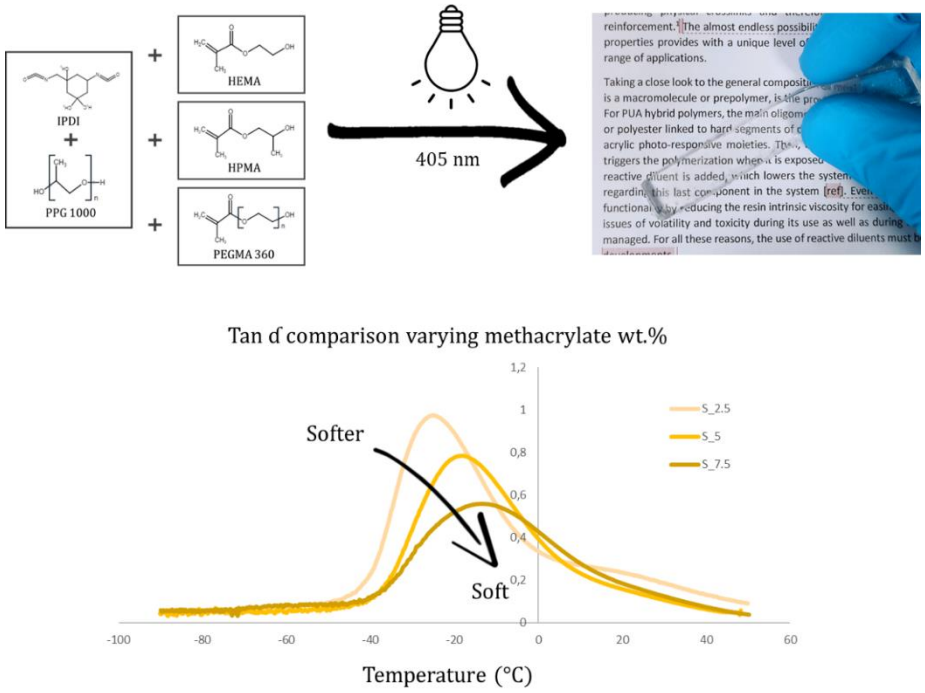

Scheme 4.1. Graphical representation of the presented work. By a careful selection of the building block types and composition, it was possible to generate a set of transparent photocuring polymers with tunable softness and viscoelastic behavior.

Abstract

Currently, there is an unmet need of possessing a deeper understanding between the chemical structure and the exhibited properties of polymers. Moreover, thanks to the development of technologies allowing an unprecedented level of personalization, researchers are aiming towards the generation of polymers tailored for specific applications. In the present work, a series of soft, transparent, and UV-photopolymerizable Polyurethane-Acrylate (PUAs) hybrids were synthesized via a two-step polymerization route, followed by a UV-curing process and maintaining two constant ratios of soft/hard segment in the polyurethane (PU)

structure as well as using three different acrylate segment types at three concentrations in the overall polymeric structure (2.5, 5 and 7.5 wt.%). The success of the synthesis procedure, the molecular weight, the transparency, the thermal behaviour, the viscoelastic response and the softness of the synthesized PUA were studied by analytical methods. Using those techniques, it was possible to quantify gradual values between the different generated materials showing up to a 50% difference in the molecular weight, variations reaching 15 °C in the thermal transition or modifications of the thermal stability of 50 °C, changes of even a 90% in the viscoelastic response and additionally, a range of hardness going from extra-soft to medium-hard. Through this work, it is possible to predict how the different variables affect some of the most relevant properties of the synthesized materials and therefore select the most suitable for each specific application. These results are expected to guide further developments on materials in applications ranging from UV-curable coatings to in situ 3D-printing for biomedical applications.

Keywords: Polyurethane; Acrylate; Photocurable; Thermal stability; Dynamic Mechanical Analysis; Soft Polymers;

4.1 Introduction

The transition from solvent-containing, toxic and slow reactive 2k formulations to 1k UV-curing systems made a significant impact in improving the fields of protective coatings,[1] automotive, dental industry,[2] or photolithography among others.[3] Moreover, the addition of Polyurethanes (PU) to the typically acrylic single-component formulations to synthesize Polyurethane-Acrylate hybrids (PUA) allowed a gain in mechanical properties, adhesion and weather resistance while keeping the good properties of these light-curable materials.[4] Most of the interesting properties of these PUA polymers come from the PU's molecular backbone composed of different blocks of soft polyether or polyester bonded by polycondensation reactions to hard segments of diisocyanates. While soft segments account for the elastic behaviour, urethane groups are the main responsible for increasing the rigidity due to their high hydrogen bond content.[5] The almost endless possibilities of modifying the polymer's structure and final properties provides with a unique level of versatility, thus being possible to adapt them into a wide range of applications.

Taking a close look at the general composition of most UV-curable systems, the oligomer, which is a macromolecule or prepolymer, is the provider of the major properties of the end-product.[6,7] Concretely for PUA hybrid polymers, the main oligomers are based on a PU structure but ended in both extremes of the chain by acrylic photo-responsive moieties. Then, a light sensitive molecule called the photoinitiator, triggers the polymerization when it is exposed to certain wavelengths of UV light, and finally, a reactive diluent is added, which lowers the system's viscosity. There are, however, concerns regarding this last component in the system.[8] Even though the reactive dilutant reduces the

system's intrinsic viscosity and thus eases its use into certain applications, issues of volatility and toxicity during its manipulation as well as during transport and storage must be managed. For all these reasons, the use of reactive diluents must be carefully studied in further developments of photocurable polymer systems.

One of the fields of application with higher potential for photocurable resins lies within Additive Manufacturing (AM) technologies. AM, also known as 3D printing, has caused a revolution in designing and producing objects with complex geometries by building them layer by layer.[9] Among the different AM techniques, photocuring 3D technologies, known as vat photopolymerization techniques (VAT), are still the most relevant in terms of speed, cost, and printing resolution.[9] Within VAT AM, photocurable Direct-Ink-Write (DIW), thanks to extruding the materials to the photocuring area, has been proposed to introduce novel materials unable by conventional techniques (i.e. limited by high viscosities).[10] Moreover, the current possibility of generating data from imaging technologies (i.e., from Nuclear Magnetic Resonance (NMR) or tomography), allows the fabrication of complex personalized models, of great value for great range of medical applications.[11,12] However, to achieve successful results working with those techniques, materials with specific characteristics as well as sensitive to light stimulus must be designed. Up to now, most uses of photocuring 3D printing techniques are focused on temporary replacement materials due to the limited performance and brittleness of the nowadays used UV-curing resins. Additionally, the current commercially available elastomeric resins, apart from being mostly opaques and therefore not applicable in fields where high transparency is required, do not provide the users the possibility of modifying the resin composition and thus, its properties.[13,14] A challenging but potentially high-rewarding area, lies within the

manufacture of customizable elastomeric materials capable of complementing the current available ones for rapid prototyping AM, widening the material's portfolio and thus, accelerating the inclusion of this technology into more fields.[15] However, to achieve such goal, it is imperative to obtain first a deep enough understanding of the structure-properties relationship in the materials as a way of creating specifically and optimally synthesized polymers tailored for each desired application.[6]

Beyond the attempts to replicate some organ-like structures, to generate artificial replacements, there has been recently an interest in obtaining relevant models for testing and practicing medical procedures aiming to increase the ratio of success and decrease unexpected complications. Thanks to non-invasive techniques, doctors are already capable of looking through the human body to find alterations of the homeostasis and analysing the general tissue behaviour before an intervention. The potential generation of those images as 3D models would gear up the preoperational readiness and greatly diminish the potential associated risks. Nonetheless, to truly generate a positive impact, those models should mimic as precisely as possible the behaviour of the targeted organs. As an outline, the generation of highly tuneable materials can become a huge step forward in the successful production of those truly realistic surgical models.

In the past years, there have been studies directed specifically towards enlightening the potential relationships between molecular structures of the synthesized PUA systems and the properties those materials presented. Early studies aimed to understand, among others, the thermal,[16,17] mechanical[18] or viscoelastic[19] behavioural changes generated in basic PU systems by using different kinds of isocyanates,[20,21] chain

extenders[22] or polyol types[23] as well as the proportion between them.[24] For PUA hybrids, similar but more recent studies regarding thermal stability[25], mechanical properties,[25] microphase separation,[26] transparency[14] or biocompatibility[27,28] have been pursued. However, they are mostly focused on the effect of polyol and diisocyanate due to the relative broad spectrum of possibilities they provide. With all, very few literature report about the influence of the acrylic component in the final polymer properties.[29]

In this work, we have been able to synthesize soft, photocurable, transparent, diluent and filler-free PUA hybrid polymer aiming to provide a thorough structure-properties relationship study on the effect of different UV-reactive biocompatible acrylate moieties such as 2-hydroxyethyl methacrylate (HEMA), 2-hydroxypropyl methacrylate (HPMA) and poly(ethylene-glycol) methacrylate (PEGMA) as well as the different soft/hard microstructure ratios. Simultaneously, a methodology has been provided to finely tune the photocurable polymer's properties thus broadening the library of elastomeric materials potentially suitable for UV-curing technologies and potentially easing the adoption of soft polymers for tissue-replicating models. Additionally, the effectiveness of their sterilization was also studied to demonstrate their applicability for preoperative strategic planning as surgical model materials.

4.2 Experimental

4.2.1 Materials

Isophorone diisocyanate (IPDI), 1,4-butanediol (BDO), tetrahydrofuran (THF) (all materials were reagent grade with a purity of ≥99.0% and contained 250 ppm BHT as inhibitor), dibutyltin dilaurate (DBTDL) and

phenylbis(2,4,6-trimethylbenzoyl)phosphine oxide (PBO) were purchased from Sigma and used without further purification. Poly(propylenglycol) (PPG, M_n = 1000 g mol^{-1}), 2-hydroxyethyl methacrylate (HEMA), 2-hydroxypropyl methacrylate (HPMA), poly(ethyleneglycol) methacrylate (PEGMA, M_n = 360 g mol^{-1}, containing 500-800 ppm MEHQ as inhibitor) were purchased from Sigma and placed under vacuum at 60 °C for 2 h prior to use to ensure the removal of unwanted moisture.

4.2.2 Characterization methods.

Fourier transform infrared-attenuated total reflectance (FTIR-ATR). The infrared spectra were obtained by using an IR Affinity-1S CE FTIR spectrophotometer (Shimadzu, Japan) in the 4000-500 cm^{-1} range and with a 1 cm^{-1} resolution (32 scans collected).

Nuclear Magnetic Resonance (NMR). ^{1}H-NMR and ^{13}C-NMR spectra were acquired in a Bruker Avance-II+ 400 MHz. NMR spectra of the different polymer samples prior to being UV-cured were obtained in deuterated chloroform ($CDCl_3$) at room temperature. Chemical shifts were assigned using the residual undeuterated solvent signal as an internal reference.

Gel Permeation Chromatography (GPC). Molecular weight of the polymer samples was studied through an Ultra High Performing Liquid Chromatograph model 1260 (Agilent, US), using a PLgel 10 µm MIXED-B 300 x 7.5 column and using THF as the mobile phase at 40 °C. The equipment calibration was done with a series of PolyMethyl Methacrylate (PMMA) patrons with molecular weights from 880 to 1577000 Da.

Thermogravimetric Analysis (TGA). TGA was carried out with a Q500 thermobalance (TA Instruments, US). 5 to 10 mg of PUA samples were heated from 25 °C to 700 °C at a 10 °C min^{-1} heating rate performed in an

inert atmosphere of nitrogen (40.0 mL min^{-1}). The weight loss was recorded as a function of temperature. Values of $T_{5\%}$ were taken at the temperature that the sample's weight loss represented a 5 wt.%. T_{max} was obtained from the peak of the first derivative of the weight-loss/time curve.

Differential Scanning Calorimetry (DSC). A DSC analysis of each UV-cured polymer specimen was executed in a Q20 DSC instrument connected to a cooling system (TA Instruments, US) using between 3 and 5 mg of sample in an Aluminium pan. A heat-cool-heat analysis was performed from 25 °C to 200 °C at 10 °C min^{-1} followed by a cooling ramp to -80 °C at 5 °C min^{-1} and finally, heating again to 200 °C at 10 °C min^{-1} performed in an inert atmosphere of nitrogen (40.0 mL min^{-1}). Glass transition temperature (T_g) values and the width of the transition were obtained from the slope change in the second heating run cycle.

UV-Vis transmittance. The optical transmittance was studied in thick specimens of 4 mm using an UV-2450 UV-visible spectrophotometer (Shimadzu, JP) at the wavelength range of 400 to 800 nm. As mentioned in previous studies,[30] it is important to acknowledge that higher transmittance levels could be achieved as, due to the measurement procedure in solid samples, there are two interfaces where the light is reflected: on entering the sample, and on leaving. This effect is related to the differences between refractive indices between the samples and air.

Dynamic Mechanical Assay (DMA). DMA was carried out in a SDTA861 dynamomechanic equipment (Mettler Toledo). Rectangular specimens of 20x5x2 mm^3 were cut from UV cured films of 10*80*2 mm^3 and the viscoelastic response and glass transition temperature (T_g) were evaluated by assessing each sample's storage modulus (E') and tangent delta (tan d) as a function of temperature (from -90 °C to 50 °C in a 3 °C min^{-1} ramp) under oscillating stress at a defined frequency (1 Hz). While

the E' is proportional to the material's stiffness and is related to the stored energy level, the tan d value is an indicative of the material's capacity for energy dissipation when changes in the physical properties are applied and plainly translates into quantifying how good the material will be at absorbing energy.

Shore 00 hardness. Hardness of each UV-cured specimen was quantified following ASTM D2240 while using a manual 53505/00 shore durometer (Baxlo, Barcelona, SP). For each measurement, 5 replicates were performed in different locations of each specimen. The obtained results are expressed in Shore Units (SU) ranked from 0 to 100, being 0 the softest and 100 the hardest.

4.2.3 Synthesis of PUA hybrids

Polymerization reactions were conducted in a five-neck, 250 mL, round-bottom glass reactor equipped with an overhead anchor-type mechanical stirrer, a water-cooled condenser, a temperature probe and an Argon inlet. All the PUA hybrids were synthesized through an adapted two step polymerization procedure as follows: First, the PU prepolymers were prepared by adding together 50 mL of THF with the calculated molar amount of PPG and heating them at 60 °C while stirring at 260 rpm for 1 h under Argon atmosphere. Once the temperature was reached, the required quantity of IPDI and three drops of the catalyst (DBTDL) were introduced and the mix was left to react for 2 h at 60 °C. Secondly, half of the stochiometric quantity of chain extender (BDO) was added slowly and left to react for 1 h. In parallel, 1 wt.% of photoinitiator (PBO) was dissolved with magnetic stirring in the specified methacrylate (MA) monomer content in the dark. The acrylic mixture was then incorporated into the reactor while stirring at 200 rpm and kept at 60 °C until no

further decrease in the NCO peak at 2272 cm^{-1} was observed by FTIR-ATR spectroscopy. Finally, the remaining half of the stochiometric molar quantity of BDO was added until complete disappearance of the NCO peak. A final drying process is carried out to remove the solvent from the synthesised product prior to storage it.

As an example for "H_HEMA5" sample (Table 4.1), 82 mmol of PPG1000 were heated and stirred with 50 mL of THF before adding 180 mmol of IPDI for reaction, thus producing the prepolymer. After completion of the prepolymer, 40 mmol of BDO were added to the prepolymer mixture and left to react. Then, 50 mmol of HEMA (or 50 mmol of HPMA or 30 mmol of PEGMA) were added. Finally, another 40 mmol of BDO were used to finish the polymerization. The crude product was collected and the solvent was removed at 30 ºC under high vacuum for 12 h obtaining the corresponding PUA hybrid as a transparent fluid.

^{1}H NMR (400 MHz, $CDCl_3$) δ ppm: 6.10 (s, 1H, H_2C=C-), 5.57 (s, 1H, H_2C=C-), 4.88 (br s, 2H$_{HPMA}$, -O-$\underline{CH_2}$-CH-), 4.80 (br s, 1H$_{HPMA}$, -O-CH_2-$\underline{CH}$-), 4.07 (br s, 2H$_{HPMA}$, -O-$\underline{CH_2}$-CH-), 3.85-3.25 (m, 2H$_{PPG}$, -CH_2-, 1H$_{PPG}$, -CH-, 4H$_{BDO}$, -CH_2-$\underline{CH_2}$-O), 2.90 (br s, 2H$_{IPDI}$, -$\underline{CH_2}$-NH), 1.94 (s, 3H$_{HPMA}$, -CH_3), 1.80-1.60 (m, 4H$_{BDO}$, -$\underline{CH_2}$-CH_2-O, 4H$_{IPDI}$, -CH_2-), 1.45-0.75 (m, 2H$_{IPDI}$, -CH_2-, 3H$_{PPG}$, -CH_3, 3H$_{HPMA}$, -CH_3, 6H$_{IPDI}$, -CH_3).

^{13}C NMR (100 MHz, $CDCl_3$) δ ppm: 167.3 (O$\underline{C}$O$_{HPMA}$), 156.7 (N$\underline{C}$O$_{IPDI}$), 155.5 (N$\underline{C}$O$_{IPDI}$), 136.1 (H_2C=$\underline{C}$-$_{HPMA}$), 126.1 ($H_2\underline{C}$=C-$_{HPMA}$), 76.0-71.5 (-$\underline{C}$H-CH_2-$_{PPG}$, -CH-$\underline{C}H_2$-$_{PPG}$, CH_2-$\underline{C}H_2$-O-$_{BDO}$), 70.0-62.0 (-$\underline{C}H_2$-$_{HPMA}$, -$\underline{C}$H-$_{HPMA}$), 55.0 (-$\underline{C}H_2$-NH-$_{IPDI}$), 47.2-23.3 (-$\underline{C}H_2$-$_{IPDI}$, (-$\underline{C}$-$_{IPDI}$, $\underline{C}H_2$-CH_2-O-$_{BDO}$), 18.4 (-$\underline{C}H_3$ $_{HPMA}$), 17.6-17.0 (-$\underline{C}H_3$ $_{PPG}$, -$\underline{C}H_3$ $_{IPDI}$).

Signal assignments were done with the aid of HSQC experiment.

4.2.4 Specimen preparation

Polymer specimens of 10x80x2 mm^3 were prepared by filling a Teflon mold with the uncured PUA hybrid to remove the residual THF in a vacuum oven at 30 °C with a tinted screen until no bubbles appeared. Then, the mold was covered with a glass slide to avoid the presence of oxygen during the photopolymerization process, and the sample was placed in a UV Form Cure (Formlabs) and irradiated for 5 min at 405 nm at room temperature while rotating at 1 rpm to ensure a fully cured sample.

4.3 Results and discussion

4.3.1 Synthesis of PUA hybrids

Within the synthesis process, IPDI was selected as the diisocyanate monomer due to its reported lower toxicity and higher biosafety than its aromatic counterparts.[31] Moreover, due to its asymmetric structure, each isocyanate group follow a different reaction kinetics and thus it is possible to generate a more accurate synthesis process. From the wide range of potential polyol molecules, PPG was selected due to their asymmetric methylene group that prevents from potential crystallization processes, thus enhancing the transparency and also, providing an overall improved material softness.[32] THF was selected as the synthesis solvent due to having a minor hazardous impact than other potential options (i.e., DMF or DMSO) while offering a good temperature reaction as well as having the capability of maintaining the polyurethane pre-polymer in solution with higher molecular weights than other solvents.[33]

Finally, the 3 different acrylic monomers were selected due to presenting differences only in the chain length of the main structure between the

acrylate and hydroxyl moieties, thus providing the single key variable of chain length to the overall process.

In this methodology, polyurethane prepolymer was first synthesized with an excess of isocyanate end-groups to provide potential anchoring points for the successful incorporation of the following acrylic monomers (Figure 4.1). The main adaptation produced to this well-known method,[4] was the addition of the chain extender monomer (BDO) that was incorporated in two different feedings. The first feeding was introduced before the acrylate monomer while the second one was the final step of the synthesis.

The changes in the feeding procedure aimed to lower the pre-polymer's intrinsic viscosity thus allowing a homogeneous distribution of the acrylic monomer in the overall polymer attempting to improve the polymer's fluidity prior to being UV-cured as well as generate a narrower molecular weight distribution. The molecule responsible for activating the UV-curing process (PBO) was dispersed in the last BDO feeding prior to finish the synthesis to obtain a homogeneous solution without compromising its stability and avoiding any unintentional photopolymerization.

Thanks to the acrylic groups at the end of each PU oligomer and the photoinitiator, it was possible to generate a soft thermoset elastomer when placed under UV-light for a few seconds by crosslinking the different PUA oligomers through radical polymerization. The overall process different PUA oligomers through radical polymerization. The overall process of PUA synthesis can be observed in Figure 4.1. Even though the acrylate composition-properties relationship is pivotal in this study, the selection of two different base PU pre-polymers with varying softness (65:35; 80:20) were introduced aiming to investigate the potential changes in the polymer's characteristics with the same

crosslinking densities from the acrylate moieties, thus researching about which variable holds a higher impact in the properties within the polymer.

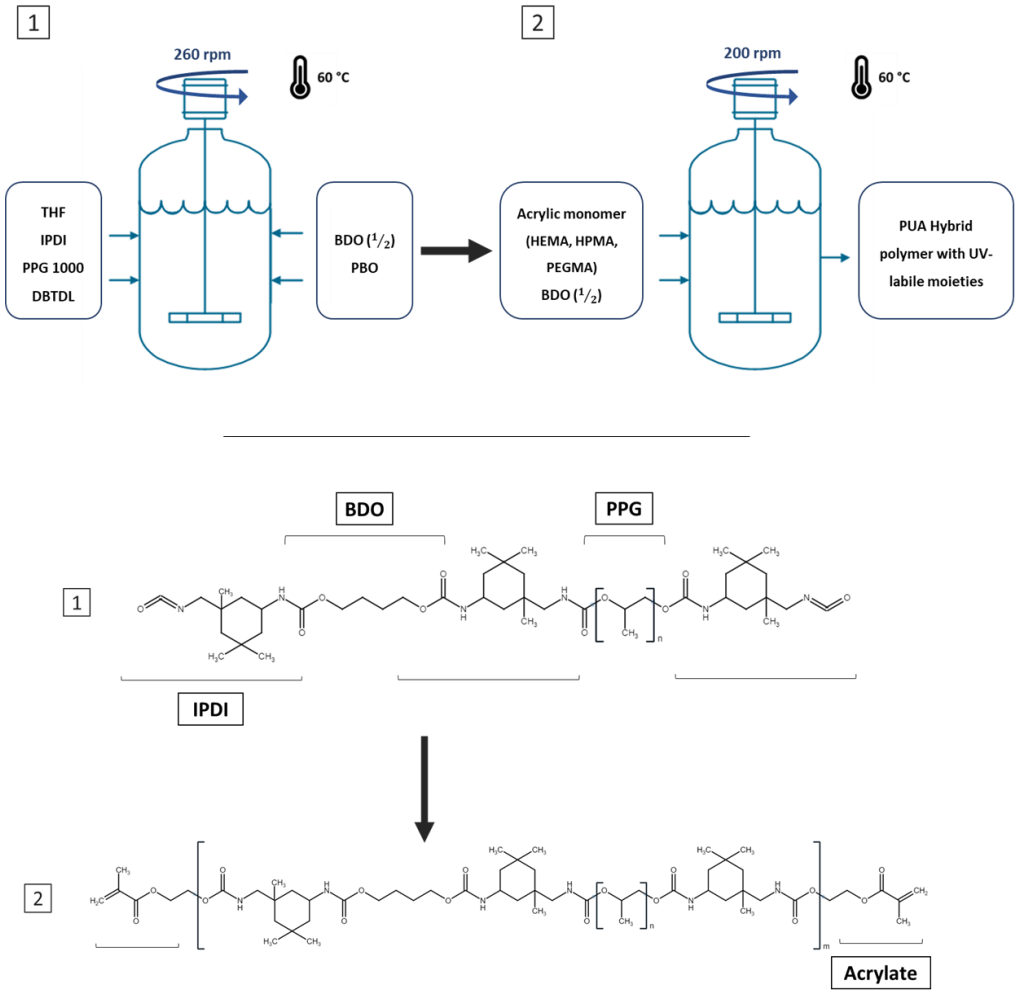

Figure 4.1. TOP. Schematic overview of the synthesis process of the Polyurethane-Acrylate Hybrids (PUAs). The polymers were synthesized in a batch process at 60 °C, with mechanical stirring and under Argon atmosphere. BOTTOM. Diagram of the theoretical molecular structure obtained in each synthesis step. An NCO-terminated oligomer is obtained in the first step while a larger molecule with acrylic end-groups is obtained at the end of the synthesis process. Molecules containing terminal hydroxyl groups are found in the middle of the oligomer structure, linked to IPDI molecules. A variable number of oligomer structures obtained in process 1 can be found within structure 2.

Table 4.1. Soft/hard ratios (relating to NCO/OH feed) and the composition of the PUA hybrids, including the acrylate type and its concentration in each sample. Moreover, the average Molecular weight obtained by Gel Permeation Chromatography (GPC) and the polydispersity of each sample is shown.

Sample	Soft/Hard ratio	Acrylate type	Acrylate wt.%	Average Molecular Weight (M_w), (g mol^{-1})	Polydispersity index (PDI)
H_HEMA2.5	65:35	HEMA	2.5	26190	2.03
H_HEMA5			5	15600	1.92
H_HEMA7.5			7.5	8972	2.44
H_HPMA2.5		HPMA	2.5	24667	2.04
H_HPMA5			5	17192	2.02
H_HPMA7.5			7.5	13552	1.89
H_PEGMA2.5		PEGMA 360	2.5	28400	2.25
H_PEGMA5			5	16545	2.11
H_PEGMA7.5			7.5	10964	1.77
S_HEMA2.5	80:20	HEMA	2.5	20761	2.38
S_HEMA5			5	17488	2.01
S_HEMA7.5			7.5	10225	1.81
S_HPMA2.5		HPMA	2.5	33260	2.01
S_HPMA5			5	*	*
S_HPMA7.5			7.5	22432	1.95
S_PEGMA2.5		PEGMA 360	2.5	41125	2.04
S_PEGMA5			5	38210	2.04
S_PEGMA7.5			7.5	*	*

* Not determined due to gelation of the polymerization mixtures

Progress of reactions were monitored by FTIR-ATR spectroscopy to observe the changes in the molecular structure of the PUA hybrids during their polymerization and to confirm the successful syntheses of the prepared hybrids. The decrease of the characteristic NCO stretching peak at 2272 cm^{-1} could be clearly seen as more components with hydroxyl moieties were added to the growing polymer. The complete absence of isocyanate groups was assured by the disappearance of that peak, which

indicates the reaction completion. Representative FTIR-ATR spectra are shown in Figure 4.2 for sample S_HPMA5 (before and after UV-curing).

The appearance of the characteristic PU peaks, such as the stretching vibrations of NH at 3380 cm^{-1}, the stretching vibrations of C=O of carbonyl groups at 1734 cm^{-1}, the bending vibrations of N-H at 1644 cm^{-1} , the peaks at 1350 and 1250 cm^{-1} associated with the stretching of C-N bond and the C-O-C vibrations respectively, indicates the presence of the ester linkage confirming thus the polyurethane formation.[34,35]

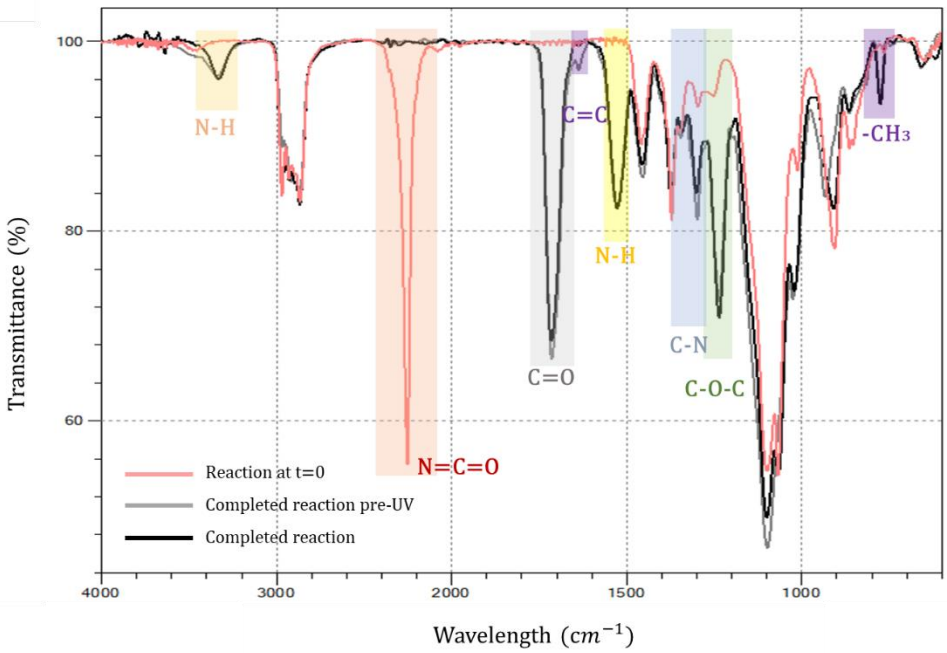

Figure 4.2. FT-IR spectrum of the sample S_HPMA_5 reaction at time 0 (red) and once the reaction was considered as finished (black). It is possible to observe the complete disappearance of the NCO peak at 2272 cm^{-1} while peaks from the PUA structure appear at 3380, 1734, 1644, 1250 and 815 cm^{-1} demonstrating thus the complete polymer synthesis.

Moreover, the appearance of a peak at around 1644 cm^{-1} in the spectra before the UV-curing, which corresponds to the stretching of the C=C bonds, indicates that the methacrylate groups have been successfully incorporated into the polyurethane chains. The further disappearance of

that peak in the spectra after UV-curing and the apparition of a peak at 815 cm^{-1} related to the methylene group in the methacrylate molecule confirms the UV-crosslinking procedure. After irradiation by UV, it can be observed that the peak frequency bands assigned to disordered hydrogen-bonding carbonyl groups are narrower and weaker than before irradiation, while the frequency bands assigned to ordered hydrogen-bonded carbonyl groups are broadened thus indicating a higher degree of hydrogen bonding (Figure 4.3). [36]

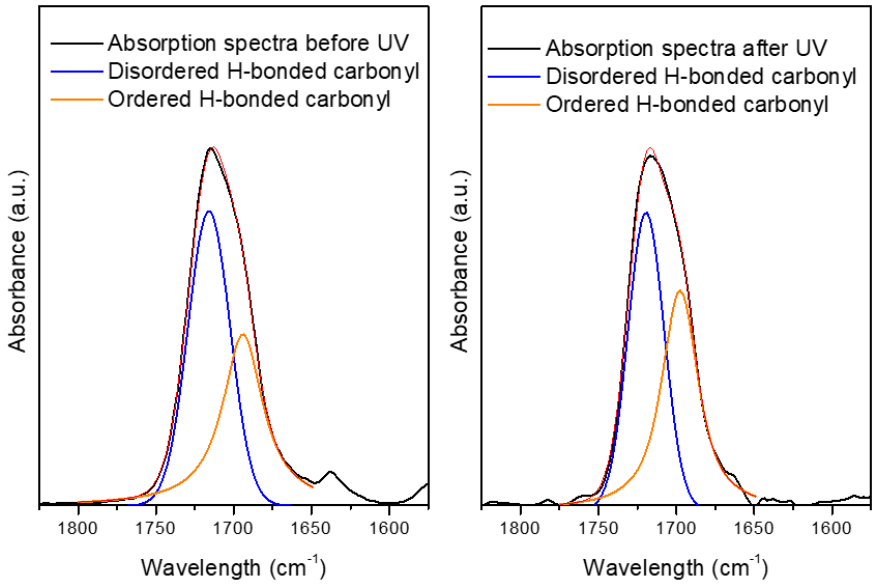

Figure 4.3 FT-IR spectrum of sample S_HPMA5 before and after UV irradiation in 1800-1600 cm-1 region fitted by Gauss-Lorentz curves.

The chemical structure of the synthesized PUA hybrids was also analyzed by ^{1}H NMR and ^{13}C NMR in $CDCl_3$. As an example, Figure 4.4 shows the ^{1}H NMR spectrum corresponding to sample H_HPMA5. The assignation of peaks is also remarked and fully confirm the chemical structure of the PUA hybrid. The peaks in the range of 4.88-4.07 ppm are $-CH_2-CH-$ protons of HPMA and appear at lower chemical shift than the free monomer. These peaks shift to lower field confirms that the acrylic monomer is attached to the OCO group of urethane nitrogen atom of

IPDI. Moreover, the existence of acrylic groups (-H_2C=C-) is clearly observed by the characteristic peaks at 6.10 and 5.57 ppm, which is crucial to carry out the subsequent UV-curing of the polymer.

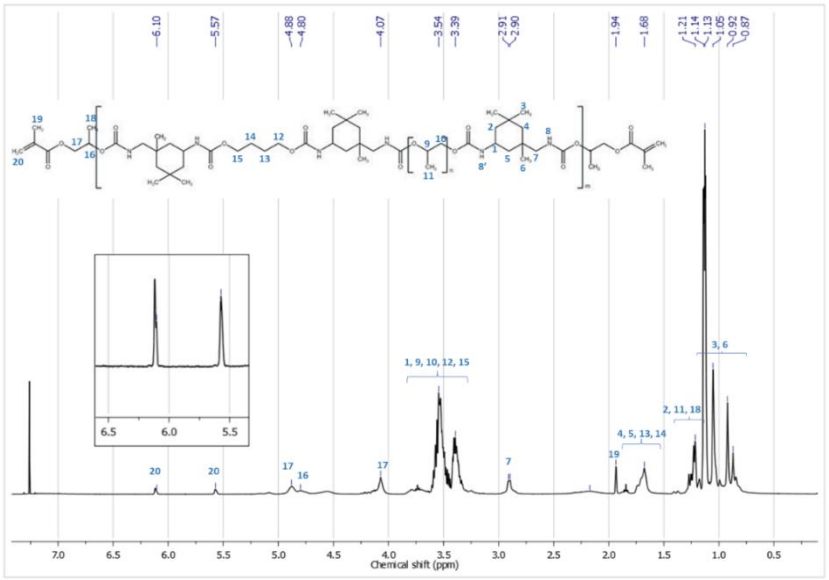

Figure 4.4. ^{1}H NMR ($CDCl_3$) spectrum of sample H_HPMA5

The GPC analysis of the synthesized polymers showed a single peak with gaussian symmetry around the highest point and a medium width distribution. Table 4.1 summarizes the GPC results of the PUA hybrids with varying contents of methacrylate monomers.

All the obtained values were found between 10000 and 40000 g mol^{-1}. It can be observed in Table 4.1 that for any of the three methacrylate monomers under study, the M_w decreases with the concentration of methacrylate monomer. This effect can be attributed to the monofunctional methacrylate monomer acting as chain stopper of the linear PU. As expected, by increasing the content of methacrylate monomer, the PU yields chain ends lacking functional groups and therefore the polycondensation process terminates earlier, leading thus to lower M_w polymers.[37]

The increased content of PPG monomer in the initial steps of the synthesis for softer PUA samples led to a higher prepolymer molecular weight and therefore, an increment in the final polymer's molecular weight.

Comparing harder polymers with equal acrylic wt.%, those containing HEMA exhibited lower M_w than with HPMA or PEGMA. Additionally, focusing on the differences between the softer and harder synthesized polymers, HPMA and PEGMA soft samples exhibit an overall higher average M_w over their harder counterparts. These results can be translated into HPMA and PEGMA monomers having a lower reactivity compared with HEMA, thus allowing the step-growth polymerization process for longer times.

The authors hypothesize that the decreased reactivity for PEGMA and HPMA monomers and the overall higher M_w of the synthesized polymers is related to steric hinderances generated by the increased volume of the monomer particles compared to HEMA. The increase for the HEMA to successfully find the free isocyanate group could produce a general decrease of the prepolymer molecular weight, explaining thus the obtained results.

4.3.2 Transparency

Optical transparency is a desirable property for most materials and utmost necessary in some applications.[14,38] The transparency degree was measured by determining the light transmittance in 4 mm thick samples obtained by photocuring the UV-susceptible methacrylic end-groups from the synthesized flowable polymer. This procedure was performed for all the synthesized specimens. Figure 4.5 (upper) depicts three

representative transmittance results in samples exhibiting the higher and lower limits obtained after irradiating from 400 to 750 nm. As observed, the measured samples exhibit good transparency levels and can be easily used as see-through materials (Figure 4.5, bottom). Among the different PUA, HPMA-based formulations appear to exhibit higher transparency levels than their counterparts achieving transmittance values up to 85% throughout the overall wavelength range.

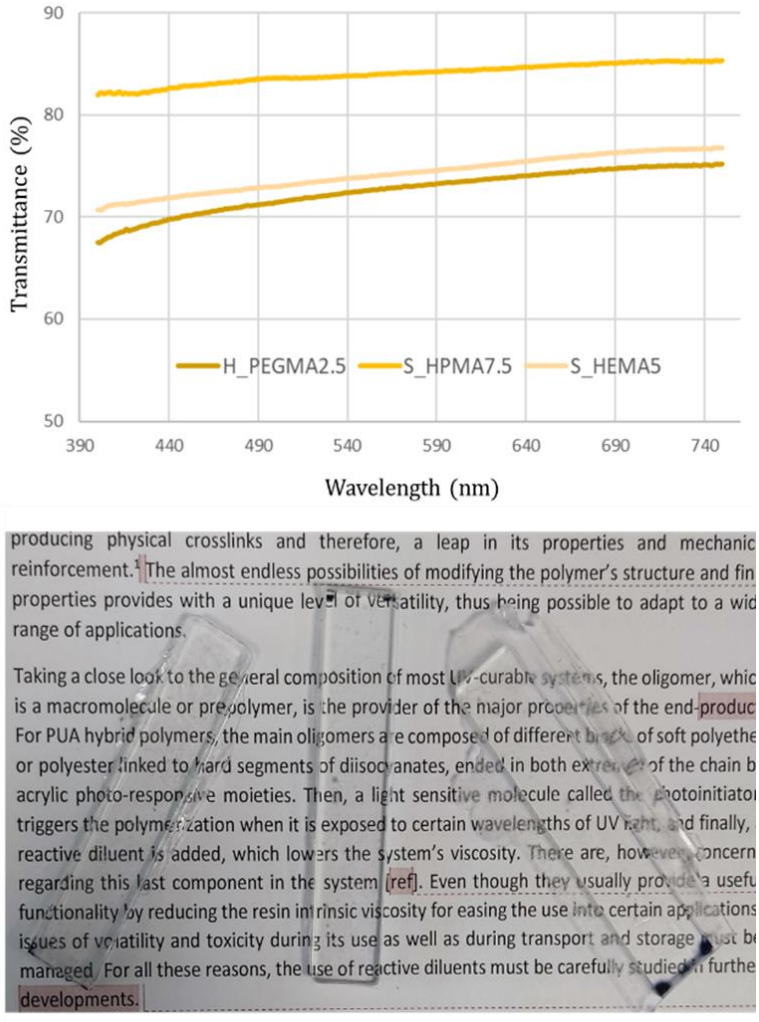

Figure 4.5. Up, optical transparency at from 750 to 400 nm with three different acrylic types, concentration, and soft/hard ratio. Bottom, representative picture of the transparency of different 4 mm thick HEMA, HPMA and PEGMA specimens.

4.3.3 Thermal properties

Table 4.2. Summary of the synthesized polymer's thermal properties. For each material is shown its Glass temperature (T_g) as well as the transition onsets (Ti and Tf) and overall increment (ΔT). Moreover, 5% weight loss ($T_{5\%}$) as well as the samples maximum degradation temperature (T_{max}) are shown.

Sample	T_g (ºC)	T_i (ºC)	T_f (ºC)	ΔT (°C)	$T_{5\%}$	T_{max}
H_HEMA2.5	-38.44	-42.33	-34.05	8.28	236,04	328
H_HEMA5	-27.29	-35.42	-13.53	21.89	263,75	336
H_HEMA7.5	-27.40	-36.57	-12.26	24.31	271,71	335
H_HPMA2.5	-28.33	-37.06	-13.73	23,33	256,57	338
H_HPMA5	-25.07	-33.82	-11.37	22,45	268,52	337
H_HPMA7.5	-25.49	-38.08	-26.93	11.15	282.40	343
H_PEGMA2.5	-30.81	-38.58	-17.24	21.34	264.90	321
H_PEGMA5	-29.73	-37.61	-13.68	23,93	258.09	349
H_PEGMA7.5	-27.71	-38.32	-12.35	25,97	269.12	342
S_HEMA2.5	-37.32	-42.57	-33.84	8.73	272.32	328
S_HEMA5	-35.94	-39.74	-29.57	10.17	276.38	336
S_HEMA7.5	-27.19	-41.12	-29.66	11.46	275.32	338
S_HPMA2.5	-36.21	-41.56	-33.52	8.04	258.29	339
S_HPMA5	-34,82	-43,10	-25.04	18,47	277.03	335
S_HPMA7.5	-27.49	-36.26	-10.73	25.53	273.75	349
S_PEGMA2.5	-38.42	-42.30	-34.76	7.54	257.43	352
S_PEGMA5	-37.26	-43.61	-34.64	8.97	259,35	358
S_PEGMA7.5	-35.89	-42.63	-32.25	10.35	261.76	349

Aiming to assess the differences in thermal behaviour, all the photocured samples were subjected to a cycle of heating to erase the material's thermal history, followed by a cooling, and reheating ramps. The glass transition temperature (T_g) as well as the width of the transition (ΔT) are shown in Table 4.2. The single T_g observed in all samples indicate a lack of separation between soft and hard domains within the PU structure.

Moreover, the absence of any crystallization indicates that the synthesized polymers are completely amorphous. Figure 4.6 shows the

absence of melting peaks for hard segments, as demonstrated by previous works when the hard segment content is lower than 23-35%.[39]

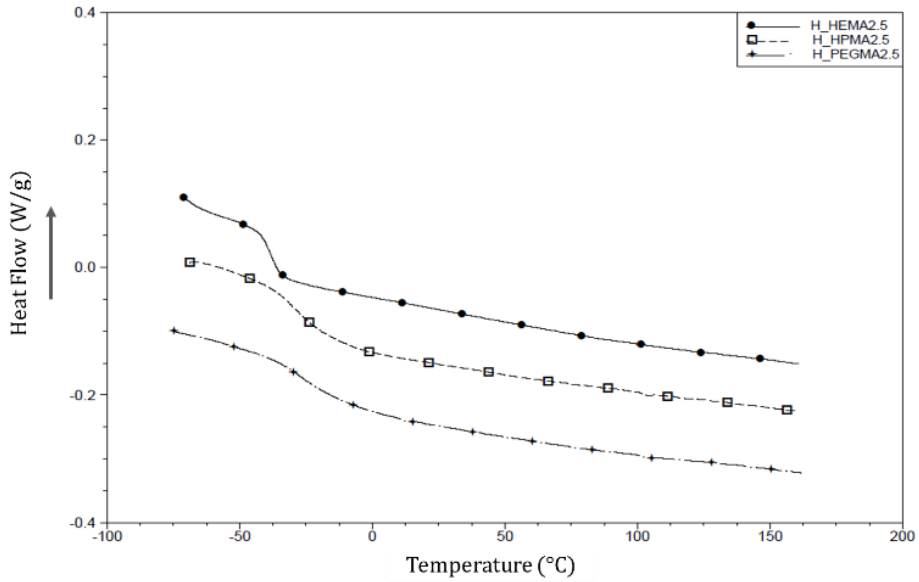

Figure 4.6 DSC curves of the 2nd heating of hard photocured samples at 2.5 acrylate wt.%.

Accounting only for the acrylate wt.% change, it is possible to observe that there is a trend pointing towards the increment of the T_g when there is a higher presence of acrylic moieties in the polymer structure, increasing up to 10 °C between the less and more crosslinked specimens (2.5 to 7.5 wt.%) (Figure 4.7). Additionally, the transition temperature width (Table 4.2) appears to broaden when the acrylic wt.% is increased. The observed direct relationship between the simultaneous increase of crosslinking points and the T_g value due to mobility restrictions is already well known and has been described extensively.[17]

Comparing samples with the same acrylate wt.% but varying its type, HPMA-based samples appear to have a higher T_g, followed by those containing HEMA and finally, PEGMA polymers exhibit generally the transition at the lowest temperature (Figure 4.7).

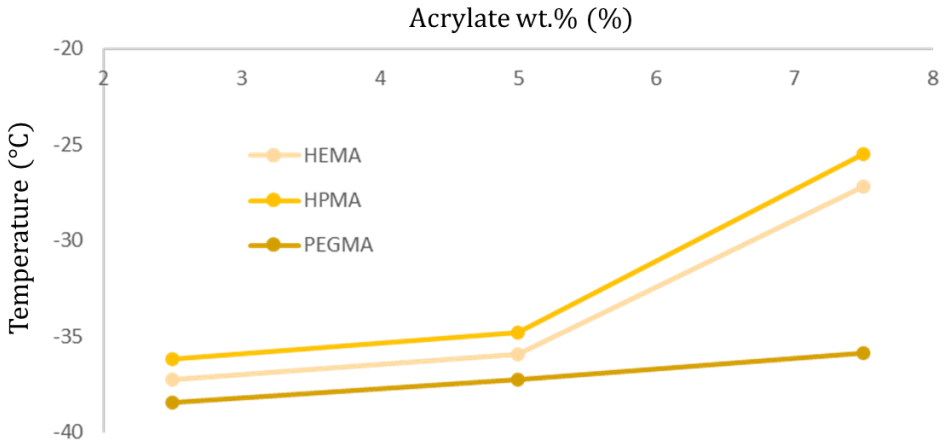

Figure 4.7. Graphical representation of the obtained T_g temperature values for soft samples with different acrylate types and concentrations.

It can also be extracted from the results that the soft/hard ratio, show a lower T_g when containing higher softer components (80:20) compared to its harder counterparts (65:35). This phenomenon is due to limitations in the freedom degree promoted by the harder segments.

The TGA thermograms of all the samples presented a very similar degradation profile where only a single weight drop is measured when the temperature is increased. Table 4.2 also presents the onset degradation temperature determined at 5% weight loss ($T_{5\%}$) as well as the maximum degradation rate temperature (T_{max}), determined from the first derivative's peak maximum were obtained for each polymer specimen by TGA. In all samples, the maximum weight loss rate is produced in the temperature range between 328 and 360 °C. This decomposition is attributed to the cleavage of both urethane and ether

bonds.[40] The degradation process takes place around the same temperature values independently from the acrylate concentration and type, as well as its soft/hard ratio. However, when comparing $T_{5\%}$ a higher thermal stability can be stated in the formulated specimens with higher acrylate wt.%. Additionally, when comparing samples with equal acrylate wt.% but different type, HPMA-based samples appear to have a slightly higher thermal stability than HEMA or PEGMA samples.

The lack of relevant differences in the main degradation temperature is derived from the presence of identical type of chemical bonds through the polymer. Nonetheless, the findings regarding the polymer's thermal stability are in agreement with previous research already exhibiting a small better thermal stability of poly(HPMA) over poly(HEMA).[41]

The thermal stability of the synthesized materials, in the same range of typical TPU elastomers and coatings,[42,43] points towards a good thermal compatibility with current conventional sterilization processes (reaching up to 140 °C) and therefore, a potential use in biologically sensitive applications.

4.3.4 Dynamic mechanical assay

After the samples were photocured, the effects of the different methacrylate cross-linkers and its concentrations on the viscoelastic properties of the PUA hybrid were assessed by Dynamic Mechanical Analysis (DMA).

The obtained results were grouped and compared depending on the type of acrylic monomer (HEMA, HPMA and PEGMA) and its weight

percentage (2.5, 5, 7.5 wt.%) in the final polymer formulation as well as the soft/hard ratio.

In Figure 4.8 can be seen that PEGMA samples presents two thermal transitions (T_α and T_β at around 20-30 ºC and -20 ºC, respectively), while in HEMA and HPMA only that T_β, related to the glass transition, can be identified.

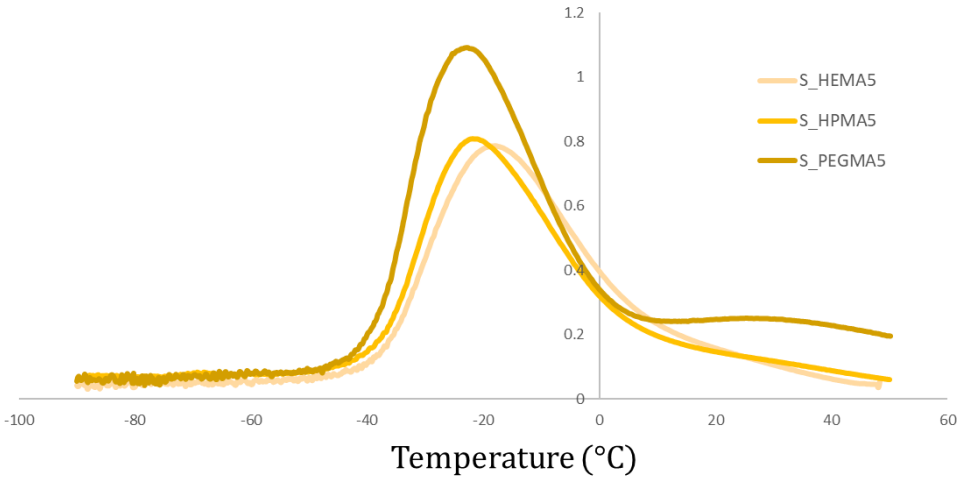

Figure 4.8. Comparative tan ɗ (DMA) graph between polymers with the same soft/hard ratio and acrylate wt.% (5%) but different type. While T_α (20-30 °C) and T_β (-20 °C) are seen for the PEGMA sample, only the T_β transition is observed for HEMA and HPMA-based polymers.

The influence of acrylate content while maintaining the same acrylate type (HPMA) and soft/hard ratio (80:20) is exemplified in Figure 4.9. Samples exhibit a peak broadening and an intensity diminution as the acrylate wt.% is increased. Simultaneously, the tan ɗ peak (or T_β) is shifted to higher temperatures.

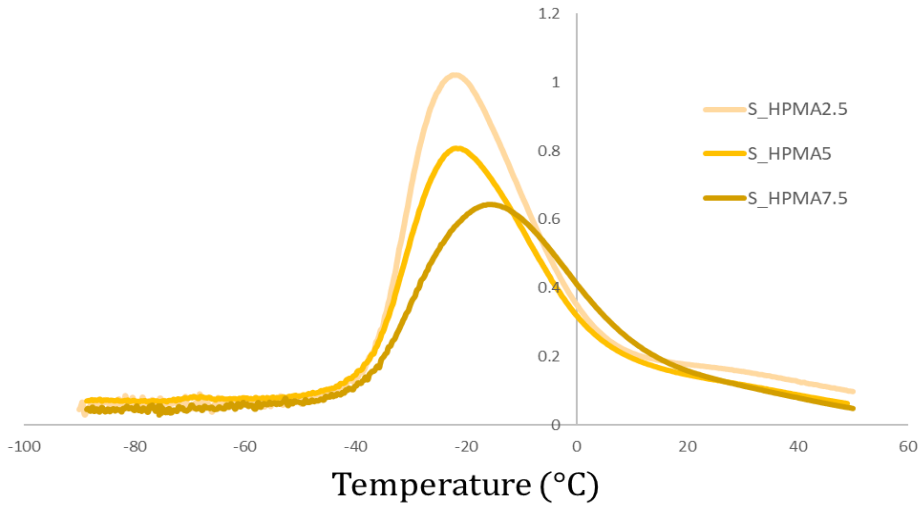

Figure 4.9. Comparative tan d (DMA) graph between polymers with the same acrylate type (HPMA) and soft/hard ratio (80:20) but different wt.%.

That behaviour is more intense in HEMA and HPMA-based polymers than in PEGMA samples and it is observed in both hard and soft samples (Table 4.3). Using the peak intensity and full width at half maximum (FWHM) values of samples containing 2.5 wt.% of acrylic monomer as reference and comparing it to the obtained values for the 5 and 7.5 w.%, it is possible to observe the previously mentioned tendencies. In detail, a peak intensity reduction of 28 and 41% and a broadening of 22 and 59% is determined for hard HEMA samples. In HPMA, the intensity also decrease a 28 and a 39% while the peak widths is increased to 14 and 57%. For PUA samples with 80:20 soft/hard ratio, the peak reduction are about 19 and 43% for HEMA while 21 and 37% when increasing the HPMA wt.% content.

Table 4.3. Synthesized polymer's tan d temperature (T_β), its intensity and the full width at half maximum (FWHM). For reference, samples containing a 2.5% of each acrylate type were determined to be a 100% for the FWHM values. In [a] columns, samples with a 2.5 wt.% of acrylate content are used as reference while in [b], HEMA-based polymers are the reference for comparing between different acrylate types.

Sample	T_β (°C),	Peak intensity	Peak intensity[a] (%)	Peak intensity[b] (%)	Full width at half maximum (°C)	Full width at half maximum[a] (%)	Full width at half maximum[b] (%)
H_HEMA2.5	-3.6	0.839	100	100	35	100	100
H_HEMA5	3.6	0.601	71.6	100	42.6	121.8	100
H_HEMA7.5	6.1	0.498	59.4	100	55.5	158.7	100
H_HPMA2.5	-4.0	0.868	100	103.4	33.3	100	95.1
H_HPMA5	5.1	0.621	71.5	103.3	38.1	114.3	89.2
H_HPMA7.5	3.7	0.533	61.4	107.0	52.3	157.1	94.2
H_PEGMA2.5	-6.1	1.036	100	123.5	35.1	100	100.4
H_PEGMA5	-2.1	0.945	91.2	157.2	29.7	84.5	69.7
H_PEGMA7.5	-0.6	0.951	91.8	190.9	30.5	110.4	54.9
S_HEMA2.5	-25.1	0.975	100	100	27.7	100	100
S_HEMA5	-18.0	0.786	80.6	100	31.2	112.5	100
S_HEMA7.5	-13.6	0.558	57.2	100	41.7	150.3	100
S_HPMA2.5	-22.3	1.021	100	104.7	26.4	100	95.2
S_HPMA5	-21.8	0.808	79.1	102.8	28.7	108.7	92.1
S_HPMA7.5	-15.4	0.644	63.1	115.4	38.8	115.4	93.1
S_PEGMA2.5	-25.4	1.346	100	138.1	24.4	100	88.0
S_PEGMA5	-22.7	1.090	81.0	138.7	26.8	109.9	86.0
S_PEGMA7.5	-22.3	1.046	77.7	187.4	28.6	117.0	68.5

The same analysis was performed for PEGMA-based samples, the peak intensity comparison from 2.5 to 5 and 7.5 wt.% of acrylic monomer, shows a reduction of only a 9 and 8% respectively, in hard samples. With softer samples, the decrease follows up to 19 and 22%. In general, the peak widening effect in those PEGMA samples is minor, being an 17% the maximum obtained of them all. The temperature increase in the T_β can be explained by the reduction in the polymer's chain mobility due an increase of crosslinking points as the acrylate wt.% is increased.

Those samples with lower acrylate wt.% inherently possess a higher number of freely moving polymer chains that cause more internal frictions or entanglements constrains among chains[44] and subsequently, those polymers have a higher energy dissipation capability (higher tan ɗ peak).[45]

In parallel the increase in crosslinking density associated with the higher acrylate wt.%, produces a widening of the tan ɗ peak due to a greater heterogeneity in the average length between crosslinking points. [40,46,47]

Comparing HPMA or PEGMA samples with HEMA's with the same acrylate wt.%, an increase of the peak intensity is noticeable (Figure 4.8). While only a 3 to 15% differences in the peak intensity are seen between HEMA and HPMA, the peak intensity of PEGMA can be up to 90% higher (Table 4.3). Studying the FWHM, an inversely proportional relation between peak intensity and width can be detected again. HEMA-based samples appeared to exhibit the widest graphs when comparing with the other acrylic moieties at the same wt.%. This effect is most notorious for hard PEGMA samples with 7.5 wt.%, where a maximum of a 45% decrease can be seen.

Internal frictions caused by the long polyethylene chain from PEGMA are hypothesized to be the main responsible for the increase in the peak intensity and thus, its higher capability to dissipate energy viscously. The differences between acrylate type are more significative in 7.5 wt.% samples. This effect is related to the greater freedom of movement that chains with higher M_w have inherently and therefore, higher number of interactions. In other words, HEMA is the shortest chain, thus, the internal molecular packaging of a highly crosslinked HEMA-based PUA is more restricted (and elastic) than a PEGMA-based PUA. While having similar crosslinking density with the same acrylate wt.%, in PEGMA PUAs the longer polymer chains allow for more freedom of movements as well as an increased length for entanglement interactions.[44] This increased interaction among the molecules is translated directly into an increased viscous behaviour.

Similarly, the widening effect of the tan δ peak is hypothesized to be related to the non-homogeneous dispersion of the chain length between crosslinking points. Observing the width tendencies, it can be stated that at low concentration values, the random bonding of the acrylic groups during the photopolymerization is similar in all samples and therefore, samples with HPMA and PEGMA moieties show stronger FWHM reductions when increasing acrylate content compared to HEMA. So, as the acrylate concentration increases, the molecular weight between crosslinking points is more homogeneous compared to HEMA PUAs. For HPMA and PEGMA samples, as the wt.% is enhanced, so does their intermolecular steric hindrances, leading them to be relatively more evenly distributed than the HEMA references, obtaining therefore sharper peaks. The effect is enhanced with PEGMA, which has a much longer polymeric chain than the reference, than for HPMA, which only

has the asymmetric methylene differing from the HEMA's molecular structure.

Figure 4.10 shows the tan d curves of samples maintaining the acrylate type and wt.% but changing the soft/hard ratio. Comparing those results, it is possible to notice that softer specimens (80:20) show a higher peak intensity as well as a much lower peak temperature (T_β) in all samples. This effect can be also attributed to the higher presence of the hard and more rigid PU domains that limit the chain movement in the polymer segments in harder samples (65:35).

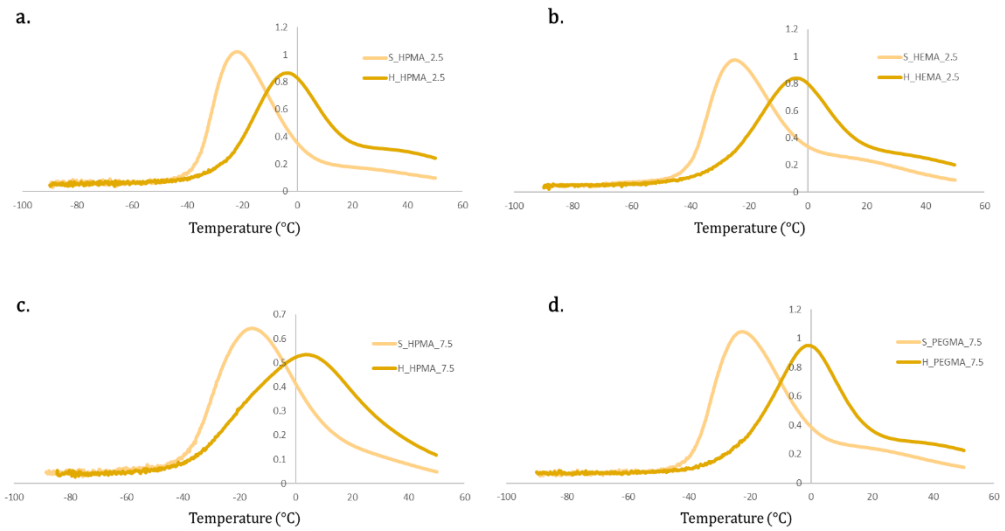

Figure 4.10. Comparative tan d graphs between soft (80:20) and hard (65:35) samples containing different acrylic types and wt.%. A. Comparison for HPMA at 2.5 wt.% B. Comparison for HEMA at 2.5 wt.% C. Comparison for HPMA at 7.5 wt.% D. Comparison for PEGMA at 7.5 wt.%.

Storage modulus (E') curves of the different samples are shown in Figure 4.11. All materials exhibited a similar storage modulus evolution during the heating. First, at low temperature, the materials present a plateau at values around 1 GPa followed by a drop during the transition from glassy

to rubbery state generated by the chain mobility and finally, ending in a rubbery plateau at E' values comprehended between 0.4 and 5.0 MPa.

There are, however, differences in the obtained E' graphs between the acrylate wt.% used, the type of acrylate, as well as the soft/hard ratio of their PU backbone.

Comparing first acrylate wt.% modifications whilst maintaining the rest of variables constant, samples with an acrylate content of a 2.5 wt.% exhibited the steepest slope during the transition process and reach a lower rubbery plateau values than their 5 or 7.5 wt.% counterparts.

Those differences are clearer in HPMA-based polymers than in PEGMA (Figure 4.11, a and c). Using the acrylate type as the only variable function, HEMA and HPMA perform very similar while PEGMA-based formulations show a more intense decrease as well as reach lower E' values in the rubbery plateau (Figure 4.11, d).

This could be attributed to the increased molecular segment length between crosslinking points in the PEGMA-based samples in contrast with HEMA and HPMA samples, that would present an identical length. This segment length increment could facilitate chain movement resulting in a lower E' when the temperature is increased, as seen in Figure 4.11, c. HPMA thermograms were selected to illustrate the effect on the soft/hard ratio.

While in 65:35 soft/hard samples there are little differences when comparing 5 to 7.5 wt.% graphs, in softer specimens appear a proportional trend between the wt.% of acrylate and the E' values in the rubbery plateau (Figure 4.11, a and b). This can be linked to a relative increase of the chain movement restriction produced by the acrylate content in softer samples in contrast with those with higher harder polyurethane

segment composition, where the PU backbone seems to play a stronger role in the generation of its properties.

Those results indicate that the number of acrylic moieties in the polymer are directly related to the material's stiffness. There is little to no differences between the different materials' stiffness at temperatures below the glass transition, mostly due to the predominance of the PU structure. Whereas, at temperature above the glass transition, the acrylic segments appear to have a greater impact on the storage moduli.

These differences are increased with the acrylate wt.% and are seen in specimens with higher polyol content (80:20) due to the increased impact of the crosslinking effect in softer samples as explained previously.

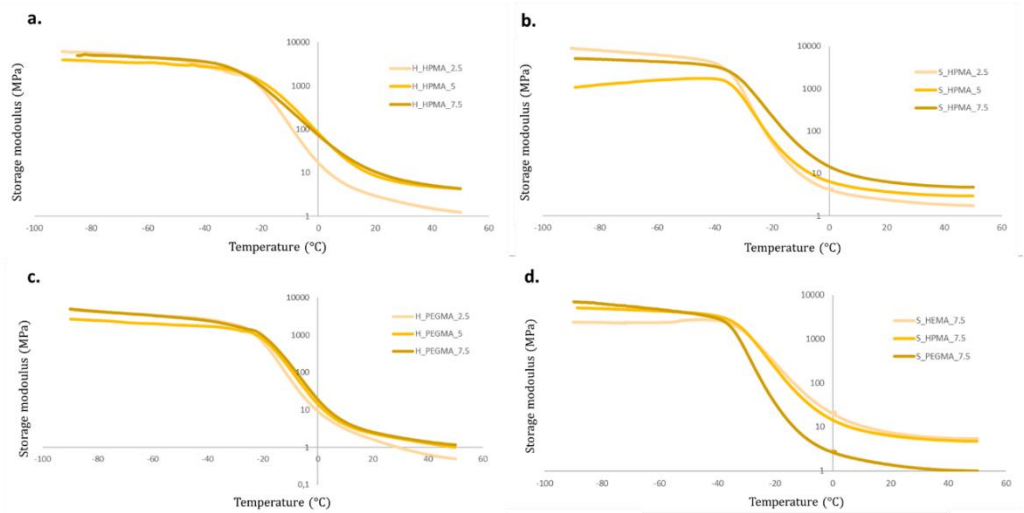

Figure 4.11. E' graphs of different PUA samples. A. comparison between samples with HPMA but different wt.% in hard samples. B. Comparison between HPMA specimens with different wt.% with soft PU backbone. C. E' results for PEGMA-based, hard polymers with varying wt.%. D. E' comparative of different acrylate types with constant wt.% for soft samples.

4.3.5 Shore 00 hardness

The measurement of the PUAs hardness according to a shore 00 methodology are exhibited in Figure 4.12 for each specimen. As observed, the obtained levels of hardness are well distributed from extra soft (a little over 40 SU) from the S_PEGMA2.5 specimens to medium-hard values (with approximately 95 SU) from the H_HEMA7.5. Several tendencies can be spotted within the hardness quantification. First, the obtained results are aligned with the data presented so far, where PEGMA-based samples, due to possessing longer polymeric chains present a more viscous behaviour that can be translated into softer materials compared to HEMA or HPMA polymers. Interestingly, the increment from 2.5 to 5 wt.% in HEMA PUAs appear to have a higher impact in the material's hardness than in HPMA samples. This effect is hypothesized to be generated by the same inner frictions that induced a more viscous behaviour exhibited by DMA and caused by the steric hinderances from HPMA. At 2.5 wt.%, HEMA PUAs exhibited slightly lower hardness values than their HPMA counterparts. However, from 5 and 7.5 wt.%, samples containing HEMA were quantified as harder than the samples containing the same acrylate wt.% of HPMA in both 80:20 and 65:35 compositions. Differences between 80:20 and 65:35 formulations are also noticeable. At all times, 80:20 specimens showed a softer behaviour than 65:35 samples, with differences up to a 28% between H_PEGMA2.5 and S_PEGMA2.5. Beyond the already interesting capability of obtaining a desired degree of softness with a well-known and specific formulation, some of the quantified values are in the same range of certain biological tissues such as heart,[48] kidney,[49] muscle,[50] fetal membranes,[51] tendon, skin[52] or cartilage.[53] Moreover, it has been demonstrated by previous works that although certain healthy tissues exhibit lower hardness values, due to changes in their inner structure (fibrotic or cancerous processes, among others) can

lead them towards having a harder behaviour with similar values to the here presented.[54,55]

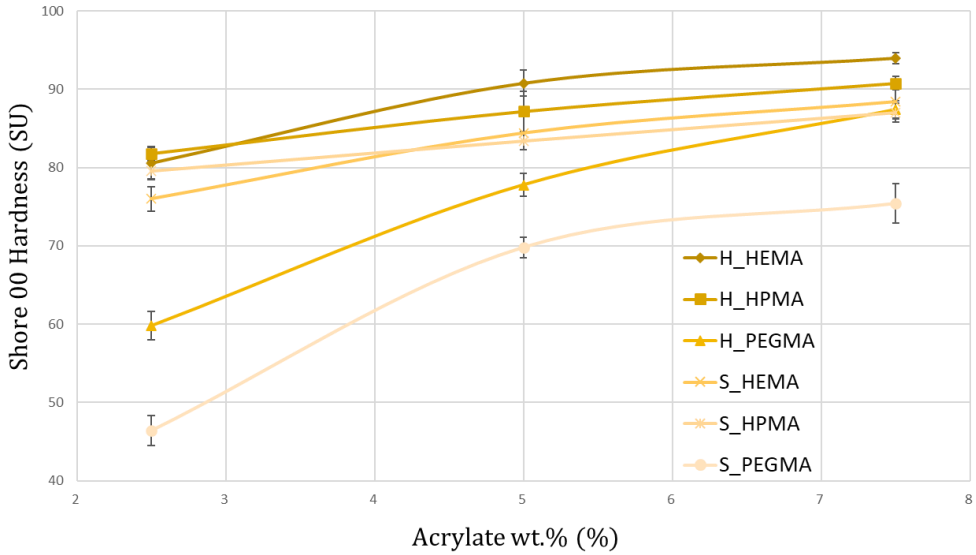

Figure 4.12. Graphical representation of the shore hardness for each synthesized PUA. The obtained results range between extra-soft (<50 SU) to medium-hard. (>90 SU).

4.4 Conclusions

A series of novel, soft photopolymerizable and transparent PUA hybrids were successfully synthesized by using a modified two-steps polymerization procedure. The synthesis was confirmed by FTIR-ATR and NMR analyses. The GPC measurements corroborated the M_w variation on the synthesized PUAs by the addition of different end-capping methacrylic molecules.

Polymer composition of the resulting PUAs varied by changing the soft/hard ratio and the acrylate monomer in the feed, which influenced the thermal, optical and mechanical properties of the final materials. DSC and TGA analyses revealed the effect of the polymer composition on the T_g and on the degradation temperature, confirming the possibility of

adjusting thermal properties by modifying either the acrylate wt.% or the soft/hard segment composition. TGA measurements showed that the decomposition takes place in one stage and the PUAs are stable up to high temperatures (around 340 ºC), which is compatible with current conventional sterilization processes.

The DMA analysis was used to investigate the viscoelastic properties of the photocured PUAs. The results suggested that the network density grows with the increasing acrylic monomer content, thus decreasing the viscous response of the material. This behaviour is also affected by the acrylate type, showing a more intense decrease of the viscous response and lower E' values in the rubbery plateau for PEGMA-based PUAs, which possess longer molecular segment length and higher chain movement among physical crosslinks than for HEMA or HPMA-based PUAs. The photocured PUAs hardness was classified between extra soft and medium-hard. PEGMA allowed the widest range of hardness customization while the incorporation of HPMA provided the lower influence on that property.

The characteristics of the synthesized materials allow them to be used in photocurable 3D printing fields where materials with tuneable properties are needed while not being limited by viscosity requirements (as DIW). Moreover, the softness of these photocurable PUAs fit within the one exhibited by certain biological tissues, so they can be considered as promising candidates for the fabrication of surgical phantoms or models for biomedical applications.

4.5 Acknowledgements

The authors would like to thank Hector Linuesa for useful discussions, as well as Dr. Aleix Conesa for technical assistance on GPC measurements and Dr. Joan Pere López-Olmedo for technical assistance on DMA measurements. This work was co-financed by ACCIÓ and the European Union through the European Regional Development Fund (ERDF) under grant COMRDI16-1-0011-03. This work has also been done in the framework of the doctorate in Material Sciences of the Autonomous University of Barcelona.

4.6 References

1. Park, S.-Y. et al. Preparation and properties of photo-curable coatings based on synthesis of self-photocuring polyurethane acrylate oligomer for pre-coated metal. Mol. Cryst. Liq. Cryst. 706, 129–135 (2020).
2. Gong, H. *et al.* Photopolymerizable and moisture-curable polyurethanes for dental adhesive applications to increase restoration durability. *J. Mater. Chem. B* **7**, 744–754 (2019).
3. Molavi, H., Shojaei, A. & Mousavi, S. A. Photo-curable acrylate polyurethane as efficient composite membrane for CO2 separation. *Polymer* **149**, 178–191 (2018).
4. Huang, J. *et al.* Improvement of biodegradability of UV-curable adhesives modified by a novel polyurethane acrylate. *Prog. Org. Coat.* **95**, 20–25 (2016).
5. Asha, S. K., Thirumal, M., Kavitha, A. & Pillai, C. K. S. Synthesis and curing studies of PPG based telechelic urethane methacrylic macromonomers. *Eur. Polym. J.* **41**, 23–33 (2005).
6. Asensio, M., Costa, V., Nohales, A., Bianchi, O. & Gómez, C. M. Tunable Structure and Properties of Segmented Thermoplastic Polyurethanes as a Function of Flexible Segment. *Polymers* **11**, 1910 (2019).
7. Bae, J.-H. *et al.* Highly Flexible and Photo-Activating Acryl-Polyurethane for 3D Steric Architectures. *Polymers* **13**, 844 (2021).
8. Kury, M., Ehrmann, K., Harakály, G. A., Gorsche, C. & Liska, R. Low volatile monofunctional reactive diluents for radiation curable formulations. *J. Polym. Sci.* **59**, 2154–2169 (2021).
9. Taormina, G., Sciancalepore, C., Messori, M. & Bondioli, F. 3D printing processes for photocurable polymeric materials:

technologies, materials, and future trends. *J. Appl. Biomater. Funct. Mater.* **16**, 151–160 (2018).

10. Chen, K., Kuang, X., Li, V., Kang, G. & Qi, H. J. Fabrication of tough epoxy with shape memory effects by UV-assisted direct-ink write printing. *Soft Matter* **14**, 1879–1886 (2018).
11. Farzan, A. *et al.* 3D scaffolding of fast photocurable polyurethane for soft tissue engineering by stereolithography: Influence of materials and geometry on growth of fibroblast cells. *Eur. Polym. J.* **139**, 109988 (2020).
12. Griffin, M. *et al.* The Current Versatility of Polyurethane Three-Dimensional Printing for Biomedical Applications. *Tissue Eng. Part B Rev.* **26**, 272–283 (2020).
13. Quan, H. *et al.* Photo-curing 3D printing technique and its challenges. *Bioact. Mater.* **5**, 110–115 (2020).
14. Kim, S., Lee, J. & Han, H. Synthesis of UV Curable, Highly Stretchable, Transparent Poly(urethane-acrylate) Elastomer and Applications Toward Next Generation Technology. *Macromol. Res.* **28**, 896–902 (2020).
15. Chen, Z. *et al.* Recyclable thermosetting polymers for digital light processing 3D printing. *Mater. Des.* **197**, 109189 (2021).
16. Chattopadhyay, D. K. & Webster, D. C. Thermal stability and flame retardancy of polyurethanes. *Prog. Polym. Sci.* **34**, 1068–1133 (2009).
17. Fox, T. G. & Loshaek, S. Influence of molecular weight and degree of crosslinking on the specific volume and glass temperature of polymers. *J. Polym. Sci.* **15**, 371–390 (1955).
18. Chen, S., Wang, Q. & Wang, T. Preparation, tensile, damping and thermal properties of polyurethanes based on various structural polymer polyols: effects of composition and isocyanate index. *J. Polym. Res.* **19**, 9994 (2012).

19. Gadley, J. L., Andrade, R. J. & Maia, J. M. Effect of Soft-to-Hard Segment Ratio on Viscoelastic Behavior of Model Thermoplastic Polyurethanes during Phase Transitions. *Macromol. Mater. Eng.* **301**, 953–963 (2016).
20. Song, Y. M., Chen, W. C., Yu, T. L., Linliu, K. & Tseng, Y. H. Effect of isocyanates on the crystallinity and thermal stability of polyurethanes. *J. Appl. Polym. Sci.* **62**, 827–834 (1996).
21. Javni, I., Zhang, W. & Petrović, Z. S. Effect of different isocyanates on the properties of soy-based polyurethanes. *J. Appl. Polym. Sci.* **88**, 2912–2916 (2003).
22. Blackwell, J., Nagarajan, M. R. & Hoitink, T. B. Structure of polyurethane elastomers: effect of chain extender length on the structure of MDI/diol hard segments. *Polymer* **23**, 950–956 (1982).
23. Chu, B. *et al.* Microphase separation kinetics in segmented polyurethanes: effects of soft segment length and structure. *Macromolecules* **25**, 5724–5729 (1992).
24. Semsarzadeh, M. A. & Navarchian, A. H. Effects of NCO/OH ratio and catalyst concentration on structure, thermal stability, and crosslink density of poly(urethane-isocyanurate). *J. Appl. Polym. Sci.* **90**, 963–972 (2003).
25. Sultan, M. *et al.* Synthesis, Characterization, and Application Studies of Polyurethane Acrylate Thermoset Coatings: Effect of Hard Segment. *Polym.-Plast. Technol. Eng.* **56**, 1608–1618 (2017).
26. Wang, F., Hu, J. Q. & Tu, W. P. Study on microstructure of UV-curable polyurethane acrylate films. *Prog. Org. Coat.* **62**, 245–250 (2008).
27. Alishiri, M., Shojaei, A. & Abdekhodaie, M. J. Biodegradable polyurethane acrylate/HEMA-grafted nanodiamond composites with

bone regenerative potential applications: structure, mechanical properties and biocompatibility. *RSC Adv.* **6**, 8743–8755 (2016).

28. Vianna-Soares, C. D., Cherng-Ju, K., Ciftci, K. & Borenstein, M. R. HPMA and HEMA copolymer bead interactions with eukaryotic cells. *Mater. Res.* **7**, 473–477 (2004).
29. An, S., Lee, M. W., Yarin, A. L. & Yoon, S. S. A review on corrosion-protective extrinsic self-healing: Comparison of microcapsule-based systems and those based on core-shell vascular networks. *Chem. Eng. J.* **344**, 206–220 (2018).
30. Bird, S. A., Clary, D., Jajam, K. C., Tippur, H. V. & Auad, M. L. Synthesis and characterization of high performance, transparent interpenetrating polymer networks with polyurethane and poly(methyl methacrylate). *Polym. Eng. Sci.* **53**, 716–723 (2013).
31. Król, P. *et al.* Synthesis and property of polyurethane elastomer for biomedical applications based on nonaromatic isocyanates, polyesters, and ethylene glycol. *Colloid Polym. Sci.* **298**, 1077–1093 (2020).
32. Szycher, M. *Szycher's handbook of polyurethanes*. (CRC Press, 1999).
33. Janardhan, R., Ramamurthy, K. & Anand, J. S. Solution properties of polyurethane. *Polym. Test.* **13**, 397–404 (1994).
34. Wong, C. S. & Badri, K. H. Chemical Analyses of Palm Kernel Oil-Based Polyurethane Prepolymer. *Mater. Sci. Appl.* **03**, 78–86 (2012).
35. Mashouf, G., Ebrahimi, M. & Bastani, S. UV curable urethane acrylate coatings formulation: experimental design approach. *Pigment Resin Technol.* **43**, 61–68 (2014).
36. Wang, M., Liang, S., Gao, W. & Qin, Y. The effect of promoting hydrogen bond aggregation based on PEMTC on the mechanical properties and shape memory function of polyurethane elastomers. *R. Soc. Open Sci.* **9**, 211393 (2022).

37. Flory, P. J. *Principles of polymer chemistry*. (Cornell university press, 1992).
38. Di, Z., Shi, Z., Ullah, M. W., Li, S. & Yang, G. A transparent wound dressing based on bacterial cellulose whisker and poly(2-hydroxyethyl methacrylate). *Int. J. Biol. Macromol.* **105**, 638–644 (2017).
39. Xu, W. J. *et al.* Tuning chain extender structure to prepare high-performance thermoplastic polyurethane elastomers. *RSC Adv.* **8**, 20701–20711 (2018).
40. Krongauz, V. V. Crosslink density dependence of polymer degradation kinetics: Photocrosslinked acrylates. *Thermochim. Acta* **503–504**, 70–84 (2010).
41. Demirelli, K., Coşkun, M. F., Kaya, E. & Coşkun, M. Investigation of the thermal decomposition of poly(2-hydroxypropyl methacrylate). *Polym. Degrad. Stab.* **78**, 333–339 (2002).
42. Herrera, M., Matuschek, G. & Kettrup, A. Thermal degradation of thermoplastic polyurethane elastomers (TPU) based on MDI. *Polym. Degrad. Stab.* **78**, 323–331 (2002).
43. Bahadur, A., Shoaib, M., Saeed, A. & Iqbal, S. FT-IR spectroscopic and thermal study of waterborne polyurethane-acrylate leather coatings using tartaric acid as an ionomer. *E-Polym.* **16**, 463–474 (2016).
44. Kong, D. *et al.* Control of Polymer Properties by Entanglement: A Review. *Macromol. Mater. Eng.* **306**, 2100536 (2021).
45. Barszczewska-Rybarek, I. M., Korytkowska-Wałach, A., Kurcok, M., Chladek, G. & Kasperski, J. DMA analysis of the structure of crosslinked poly(methyl methacrylate)s. *Acta Bioeng. Biomech. 012017 ISSN 1509-409X* (2017) doi:10.5277/ABB-00590-2016-01.

46. Krongauz, V. V. Diffusion in polymers dependence on crosslink density: Eyring approach to mechanism. *J. Therm. Anal. Calorim.* **102**, 435–445 (2010).
47. Jutrzenka Trzebiatowska, P., Santamaria Echart, A., Calvo Correas, T., Eceiza, A. & Datta, J. The changes of crosslink density of polyurethanes synthesised with using recycled component. Chemical structure and mechanical properties investigations. *Prog. Org. Coat.* **115**, 41–48 (2018).
48. A. Tejo-Otero, F. Fenollosa-Artés & I. Buj-Corral. Mimicking Soft Living Tissues for 3D Printed Surgical Planning Prototypes Using Different Materials. in *Actas del XXXVII Congreso Anual de la Sociedad Española de Ingeniería Biomédica* 307–310.
49. Tejo-Otero, A. *et al.* Soft-Tissue-Mimicking Using Hydrogels for the Development of Phantoms. *Gels* **8**, 40 (2022).
50. Choh, C. T. P., Wall, M. L., Brown, M. D., Nicolson, A. M. & Simms, M. H. Use of durometry in assessment of venous disease. *Phlebol. J. Venous Dis.* **25**, 94–99 (2010).
51. Oflaz, H. A biomechanical comparison between tissue stiffness meter and shore type 00 durometer using fresh human fetal membrane cadavers. *Biocybern. Biomed. Eng.* **36**, 138–144 (2016).
52. Chanda, A. Biomechanical Modeling of Human Skin Tissue Surrogates. *Biomimetics* **3**, 18 (2018).
53. Spahn, G. *et al.* Evaluation of cartilage defects with near-infrared spectroscopy (NIR): An ex vivo study. *Med. Eng. Phys.* **30**, 285–292 (2008).
54. Yoon, Y. C. *et al.* Quantitative assessment of liver fibrosis using shore durometer. *Ann. Surg. Treat. Res.* **93**, 300 (2017).

55. Hughes, J. D. *et al.* Higher-Resolution Magnetic Resonance Elastography in Meningiomas to Determine Intratumoral Consistency. *Neurosurgery* **77**, 653–659 (2015).

CHAPTER

5

DEVELOPMENT OF A 3D BIOPRINTING PLATFORM

5.1 Introduction

Figure 5.1. Inventia Life Science's main logo

Inventia Life Sciences Ltd. is an Australian private company based in Sydney (New South Wales, Australia). Founded in 2015, this biotech company has developed a bioprinting platform that targets the possibility of obtaining 3D cell cultures in a high throughput approach. The main objective of developing those 3D cultures is to generate more representative models that can be helpful in the research for new drugs or techniques (Figure 5.2). Thus, the final aim of the 3D bioprinting platform, called "***Rastrum***" (Figure 5.3) is tackling at the same time the need for an improved system that can replicate better the biological environment while removing the difficulties of doing so.

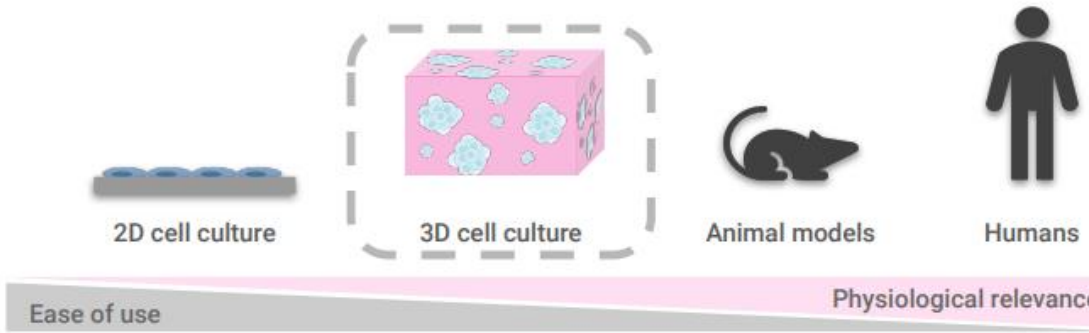

Figure 5.2 Representation of how 3D cultures are more physiologically relevant than current 2D cell cultures but are more complex to work with. They can replicate more easily the true cell morphologies and replicate much more accurately the cellular response to certain treatments.

The summary of the work performed during the internship will be divided and discussed into two main sections: *3D bioprinting materials development and Rastrum Upgrading.*

As most of the information regarding the work carried on during the internship is under a confidential agreement, names and relevant data have been changed in this thesis to protect the overall intellectual property of the company.

Figure 5.3. Rastrum, the 3D printing platform that the author helped to develop during its internship.

5.2 3D bioprinting material development

Aiming for the achievement of (bio)materials that could successfully replicate physiological environments of certain tissues, parameters such as stiffness or pore size need to be perfectly controlled. Moreover, the addition of biological motifs such as RGD, YIGSR or IKVAV provide signals recognized by cells which allow an improved compatibility with the synthetic matrix.

The development of methodologies that control the quality of the product is crucial for the success of any manufacturing-related business. One of the main tasks performed during the internship, was focused on ensuring that standard operation procedures (SOP) were developed and followed for always ensuring an optimal level of behavior reactivity for the synthesized and distributed inks as well as it's expiry date.

5.2.1 Control of gen 2 matrixes

Generation II matrixes from Inventia are generated through the reaction of 2 components (called from now on Bioink A (PEG-based) and Activator B for confidentiality issues) which, when mixed in a previously well stablished proportion, an instantaneous, non-toxic crosslinking reaction is triggered, generating the matrix (Figure 5.4). The specific relationship between quantities of products A and B is based on the presence of certain concentrations of reactive groups in each one, therefore, the characterization of how these groups prevail with time is vital to ensure the correct behavior of the printing process and the 3D matrix generation.

Figure 5.4. 3D Drop-on-Demand Bioprinting process of the Rastrum platform. Upon contact of the two components, gelation occurs instantly at room temperature without harming the embedded cells.

By the time the author started with this stability project, the studies of bioink stability already labeled it as a highly stable product while Activator B did demonstrate high levels of self-reactivity so far. Thus, it was determined that the component B of the inks was the one which could stablish the expiration date of the sold packs. As the chemical performance is the main interest of the product, studies regarding the reactivity were chosen aiming to understand how this product was aging at different conditions. To do that, thanks to the possibility of reacting the Activator to a molecule "X" that causes conformational changes and turns into a colored substance, a photochemical assay was performed, and it was feasible to determine the concentration of the reactive group in B by measuring at a certain wavelength and compare it with a calibration curve. The calibration curve was generated with a known concentration of a small molecule presenting the same chemical group (Figure 5.5).

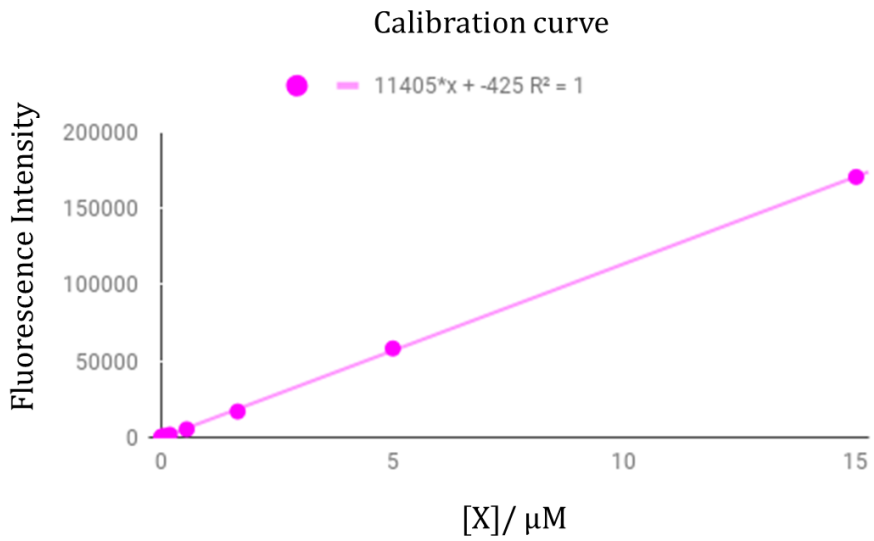

Figure 5.5. Calibration curve for the measurement of the reactive group concentration based on the fluorescence response when reacting against compound "X".

Due to the great number of necessary replicates to certify the method's validity, 96 well plates were used. Although the method so far generated quite incoherent data, even when several researchers performed the same methodology and obtaining results with significative differences, instability of the chemical compound as well as random problems with the activator through time were labeled as the main issue. Nonetheless, by the almost ceaseless repetition of the assay aiming to generate a standardized procedure and thus establishing the acceptable results of the analyzed products for further manufacturing practices, thanks the use of different types of 96-well plates and some serendipity, it was discovered that the non-attachment coating on the well's bottom in some culture plates reacted partially with the Activator B thus exhibiting lower concentration values on the experiment.

To confirm the observed hypothesis, a battery of equal samples but measured on different plates were performed (Table 5.1). In the experiment, differences going up to a 20% could be observed between the coated and non-coated plates. Moreover, within the coated results, there were inner differences that correlate with the obtained so far. Apart from the technical implications for the following internal SOP for the quantification and validation of the products, it was a way to discover a few errors present in some customer sites that could be fixed.

Finally, this test with the non-coated plates, allowed to stablish a 12-months use of the activator B while keeping it froze without losing any of its properties.

Table 5.1. Summary of the fluorescence results from the characterization of Activator B. The normalized values were obtained by using the absorbance values in the equation obtained from the calibration curve. It is possible to observe lower values for certain conditions.

F-code	Absorbance				Raw "X"%	Normalised "X"%
	0,0380	0,0380	0,0380	0,0380		
Condition A-1	0,3380	0,3320	0,3320	0,3310	90,47	90,47
Condition A-2	0,3370	0,3420	0,3300	0,3310	91,01	91,01
Condition A-3	0,3400	0,3390	0,3350	0,3350	91,69	91,69
Condition B-1	0,3350	0,3380	0,3340	0,3340	91,08	91,08
Condition B-2	0,2870	0,2510	0,2540	0,2480	68,10	68,10
Condition B-3	0,3430	0,3410	0,3420	0,3430	93,22	93,22
Condition C-1	0,3360	0,3450	0,3310	0,3340	91,47	91,47
Condition C-2	0,3530	0,3510	0,3470	0,3500	95,67	95,67
Condition C-3	0,3360	0,3350	0,3350	0,3340	91,01	91,01
Condition D-1	0,3300	0,3290	0,3240	0,3220	88,33	88,33
Condition D-2	0,3160	0,3030	0,3070	0,3090	82,99	82,99
Condition D-3	0,2900	0,2820	0,2910	0,2790	75,89	75,89
Condition E-1	0,2880	0,2950	0,2930	0,2990	78,41	78,41
Condition E-2	0,2950	0,2820	0,2940	0,2690	75,73	75,73
Condition E-3	0,2700	0,2520	0,2610	0,2660	68,78	68,78
Condition F-1	0,2660	0,2560	0,2710	0,2870	71,15	71,15
Condition F-2	0,2560	0,2440	0,2810	0,3000	71,23	71,23
Condition F-3	0,3310	0,3320	0,3290	0,3370	90,17	90,17
Condition G-1	0,3370	0,3280	0,3300	0,3330	90,09	90,09
Condition G-2	0,3330	0,3390	0,3250	0,3320	90,17	90,17
Condition G-3	0,3320	0,3280	0,3290	0,3410	90,24	90,24

5.2.2 GrowInk

While the company has its own library of different matrixes developed for specific tissues, it is possible to adapt new materials to be used as potential bioinks for the platform. Thanks to an external collaboration with UPM Biomedicals from Finland, GrowInk-T, an animal free, biocompatible and shear-thinning material based on nanocellulose was adapted to be used by the 3D bioprinter. The printing optimization process began with stablishing the printing parameters as well as the concentration of GrowInk that could support the final matrix structure

geometry without presenting blocking issues while printing through a drop-on-demand system. To assess the successful printing of the ink, a structure composed of 1 single plug of a few nL (Figure 5.6) were printed in each well of a 96-well plate.

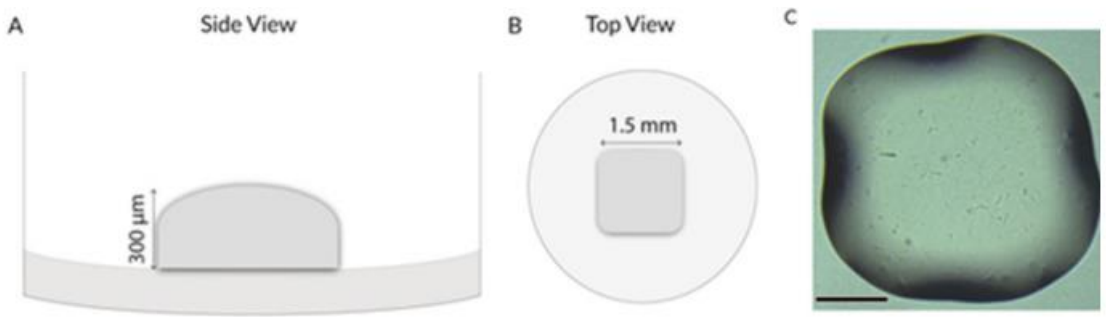

Figure 5.6. Representative 3D bioprinted GrowInk-T plug in a 96-well plate. A) Schematic side view of the structure, 300 µm in height, B) Schematic top view of plug, 1.5 mm in diameter, C) Bright-field image of the GrowInk-T cuboid structure, Scale bar: 500 µm

Some printing parameters were modified in each row to observe potential differences in the final geometry of the printed structure (Figure 5.7). The main modified variables were: the applied pressure, the opening time of the nozzle and the firing frequency. Each of those variables were studied with two concentrations previously defined between UPM Biomedicals and Inventia's research team to ensure a correct ink behavior. After several trials, together replicability and precision of the printed geometry as well as the lack of ink in the pneumatic systems rendered a previously defined concentration "X" with parameters "Y" (Figure 5.7, row B) as the most promising combination for the process in development.

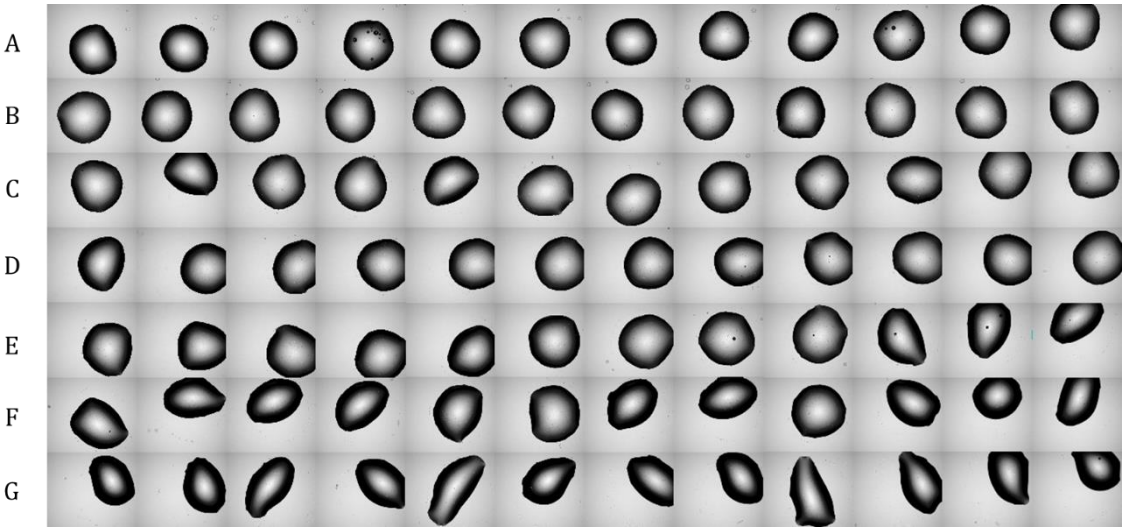

Figure 5.7 Brightfield image taken from a printed 96-well plate. Each row was printed using modified parameters to observe differences and aiming to achieve the optimal for the selected ink formulation.

To really determine the feasibility, a full 96 well plate was printed with the defined parameters (Figure 5.8). Only 2 out of the 96 printed wells presented issues and thus, the selected parameters and concentrations were certified as optimal to proceed with further experimentation in the adaptation of the ink for the 3D-bioprinting platform.

Afterwards, the cell compatibility with the selected concentration was assessed using MCF-7 cells. MCF-7 cell line is an immortalized mammary cancer cell line widely used for laboratory cell culture. Also, this cell line was chosen as the model cell based on data from previous reports that exhibited the generation of well-defined 3D spheroid structures in nanofibrillar cellulose hydrogels. Nanocellulose hydrogels are extremely hydrated porous materials with good mechanical properties that have been demonstrated for 3D cell cultures mimicking the extracellular matrix (ECM) without presenting cytotoxicity. Among the different reported approaches for crosslinking nanocellulose,[1] one protocol relies

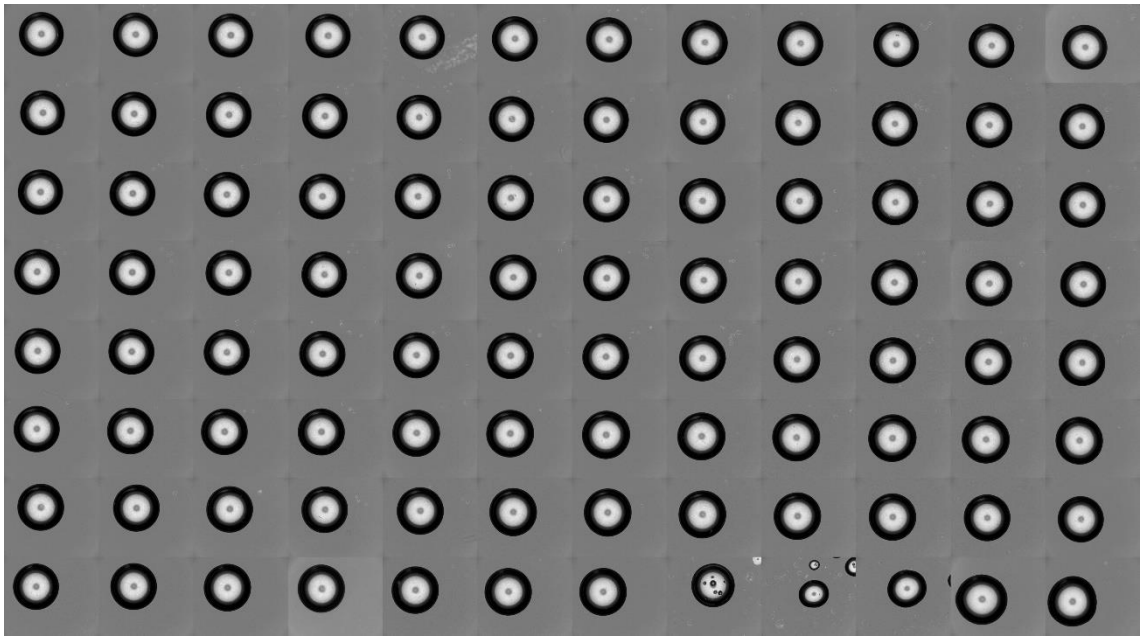

Figure 5.8. Brightfield image of a full printed 96-well plate using the most promising parameters from previous experiments. The reproducibility and precision of the structures (it only failed 2/96) determined that it was a good procedure to advance to the next steps of the ink adaptability process.

on the use of metal ions as ionic crosslinkers (Ca^{2+}, Cu^{2+} or Fe^{3+} among others). Due to the presence of ions in cell culture media, ionic crosslinking reactions are the main drivers in the soft, instant gelation for GrowInk material, which result when these two components are mixed thoroughly and the material's viscous behavior change. However, those crosslinking reactions could not take within the Rastrum system as it was determined that the increase in viscosity was too high for being correctly printed.

The experimental tests showed that not only the incorporation of media was an issue but also, the media coating the cells through surface tension forces needed to be removed in order to not generate enough ionic strength to trigger crosslinking reactions. As a solution, cells were centrifuged and washed with distilled and microfiltered water. The use of water with low ionic strength (hypotonic) generated a secondary issue

regarding cell viability through cytolysis due to the swelling of the cells (Figure 5.9). The prevention of the hypotonic shock and massive cell death inside the inks was prevented by the incorporation of a disaccharide in a certain concentration. This molecule protected the cell while not triggering crosslinking reaction and thus, maintaining the same viscosity levels as the previously studied, thus allowing to print the selected structure of GrowInk containing cells (Figure 5.10).

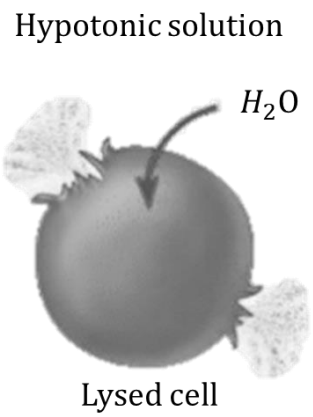

Figure 5.9. scheme of cytolysis by exposure of an animal cell to hypotonic solution.

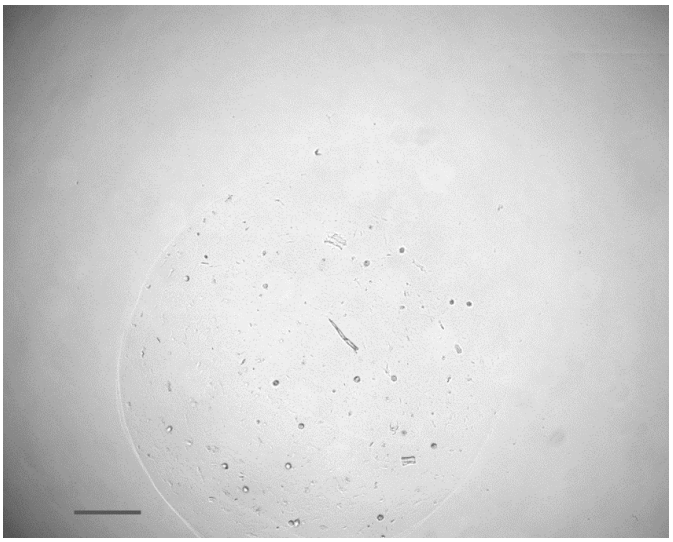

Figure 5.10. Brightfield image of a printed GrowInk plug containing MCF7 cells 1 day after being printed. The lack of resolution is due to the presence of media to help cell growth. The scalebar is 500 µm.

Nonetheless, the true meaning of a successful process was defined as the generation of potential spheroids that could be used as cellular models for basic research. Therefore, several models were generated modifying

the disaccharide concentration as well as adding certain peptides too see which one was the one allowing for the generation of the desired cellular constructs.

The printed structures were studied for at least 7 days and then, dyed with a life-death method to assess with fluorescence, both the overall cytotoxicity and to clearly see the generation of potential cellular structures.

With the generated data (Figure 5.11), it was possible to certify the cellular survival inside the ink after 7 days as well as the initial generation of more complex structures.

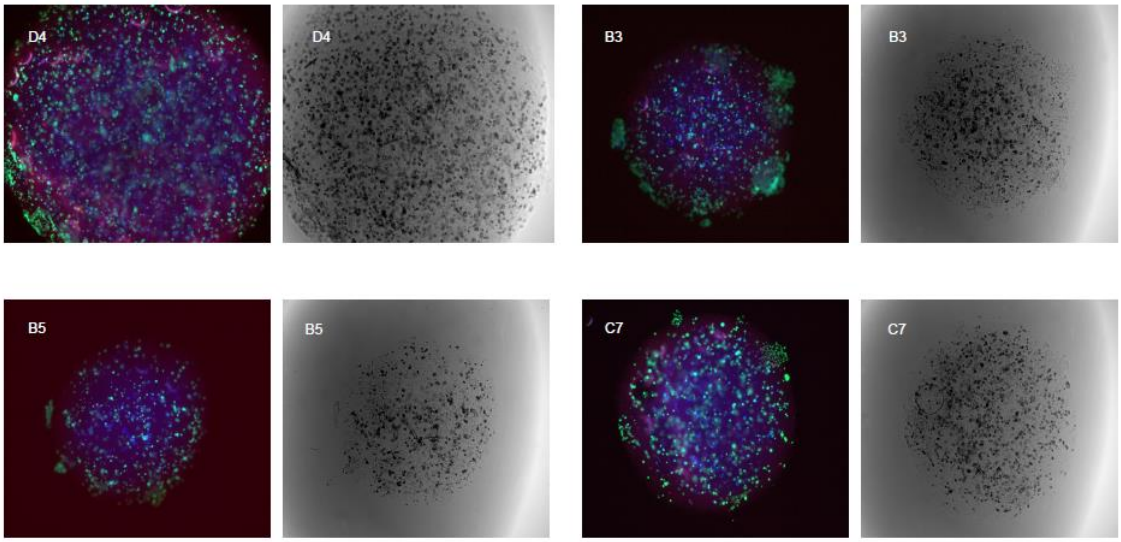

Figure 5.11. Life-death fluorescence images and brightfield images of MCF-7 GrowInk plugs at day 7. It is possible to observe that in some plugs there were cell aggregations similar to the initial constructs of spheroids. Each number at the top of the images represent the well of the 96-well plate they were seeded.

Although more studies regarding the use of GrowInk and Rastrum are taking place to further develop and see how far the material can advance with the help of Inventia, the author proceeded to work in other projects.

5.2.3 Hepatocarcinoma model

The final project regarding ink development where the author participate, was helping in the final development of a hepatocarcinoma model.

Most of the work regarding ink selection and concentrations had already been performed but the presence of optimal spheroids within the 3D printed plugs were still missing. For the final ink optimization, a Human hepatocyte carcinoma cell line called HepG2 was used. Those cells were printed using different inks that varied in their rigidity or the concentration of peptides present in the molecular structure and cultured for 7 days to study the spheroid formation.

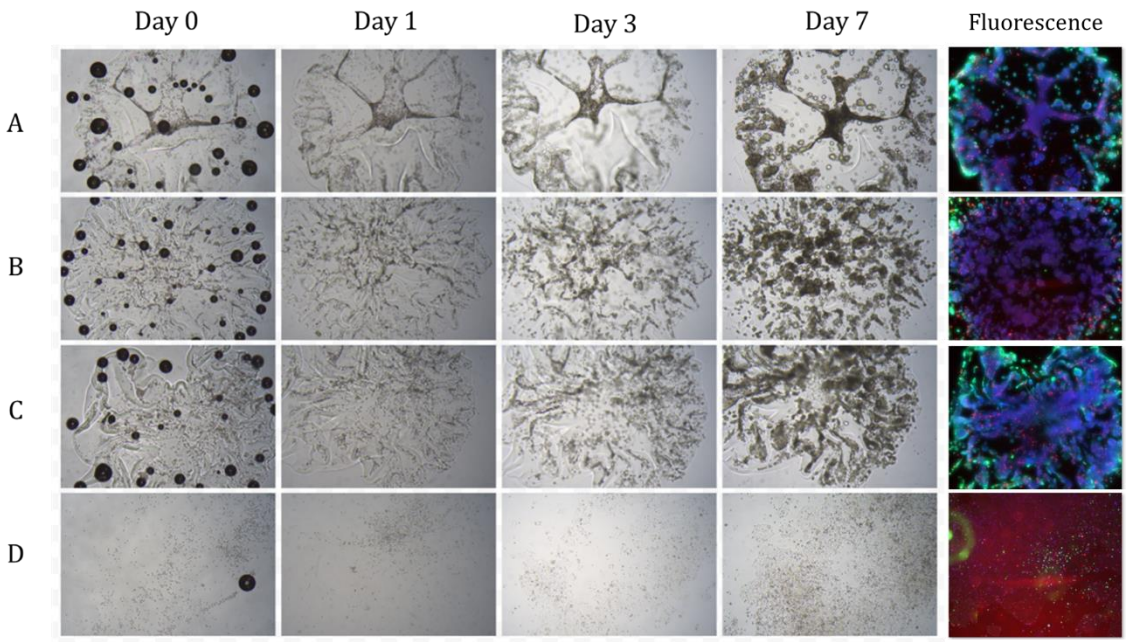

Figure 5.12. Cell model study on HepG2 cell line. A, B, C and D are different inks tested to observe differences in the generation of cell spheroids that could mimic the real tissue for research purposes. It is possible to observe in the fluorescence images on day 7, how the insides of the spheroids present violet colors due to the mix between living and dead cells from the lack of nutrient and oxygen perfusion. This is the same behavior seen in real spheroids.

On day 7, an immunofluorescent life-death assay was performed to see the cell viability in those constructs. Only the most representative models are presented and exhibited in Figure 5.12.

The obtention of representative spheroids within 7 days of normal culture in the printed 3D structures certified the success of these experimental procedure. Although conditions A, B and C demonstrated all the capability of generating those cellular structures, condition C appeared to be the one producing the most similar histological shape to the real hepatic carcinoma. More studies with these models are being carried on by both Inventia and some external collaborators.[2–4]

5.3 3D bioprinting platform (Rastrum) upgrading

5.3.1 System sterilization

One of the many advantages of Rastrum versus other 3D-bioprinter platforms is that it is itself a biosafety cabinet thanks to the incorporation of a laminar flow and several HEPA filters (Figure 5.13). However, to maintain a complete sterile system and to ensure that no cross-contamination takes place during the printing process (called *printrun*), there is the need to ensure minimal presence of microbial or cellular components in the overall internal pneumatic system. Several factors add complexity to the cleaning processes such as being regularly in contact with culture media with cells, having the overall system enclosed in the dark without possibility of being UV-sterilized or the different types of materials that compose the overall circuit (stainless steel, thermoplastic polyurethane, polypropylene or medical-grade silicone, among others).

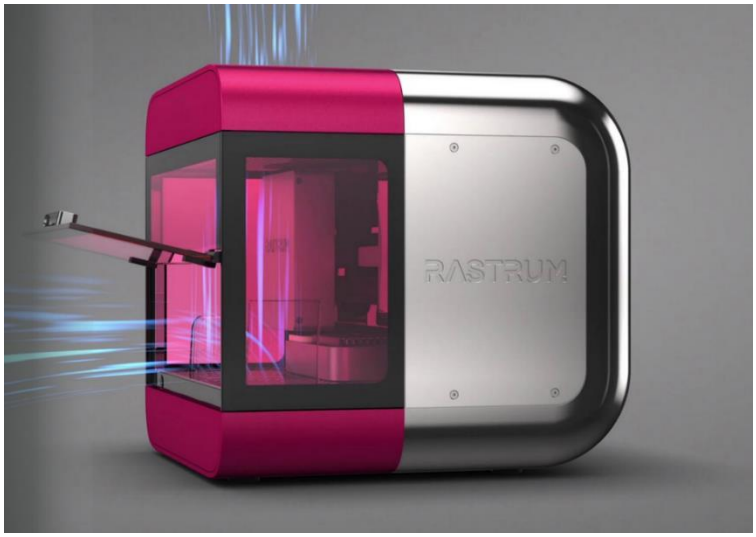

Figure 5.13. Representation of the laminar Flow inside a working rastrum 3D printer.

The easiest protocol to determine the presence of bacterial contamination was to print a few mL of distilled water through every nozzle of the system and, with a sterile pipette, add few µL into a broth and put it at 35°C for several days. If after 14 days, no presence was detected by appearance of turbidity in the media, the printer was labeled as sterile (Figure 5.14).

Although the first approaches to perform a deep cleaning of the system were through the repetitive use of a highly concentrated phosphate buffer (PBS) and several washes with Ethanol (70°), it rendered inefficient, and the printer presented bacterial contamination.

The next steps involved the use of hydrogen peroxide at different concentrations. Even it demonstrated to be more efficient than the previous method, bacterial presence was still detected while needing a more thorough afterwards cleaning process was needed. Very few ppm of

H_2O_2 demonstrated to have enough effect on cells to be detected by cytotoxicity assays such as life-death assay or *prestoblue*.

The incorporation of a different, highly reactive reagent used to deeply disinfect medical equipment into a these sensitive, complex, and overall expensive system was both brave and, as later found, successful. The optimal process of the system clean-up took several weeks of iterations

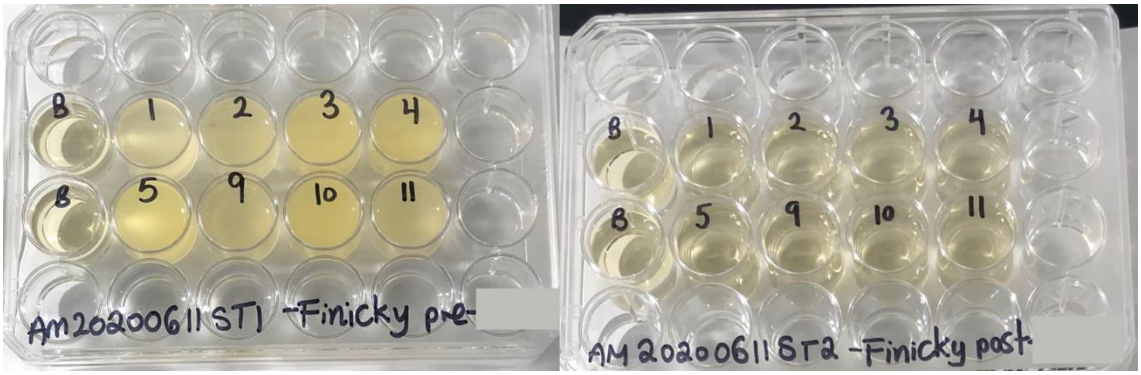

Figure 5.14. Sterility tests performed on the printer named "Finicky Flemming" before (left) and after (right)) the developed sterility process. Each well represented the sterility of each nozzle/ printing chamber and 2 baseline controls without any addition were used as negative controls.

and a check-up of every part of the pneumatic circuit to assess that no rustiness or presence of salts were left in it. Nonetheless, a multidisciplinary team composed of an informatic engineer, a cell biologist, a materials scientist, and a physicist developed a method of cleaning 99.99% of all biological residues while no harming the system whatsoever and doing it all in less than 30 minutes (Figure 5.14). This process optimization allowed to perform this test every day in every printer in use worldwide and ease the next step in the process workflow, the greenlighting.

5.3.2 Greenlighting

The Greenlighting was the other project regarding the system upgrading where the author took part. It consisted in creating a workflow designed to ensure a correct usage of the platform by all users, independently of its initial background. As the main goal of the company was to ease the access of this technology to researchers from a very different field, it was an incredibly necessary process for the upscaling of the bioprinter.

As a summary, the workflow was a series of steps designed to be performed at the beginning of every day for the first user, a series of small reminders for each researcher prior and during the performance of any of its assays. As the first step a full cleanup of the printer took place to prevent any contamination from the last usage. Aiming to optimize time, it was also designed to use the cleaning water to print several patterns that the user needed to assess. Other interesting issues were the reminders of closing or opening certain lids to prevent external contamination, the use of gloves or when to thaw ink cartridges. As a way of certifying that the created pathway was easy enough for everyone to follow, everyone in the company (more than 35 people) were invited to test it, from the CEO to the office's assistant. The results showed that independently of who did the experimental procedure with the platform, 3D cellular matrixes with no contamination were created as well as a tool to certify the status of each printer component remotely.

On the top of it all, together with the marketing department, a small infographic was created aiming to ease the visualization of the overall created workflow for both the greenlighting and the printing process, thus helping potential new users to easily understand how and what they would achieve with Rastrum, the 3D bioprinting platform.

Observing the overall workflow and as a summary, the author helped in the development of steps 1, 3 and 5 thus moving the platform a little closer to becoming and incredibly powerful tool for new developments regarding biomedical advances.

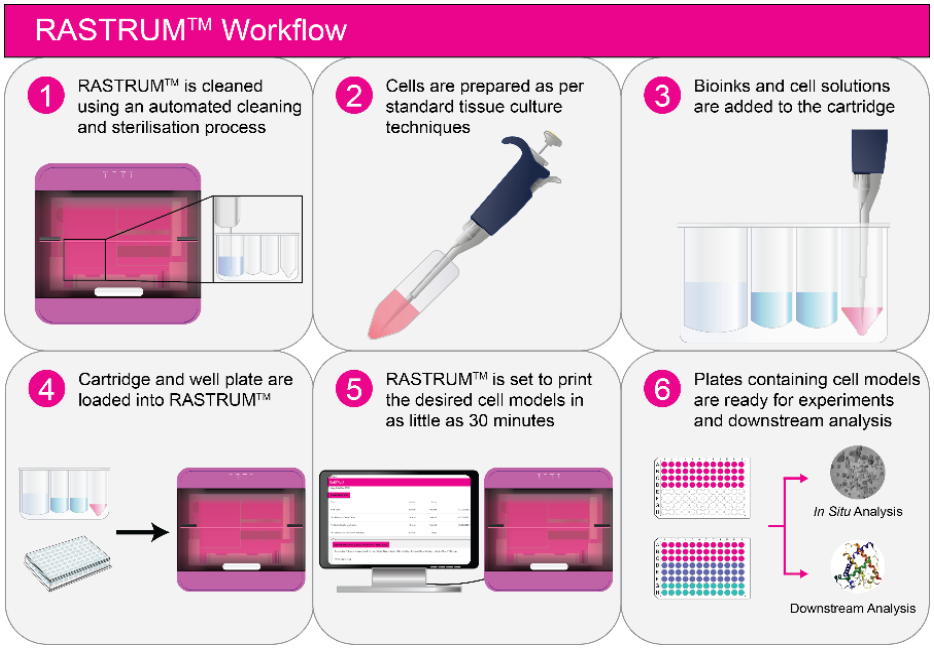

Figure 5.15. Infographic of the overall workflow with Rastrum, the 3D bioprinting platform.

5.4 References

1. Curvello, R., Raghuwanshi, V. S. & Garnier, G. Engineering nanocellulose hydrogels for biomedical applications. Adv. Colloid Interface Sci. 267, 47–61 (2019).
2. Belfiore, L. et al. Generation and analysis of 3D cell culture models for drug discovery. Eur. J. Pharm. Sci. 163, 105876 (2021).
3. Maharjan, B. R., McLennan, S. V., Yee, C., Twigg, S. M. & Williams, P. F. The Effect of a Sustained High-Fat Diet on the Metabolism of White and Brown Adipose Tissue and Its Impact on Insulin Resistance: A Selected Time Point Cross-Sectional Study. Int. J. Mol. Sci. 22, 13639 (2021).
4. Utama, R. H. et al. A covalently crosslinked bioink for multi-materials drop-on-demand 3D bioprinting of three-dimensional cell cultures. http://biorxiv.org/lookup/doi/10.1101/2021.02.18.431759 (2021) doi:10.1101/2021.02.18.431759.

CHAPTER

6

THESIS CONCLUSIONS

6.1 Thesis conclusions

In the herein presented doctoral thesis, significative progresses in the use of advanced polymers for the fields of self-healing and additive manufacturing have been achieved. The significant contributions directed towards resolving some of the major challenges that were currently preventing the inclusion, or complete adoption, of those technologies in the industrial fabric are described:

i) A *high-efficient self-healing polymeric system capable of working efficiently at low and ultra-low temperatures* was successfully obtained aimed for its application in high demanding fields such as aeronautics, automotive or windmills. By analyzing monomeric mixture behavior and its reaction kinetics of different ROMP monomers with different next-generation metathesis catalysts, it was possible to assemble an industrially scalable system that fulfilled all the theoretical self-healing steps at harsh environmental conditions. The creation of a composite material with current commercially used epoxy resins and manufactured following industrially set limitations, allowed to generate a self-healing system fully able of being introduced into industrial workflows. The replication at laboratory scale of the true climatological conditions that the composite materials will face in the real application was pivotal to create a representative system for real applications.

ii) The *synthesis of UV-Curable Polyurethane-Acrylate hybrids with tunable hardness and viscoelastic properties on demand* was achieved through a controlled and industrially scalable

two-step procedure. A controlled causal effect involving the final PUA's thermal and mechanical behavior were achieved through a careful polymer synthesis process. In the developed protocol, both the ratio of each polymer chain segments and the use of different acrylate monomers possessing differences on its molecular weight were successfully tuned. The range of achieved properties ranged from behaving as medium-hard to extra-soft materials, which translates into the possibility of obtaining materials with the potential to mimic certain biological tissues. Moreover, due to the photopolymerization step within the procedure, it has been possible to adapt this library of polymers to its use as materials for additive manufacturing. The successful synthesis of the reported library of polymers holds the potential to improve the adaptability of AM technology while advancing the field of personalized medicine with the creation of surgical guides.

iii) It was possible to advance into the full *development of a state-of-the-art 3D bioprinting platform*. The creation of standardized procedures over the stability of the used bioink, created a work frame for improved customer success. The material's portfolio of the 3D bioprinting platform was widened due to the adaptation of novel nanocellulose-based bioinks. A physiologically relevant cellular model for liver tissue was developed considering critical factors such as the interactions between the matrix material, the bioprinting parameters and the cellular components. The obtention of the cellular models in a minimized, high-throughput fashion, withhold the capability of boosting fields ranging from drug

discovery, personalized medicine to basic molecular biology research.

There are still plenty of limitations holding the application of most advanced polymers and their technologies into real, industrial environments. Nonetheless, the great impact that those materials could generate into society is a driving force powerful enough to fuel the work presented in this thesis. The (maybe) small, but rather significant progression carried in the generation of a self-healing system, specifically designed for applications were its implementation would maximize the application and economical turnover, the synthesis of a polymeric system settling improved bases for widening AM in health sector, or contributing to the generation of a novel 3D bioprinting platform with limitless potential, have fulfilled the main objective of this thesis of bringing a novel generation of materials a little bit closer to reality.

ANNEX

SUPPORTING INFORMATION

Development of a Highly Efficient Extrinsic and Autonomous Self-Healing Polymer System at Low and Ultra-Low Temperatures for High-Performance Applications

Guillem Romero-Sabat, Elena Gago-Benedí, Joan Josep Roa Rovira, David González-Gálvez, Antonio Mateo, Sandra Medel Fernández, Ainhoa Tolentino Chivite

A.1 Monomer mixtures fluidity at -20°C

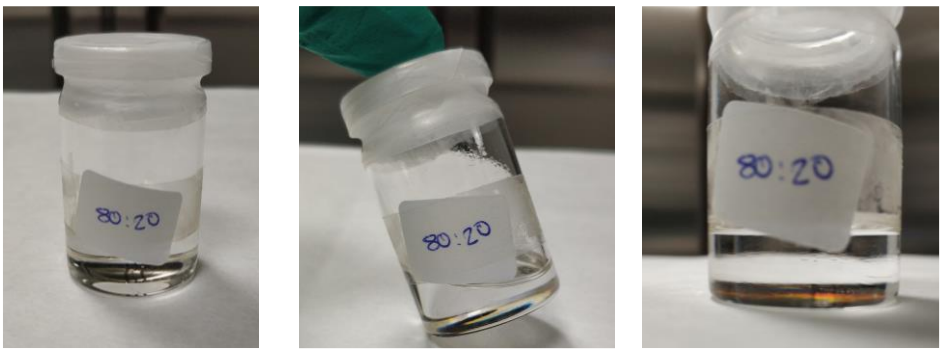

Figure S1. 80:20 ENB:DCPD mixture at -20°C after 14 days. The blend presents fluidity and no phase separation.

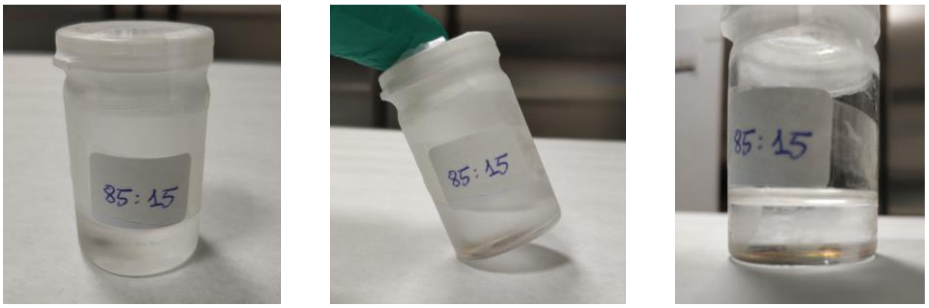

Figure S2. 85:15 ENB:DCPD mixture at -20°C after 14 days. The blend presents fluidity and no phase separation.

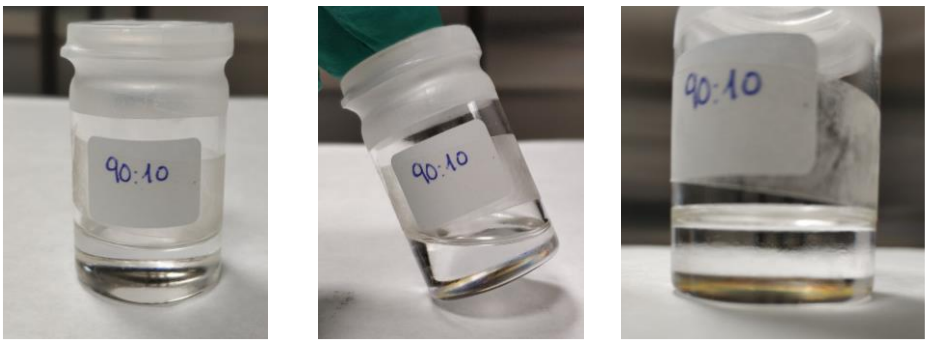

Figure S3. 90:10 ENB:DCPD mixture at -20°C after 14 days. The blend presents fluidity and no phase separation.

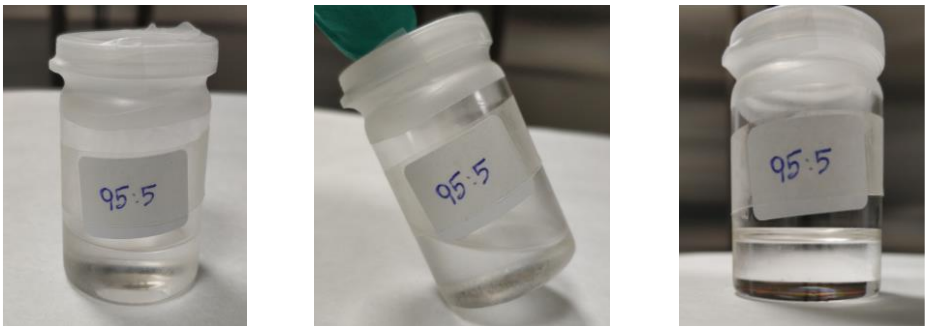

Figure S4. 95:5 ENB:DCPD mixture at -20°C after 14 days. The blend presents fluidity and no phase separation.

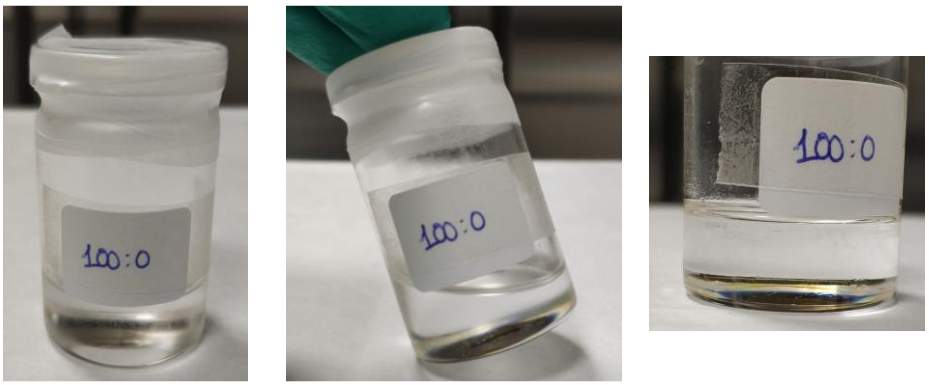

Figure S5. 100:0 ENB:DCPD mixture at -20°C after 14 days. The blend presents fluidity and no phase separation.

A.2 Monomer mixtures fluidity at -70°C

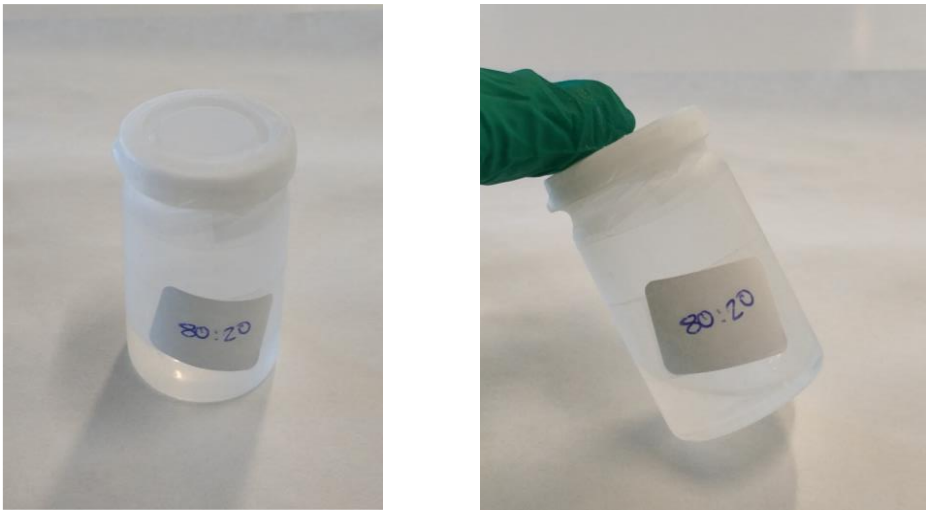

Figure S6. 80:20 ENB:DCPD mixture at -70°C after 14 days. The blend presents fluidity and no phase separation.

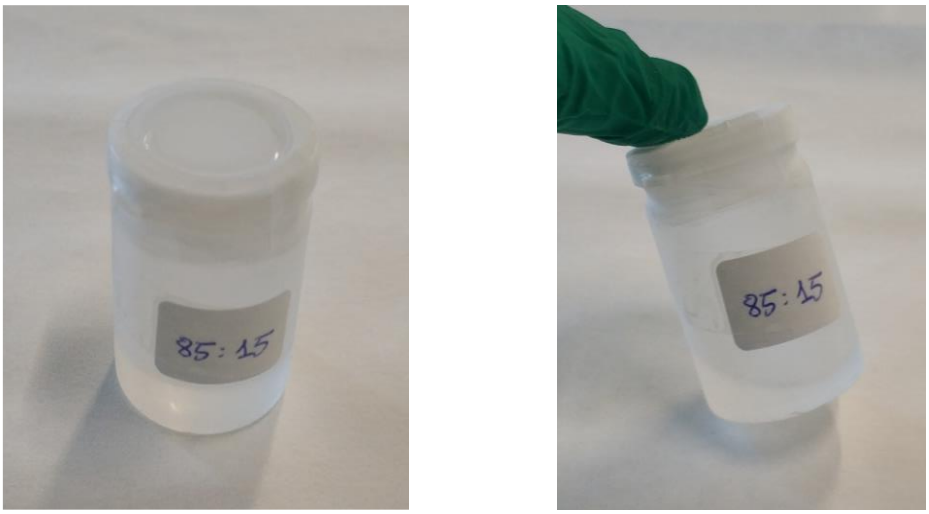

Figure S7. 85:15 ENB:DCPD mixture at -70°C after 14 days. The blend presents fluidity and no phase separation.

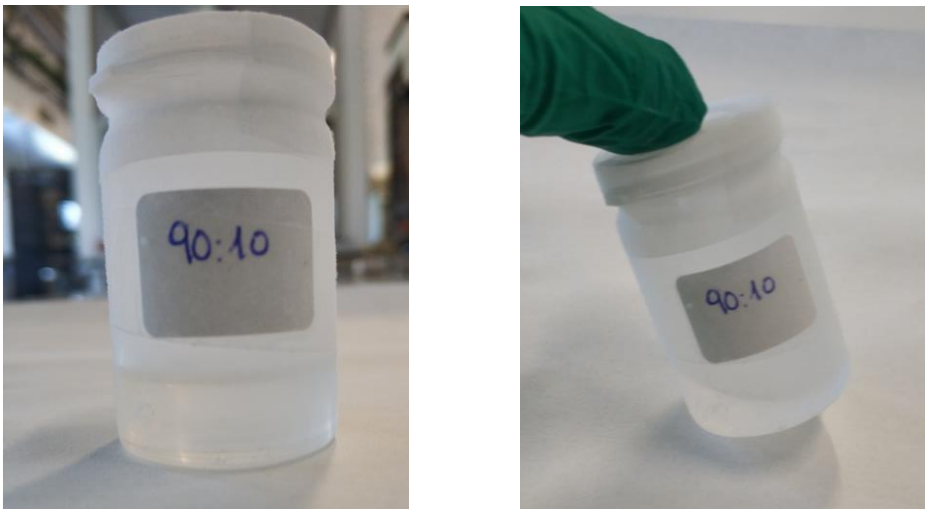

Figure S8 90:10 ENB:DCPD mixture at -70°C after 14 days. The blend presents fluidity and no phase separation.

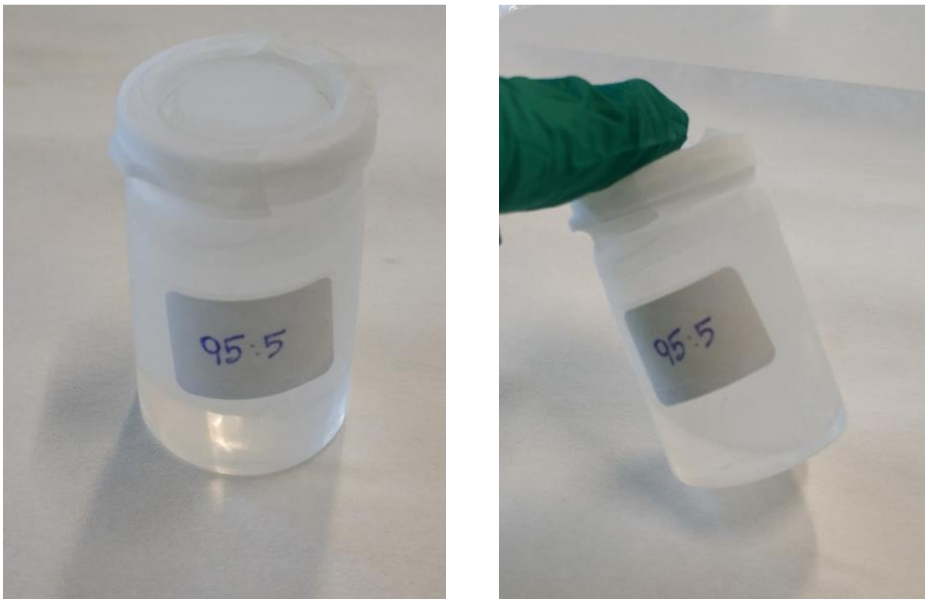

Figure S9. 95:5 ENB:DCPD mixture at -70°C after 14 days. The blend presents fluidity and no phase separation.

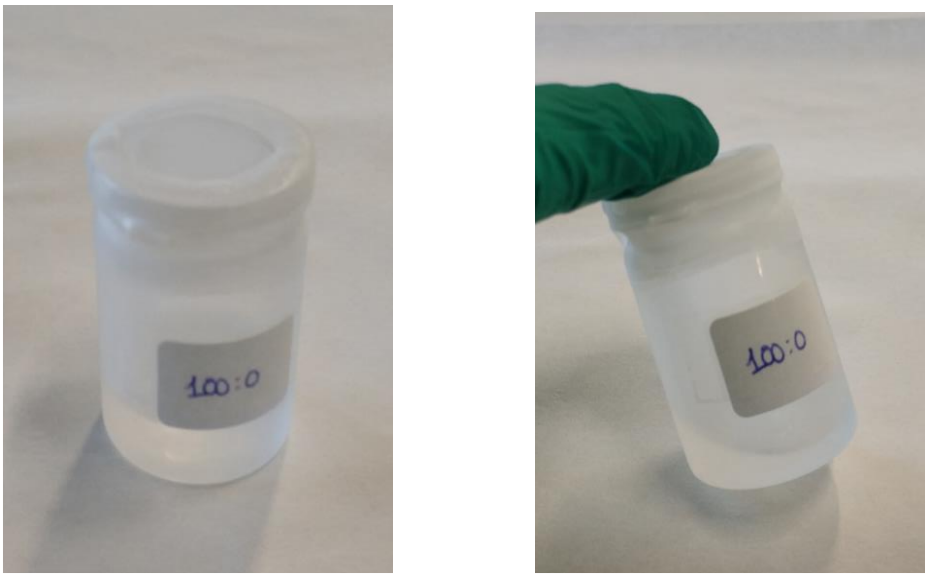

Figure S10. 100:00 ENB:DCPD mixture at -70°C after 14 days. The blend presents fluidity and no phase separation.

A.3 Chemical Structure

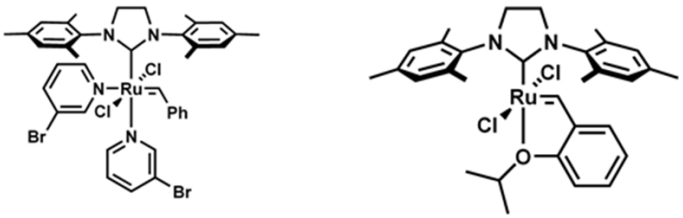

3^{rd} Generation Grubbs Catalyst

2^{nd} Generation Hoveyda-Grubbs Catalyst

Figure S11. Chemical structure of the Ru-based Catalysts used in this work.

A.4 Blend reactivity quantification at different catalyst concentration by DSC

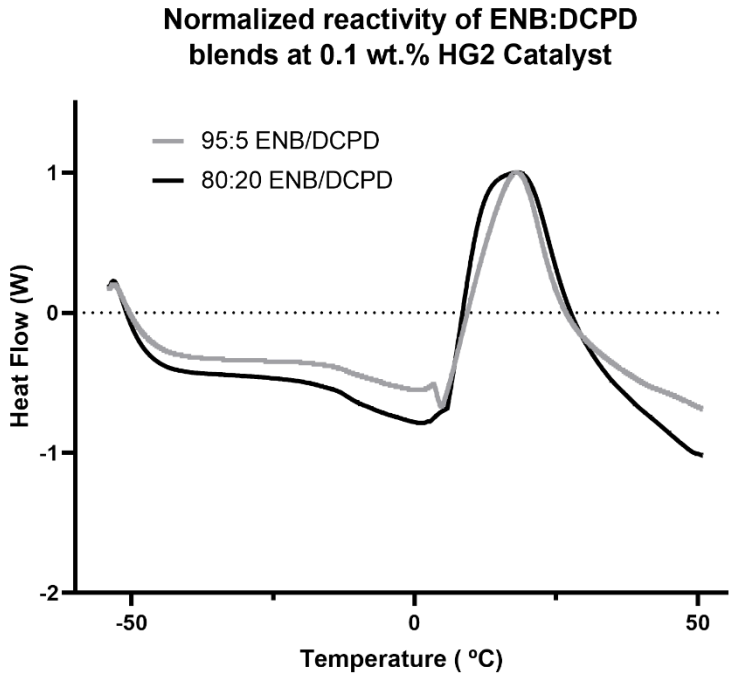

Figure S12. Normalized DSC reaction curves of different ENB/DCPD blends at 0.1 wt.% HG2 concentration. Due to the sample's reactivity, it was difficult to achieve a correct measurement of the tested weight. The graphs were normalized in order to remove the mass as a variable and observe the peak and the onset temperature and compare it with the G3 counterpart.

Table 1. Summary of all the results (Onset and Peak temperature) obtained by the DSC temperature ramp of the different ENB/DCPD blends at 0.01 and 0.004 wt.% concentration

	ENB/DCPD (wt.%)	T_{onset} (°C)	T_p(°C)
Grubb's 3rd Catalyst at 0.01 wt.%	100:0	-25.44	0.71
	95:5	-22.54	2.69
	90:10	-21.21	2.71
	85:15	-18.76	3.74
	80:20	-18.32	4.45

	ENB/DCPD (wt.%)	T_{onset} (°C)	T_p(°C)
Grubb's 3rd Catalyst at 0.004 wt.%	100:0	-18.98	3.76
	95:5	-18.76	3.76
	90:10	-16.83	6.02
	85:15	-15.32	6.79
	80:20	-17.30	4.81

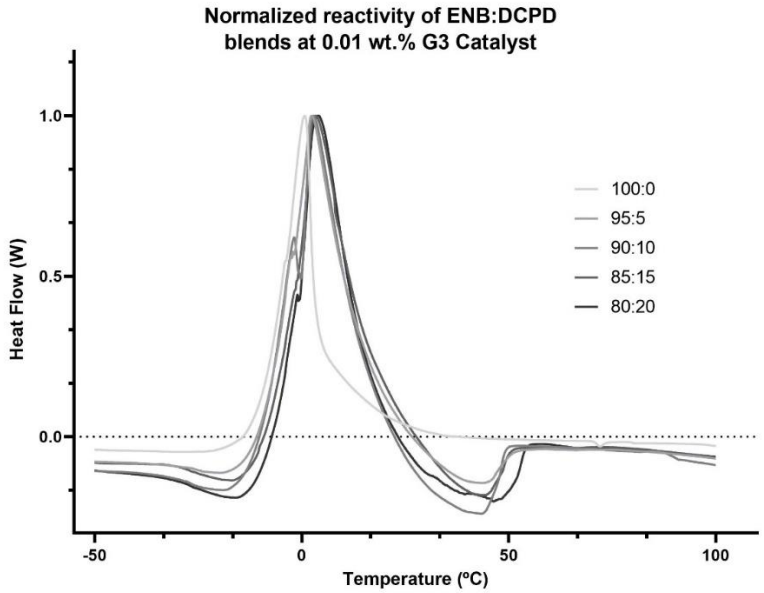

Figure S13.Normalized DSC reaction curves of different ENB/DCPD blends at 0.01 wt.% G3 concentration. Due to the sample's high reactivity, it was impossible to achieve a correct measurement of the tested weight. The graphs were normalized in order to remove the mass as a variable and observe the peak and the onset temperature.

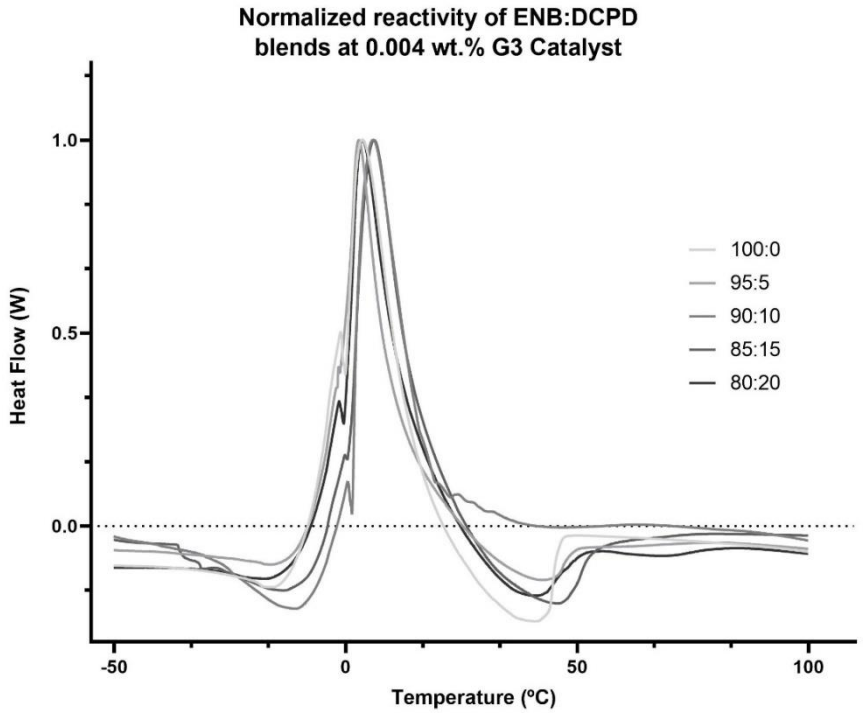

Figure S14. Normalized DSC reaction curves of different ENB/DCPD blends at 0.001 wt.% G3 concentration. Due to the sample's high reactivity, it was impossible to achieve a correct measurement of the tested weight. The graphs were normalized in order to remove the mass as a variable and observe the peak and the onset temperature.

Although all results follow the expected trend, there is however, an anomaly on the 80:20 blend with 0.001 wt.%, which exhibited a slightly lower T_{onset} and T_p that blends with higher ENB content at the same catalyst ratio. Nonetheless, all the selected ratios at the chosen G3 catalyst concentration confirmed a good cryogenic reactivity and therefore, have potential to be used as a self-healing reactivity blend for the intended application.

A.5 Scanning electron microscope images of Microcapsules

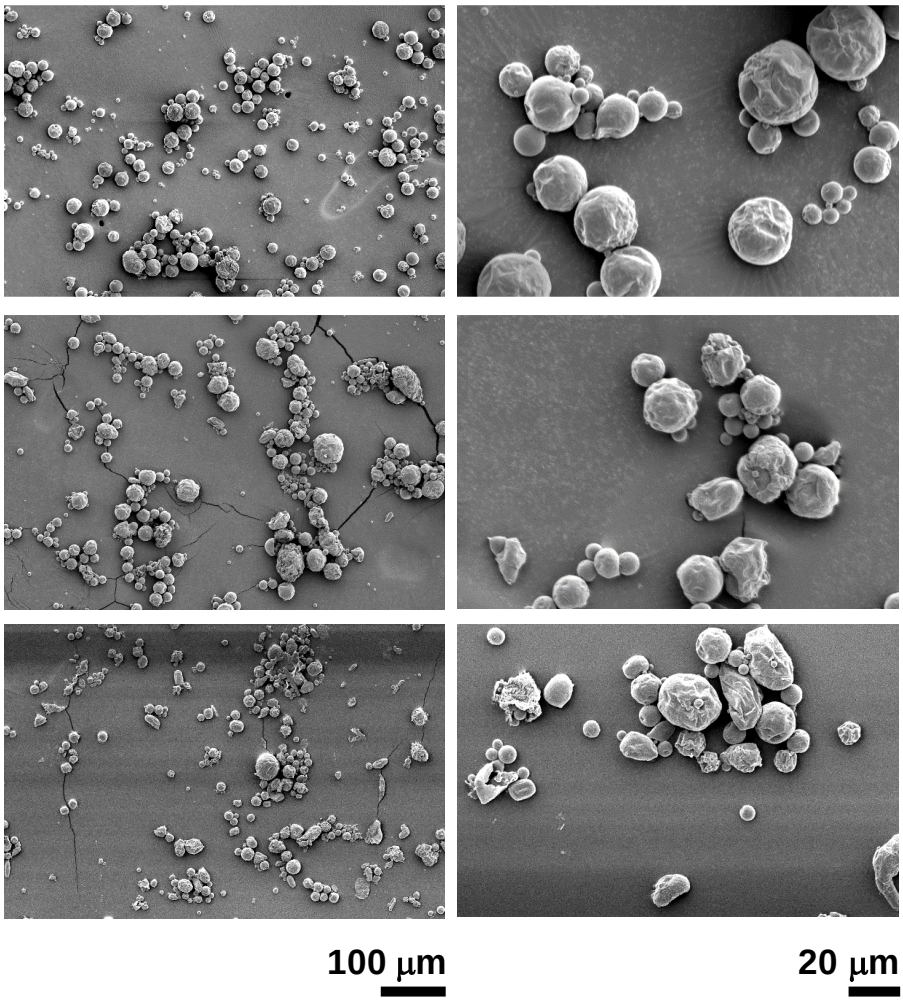

Figure S15. SEM micrographs of ENB/DCPD polyurea microcapsules synthesized employing TOP 50 °C/1h (M14), MIDDLE 70 °C/3h (M15), and BOTTOM 70 °C/overnight (M17).

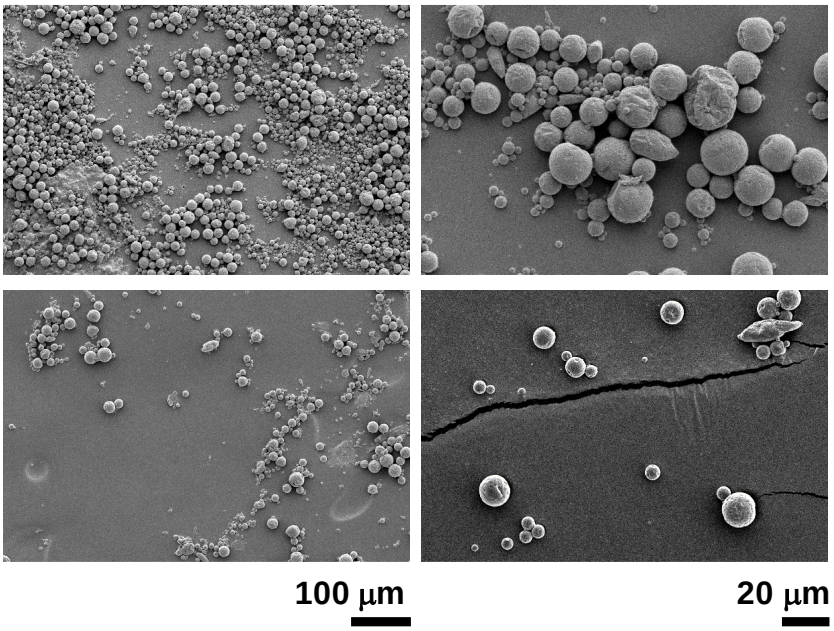

Figure S16. SEM micrographs of ENB/DCPD polyurea microcapsules synthesized at 5000 rpm in the emulsion step: TOP 3% GA and 10 min emulsion (Entry MC18), and BOTTOM 3.5% GA and 20 min emulsion (M19).

A.6 FT-IR assessment of the microparticles

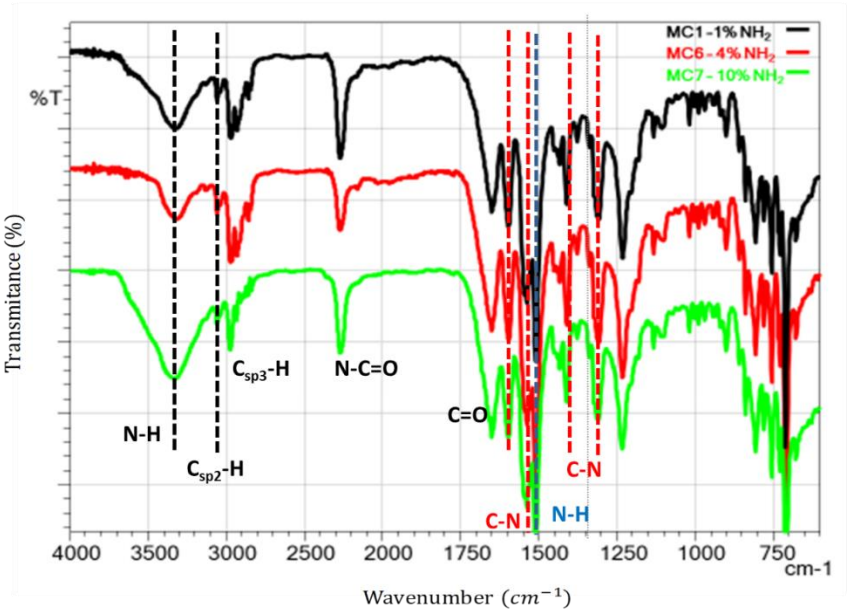

Figure 17. FT-IR spectra of the microcapsules obtained at 1% (black), 4% (red) and 10% (green)amine concentrations in aqueous solution.

A.7 FIB-FESEM images of the microcapsules

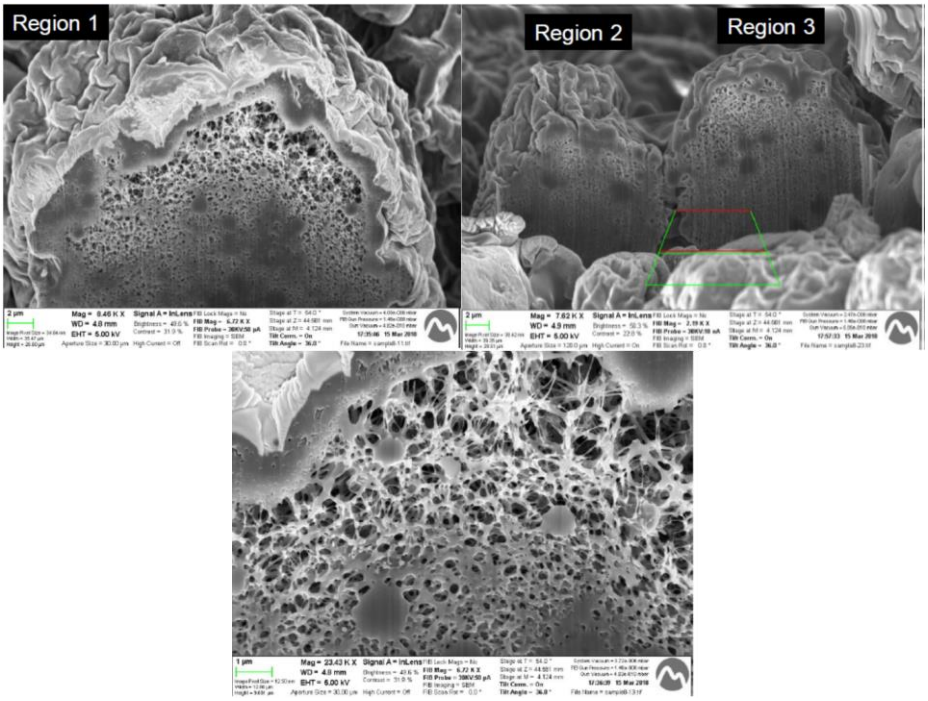

Figure S18. FESEM images of FIB cross-sections of MC1.

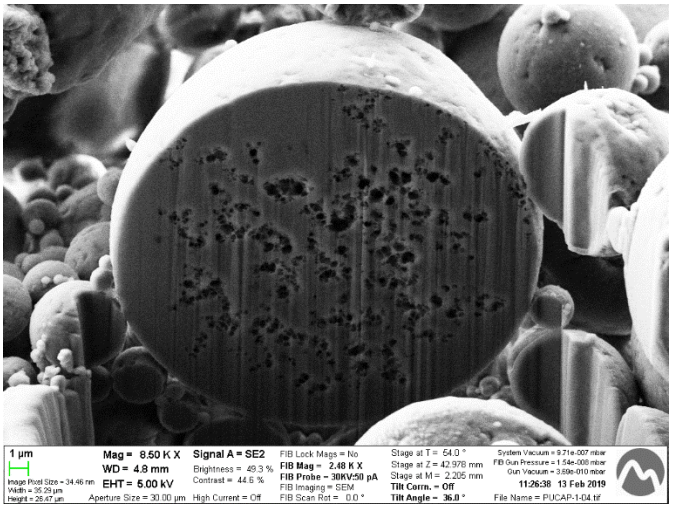

Figure S19. FESEM images of FIB cross-sections of MC5.

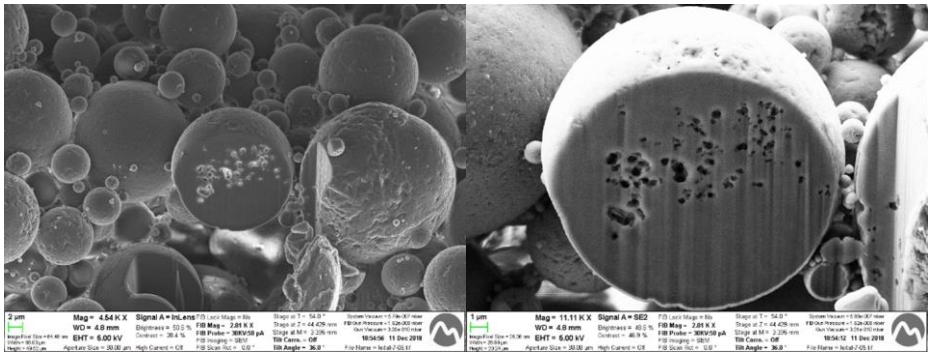

Figure S20. FESEM images of FIB cross-sections of MC18.

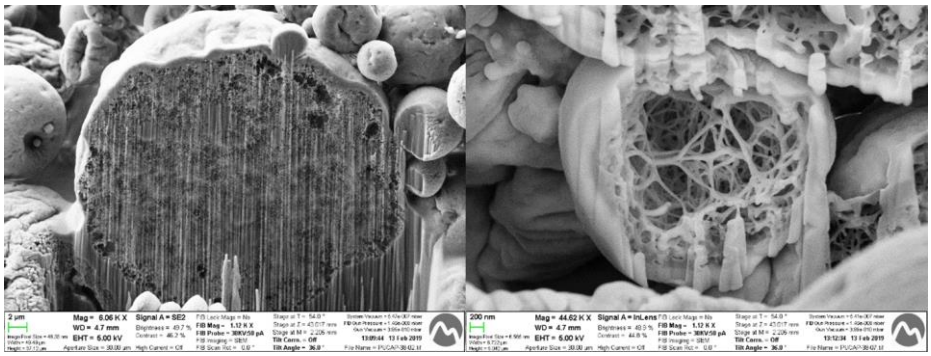

Figure S21. FESEM images of FIB cross-sections of MC19.

A.8 Thermogravimetry analysis of microcapsules (TGA)

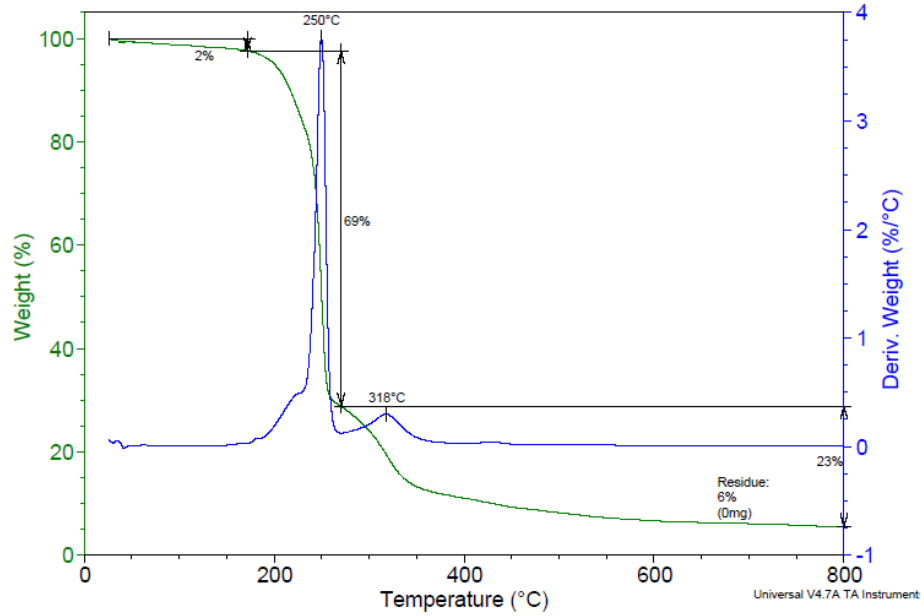

Figure S22. TGA of MC1.

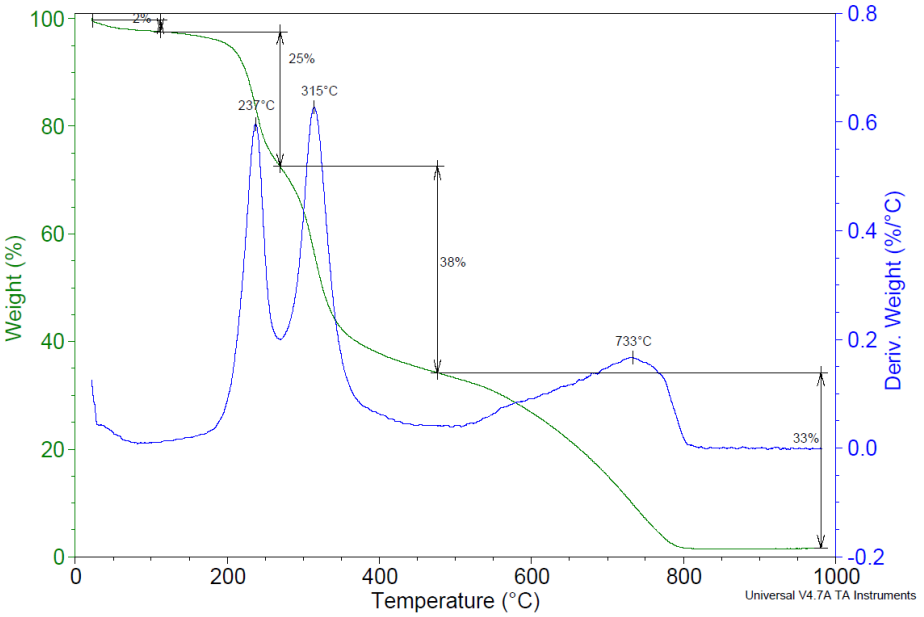

Figure S23. TGA of MC4.

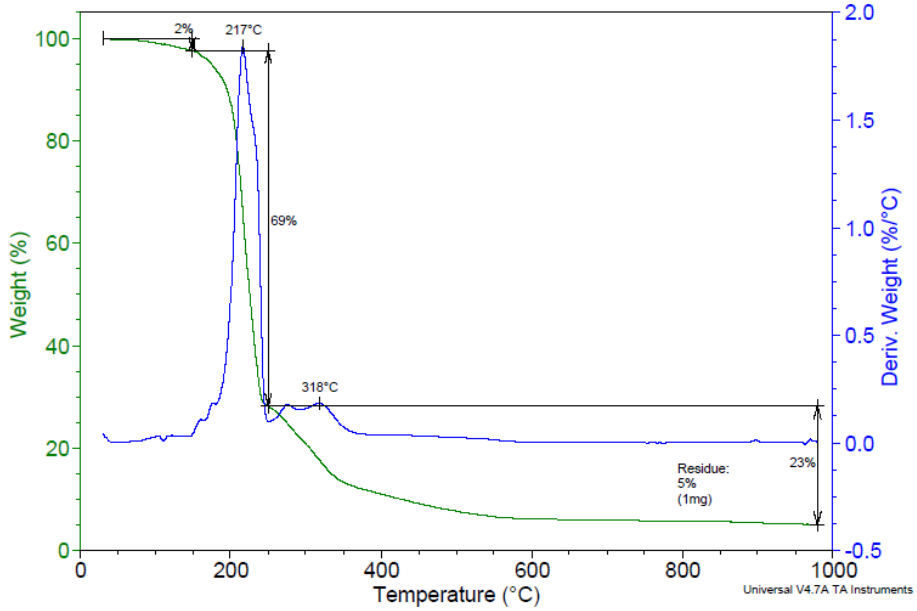

Figure S24. TGA of MC5.

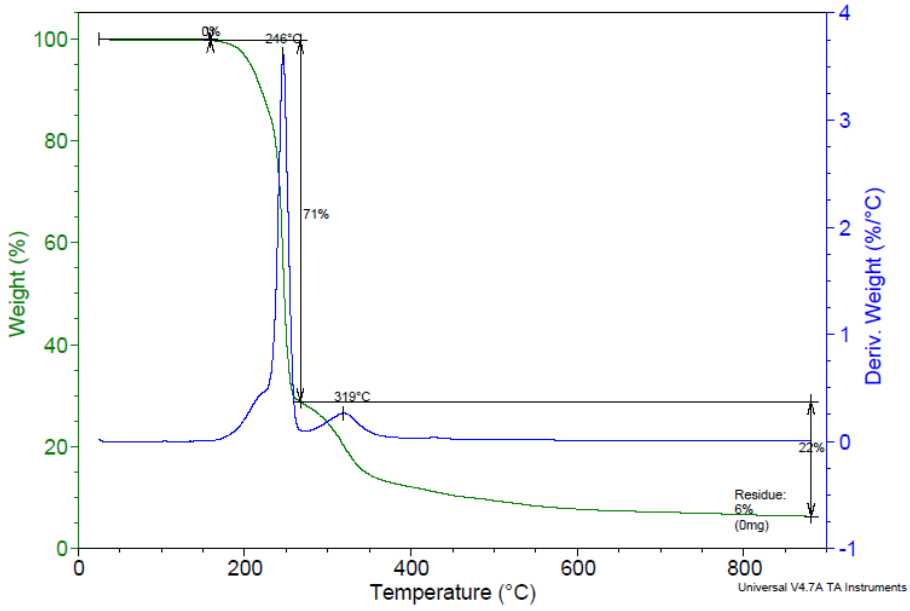

Figure S25. TGA of MC6.

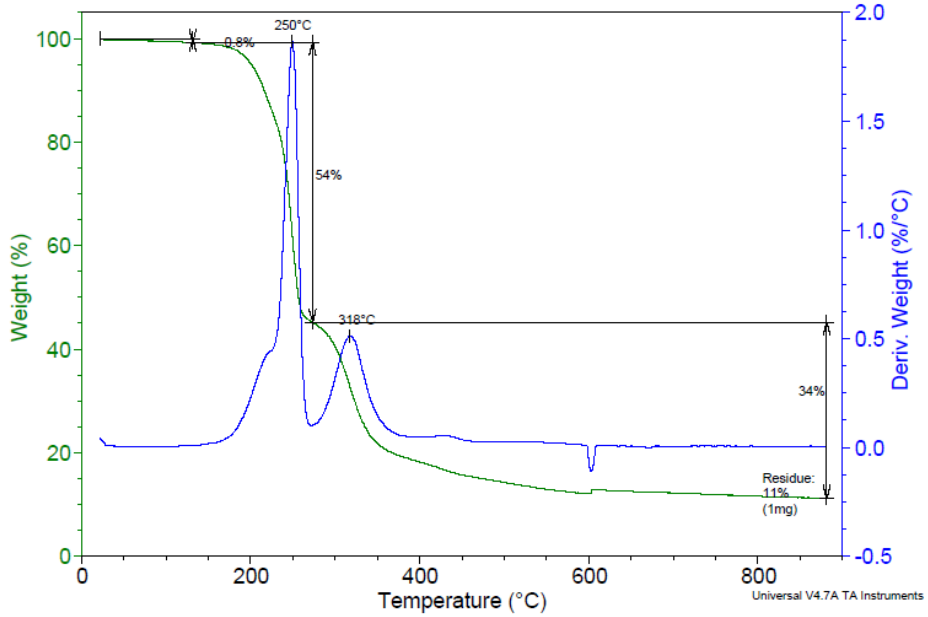

Figure S26. TGA of MC8.

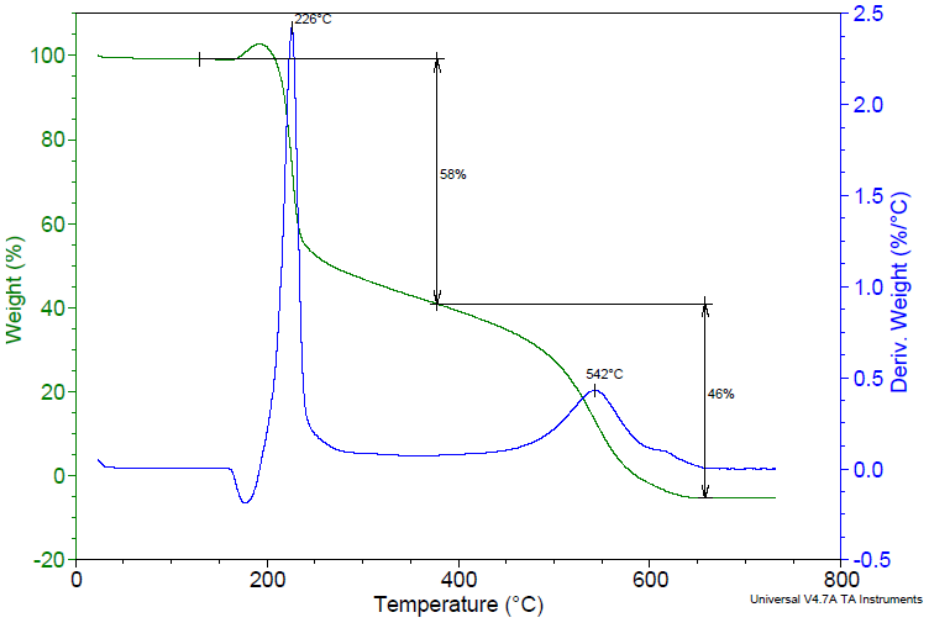

Figure S27. TGA of MC9.

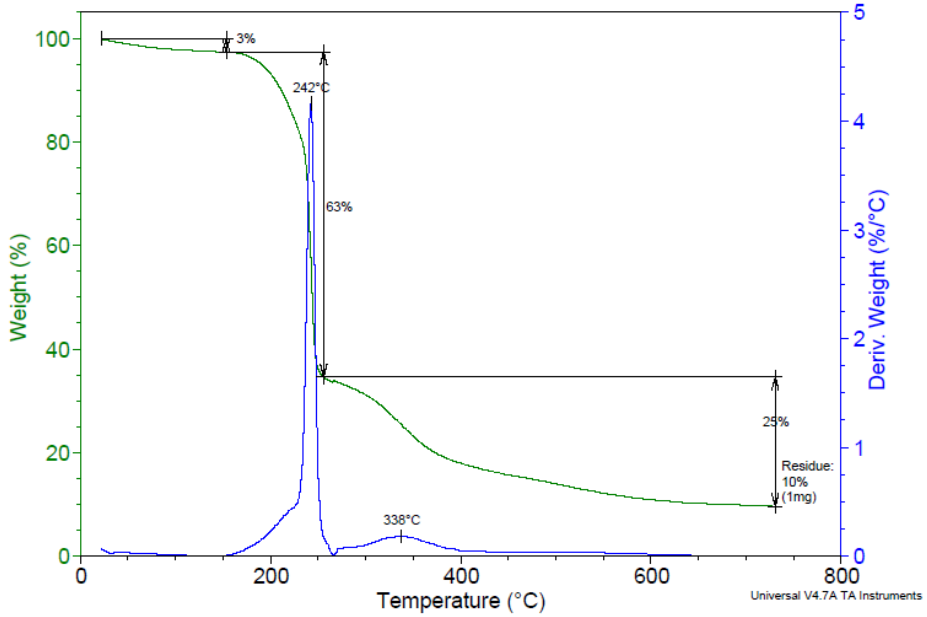

Figure S28. TGA of MC14.

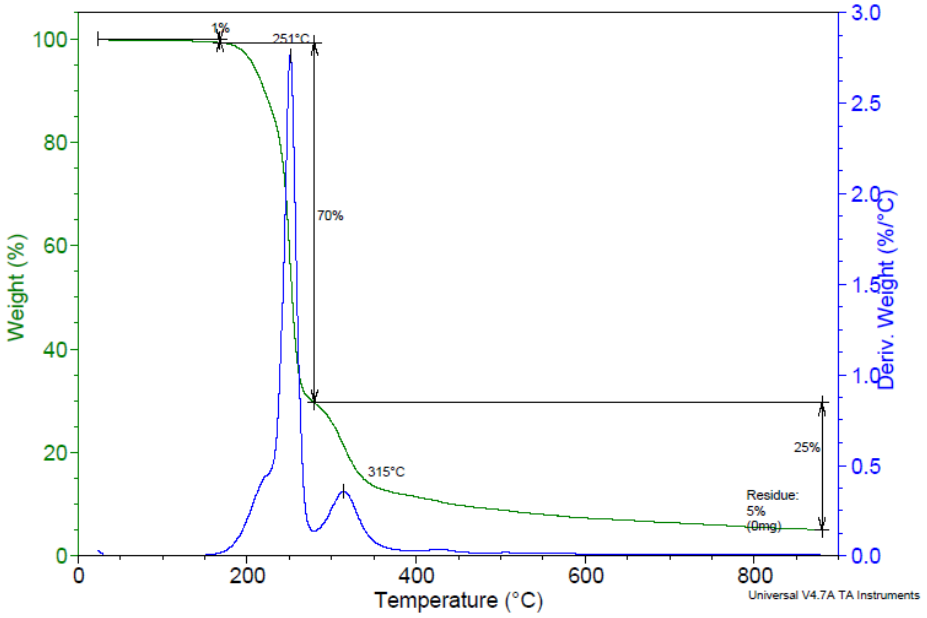

Figure S29. TGA of MC15.

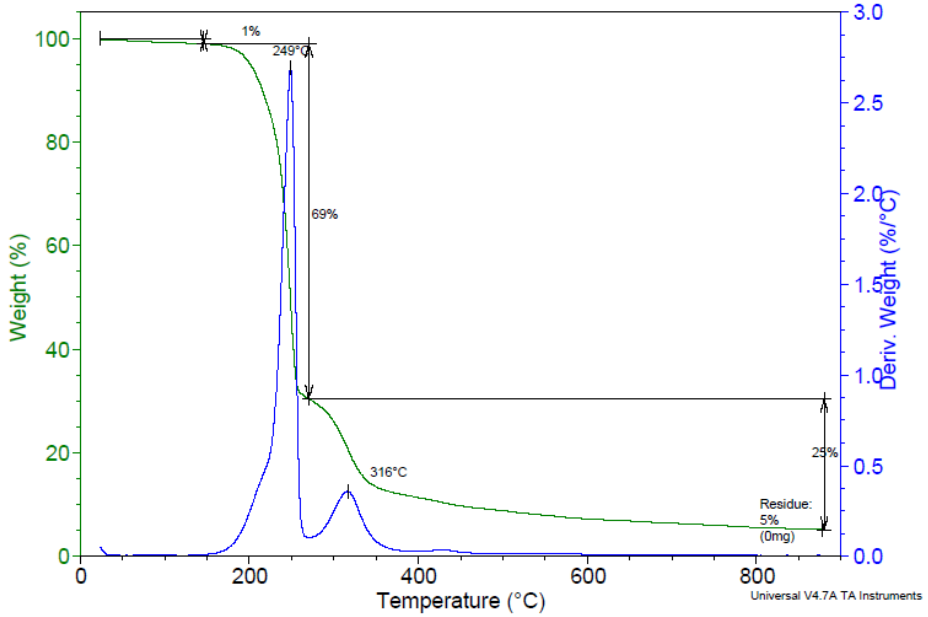

Figure S30. TGA of MC16.

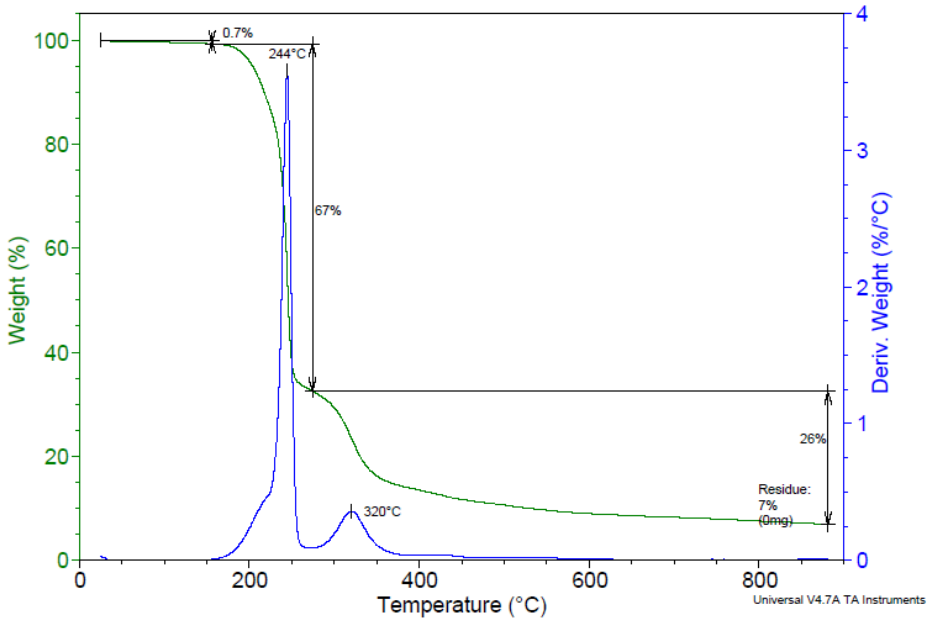

Figure S31. TGA of MC17.

v

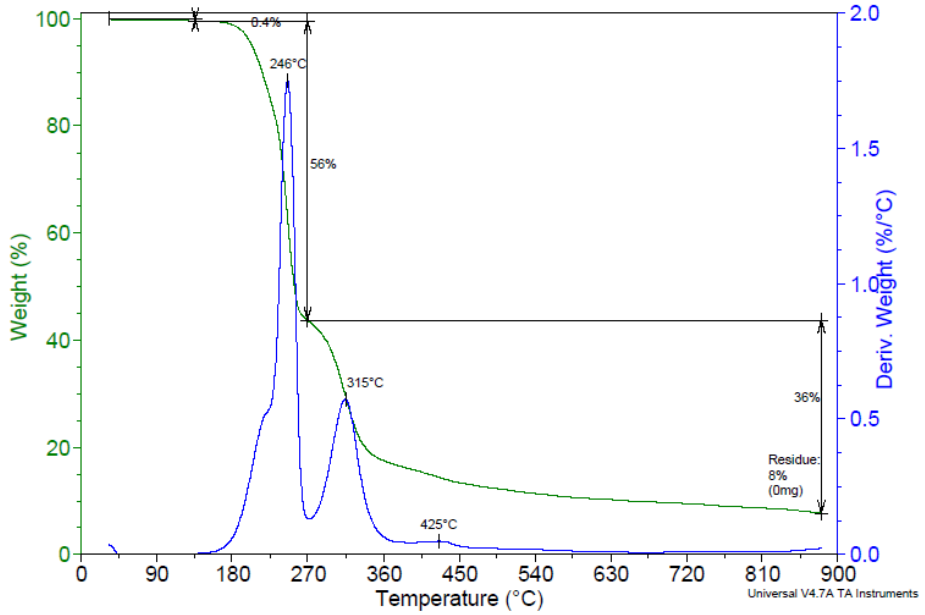

Figure S32. TGA of MC18.

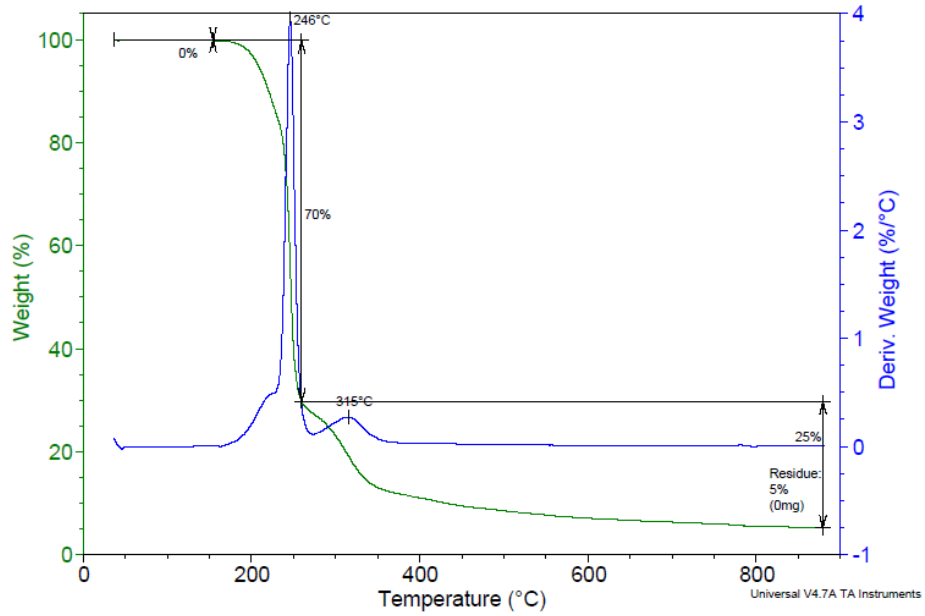

Figure S33. TGA of MC19.

A.9 FTIR spectra of microcapsules

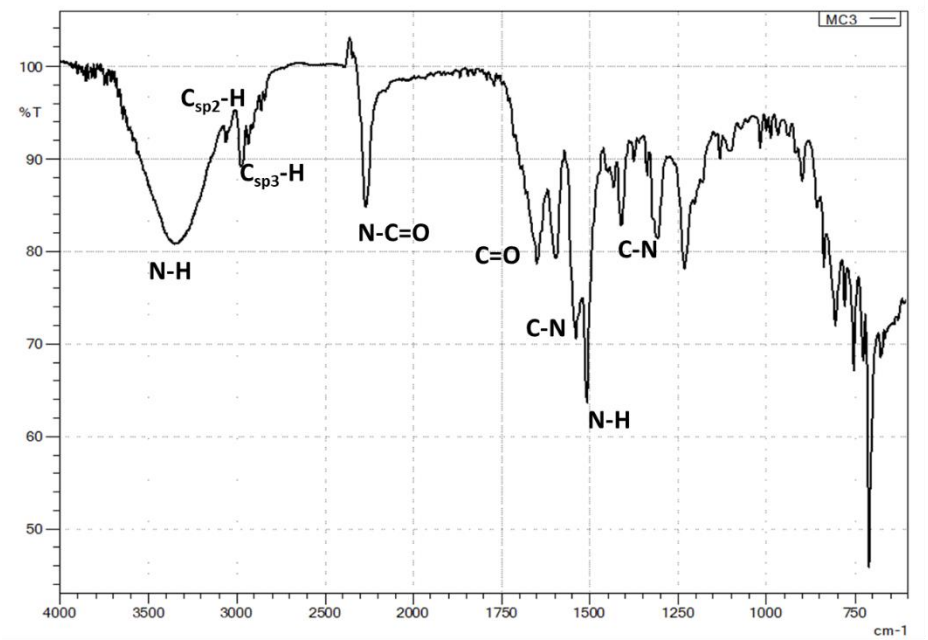

Figure S34. FTIR spectrum of MC3.

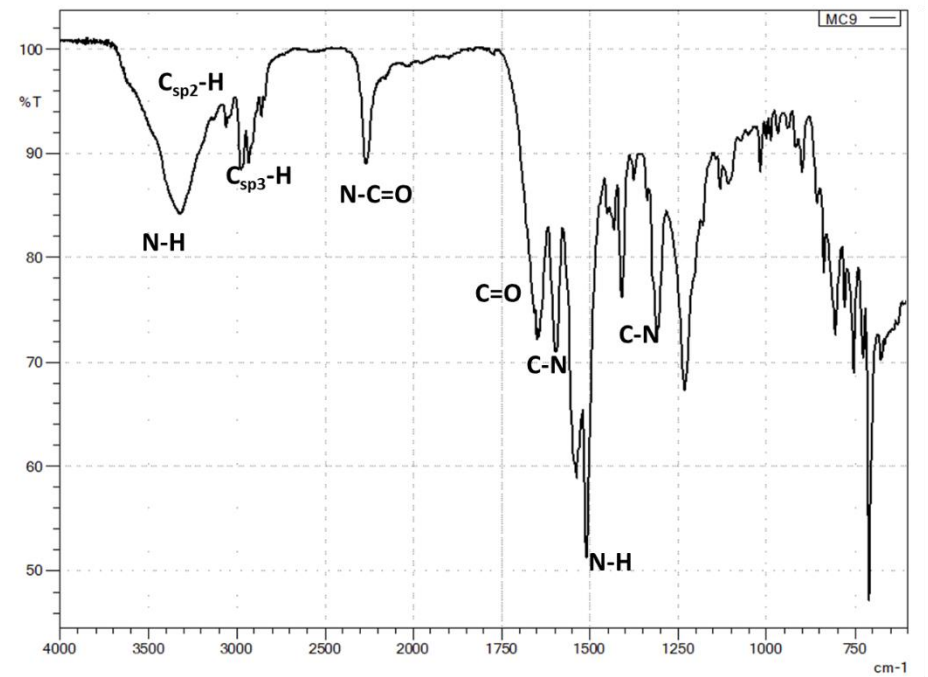

Figure S35. FTIR spectrum of MC9.

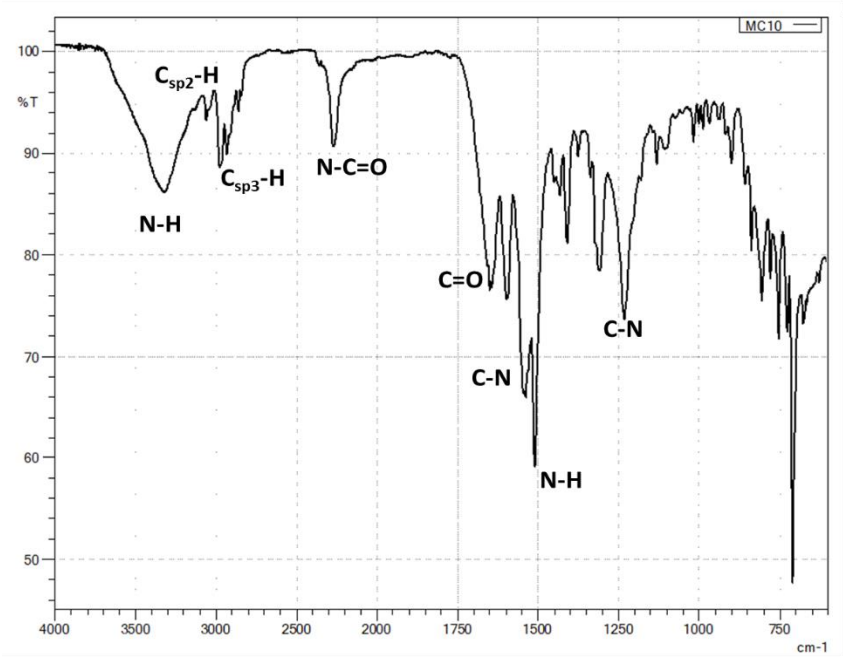

Figure S36. FTIR spectrum of MC10.

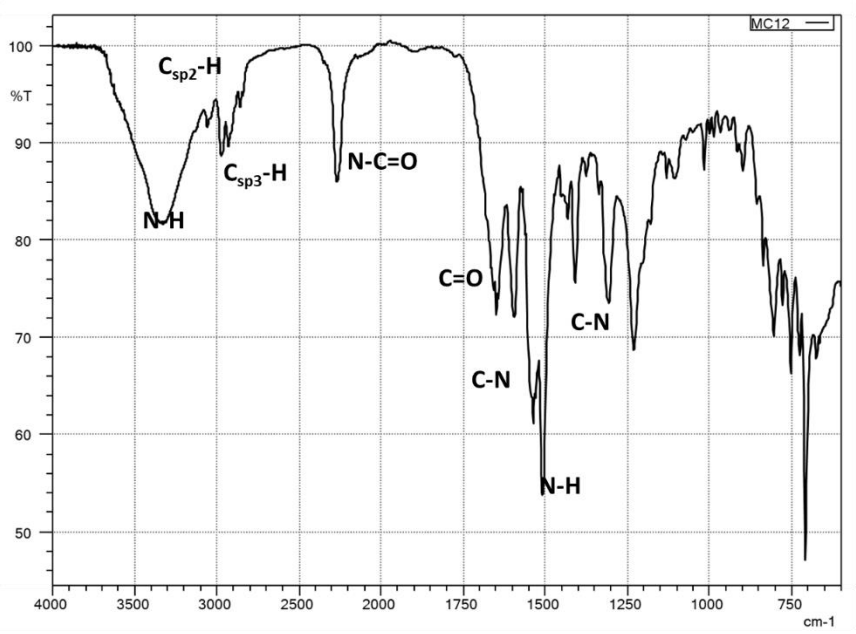

Figure S37. FTIR spectrum of MC12.

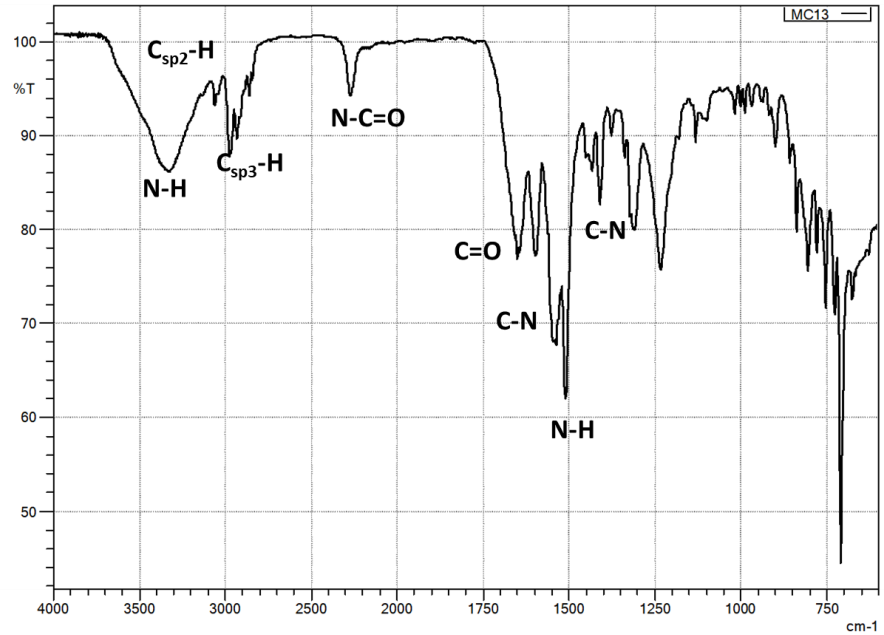

Figure S38. FTIR spectrum of MC13.

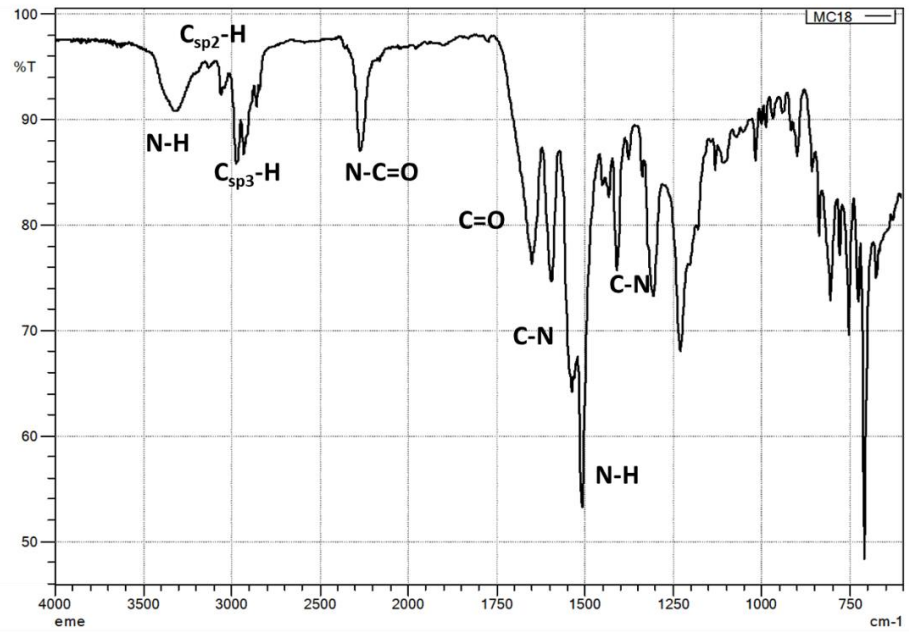

Figure S39. FTIR spectrum of MC18.

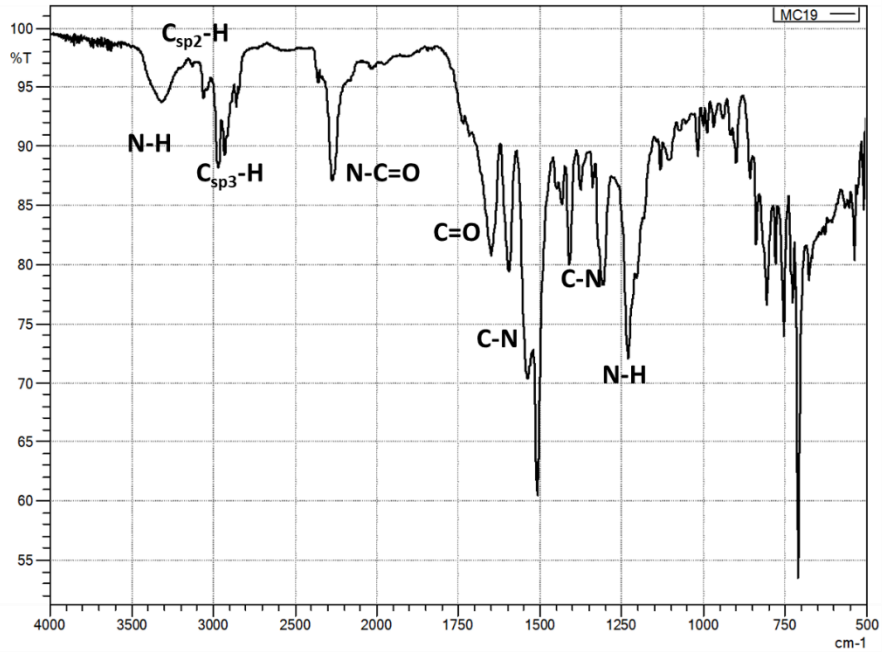

Figure S40. FTIR spectrum of MC19.

A.10 NMR spectra of microcapsules

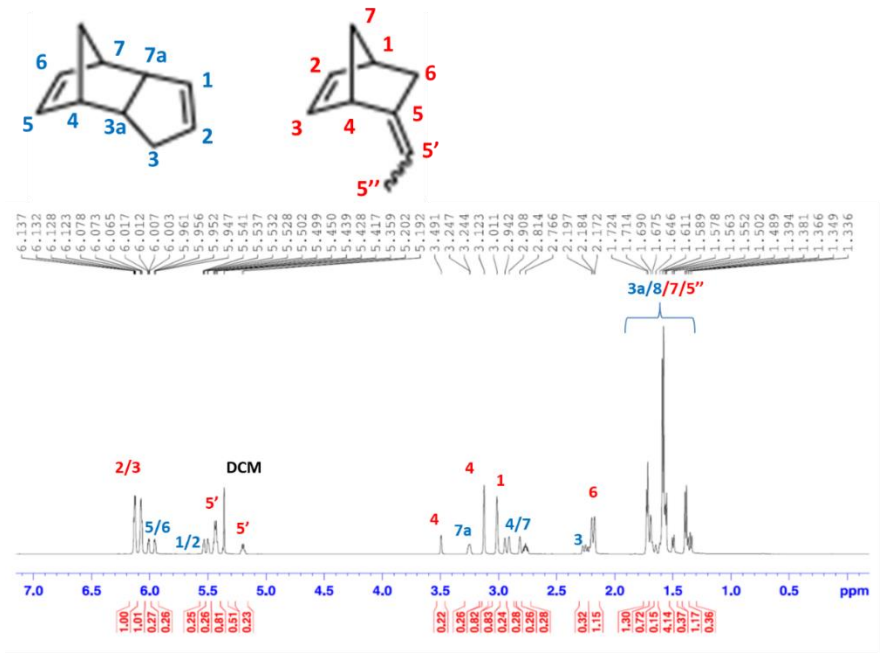

Figure S41. 1H-NMR (DCM-d_2, 600MHz) spectrum of MC19.

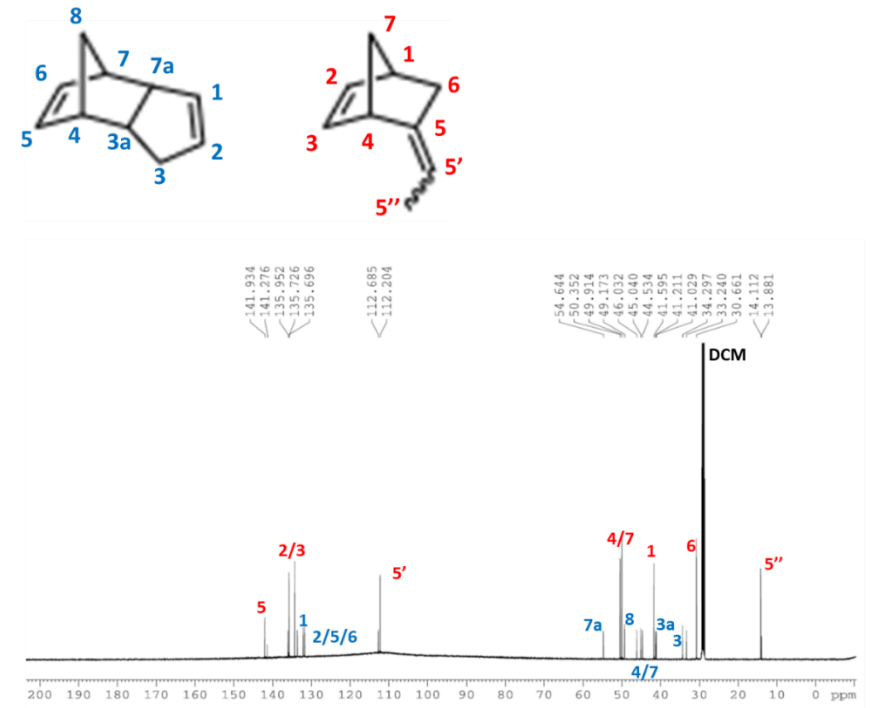

Figure S42. 13C-NMR (DCM-d_2, 150MHz) spectrum of MC19.

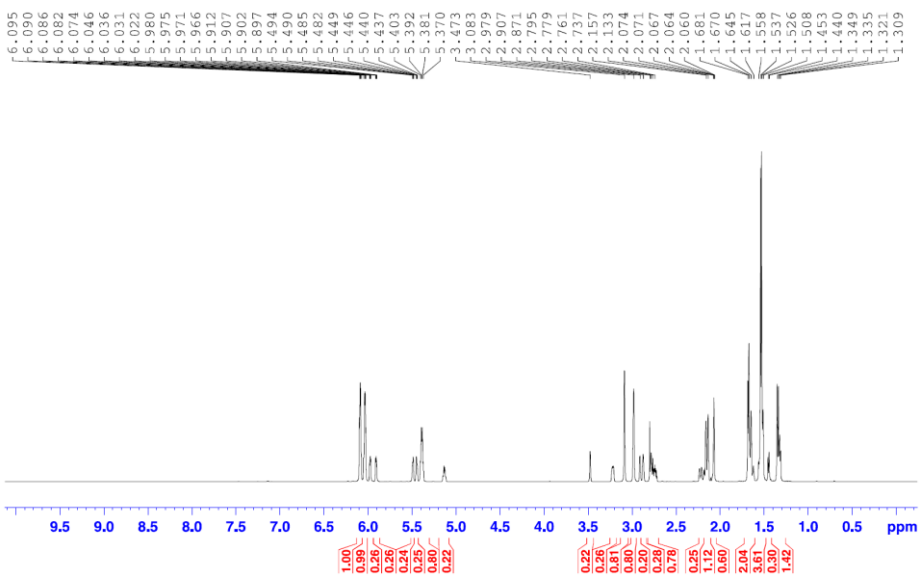

Figure S43. 1H-NMR (acetone-d_6, 600MHz) spectrum of MC19 actone-d_6 extracts.

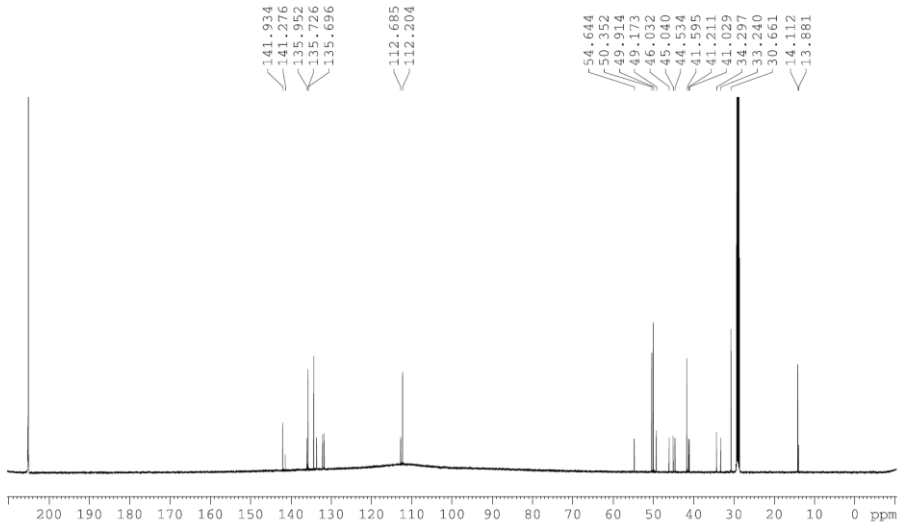

Figure S44. 13C-NMR (acetone-d6, 150MHz) spectrum of MC19 actone-d6 extracts.

A.11 Viscosity Results:

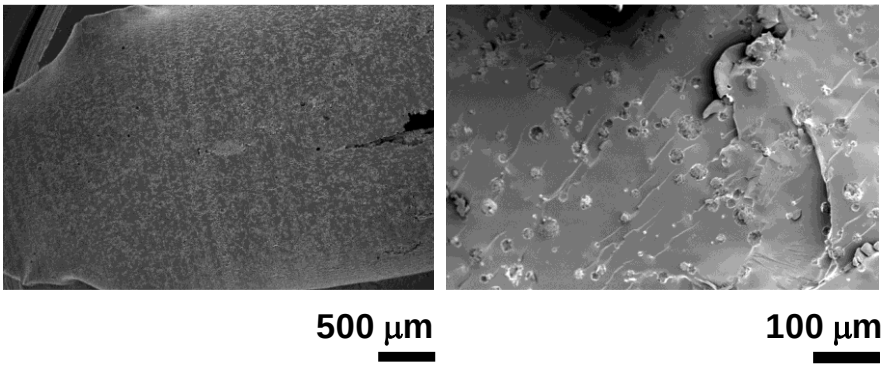

Figure S45. SEM micrographs of ENB/DCPD polyurea microcapsules with 20 wt.% (left) and 10wt.% (right) dispersed in epoxy resin.

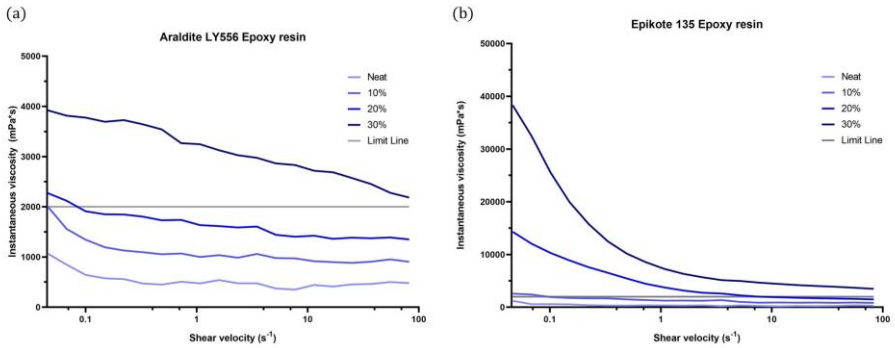

Figure S46. Viscosity curve at 25°C of (a) Araldite LY556 epoxy resin component. (b) Epikote 135 epoxy resin component.